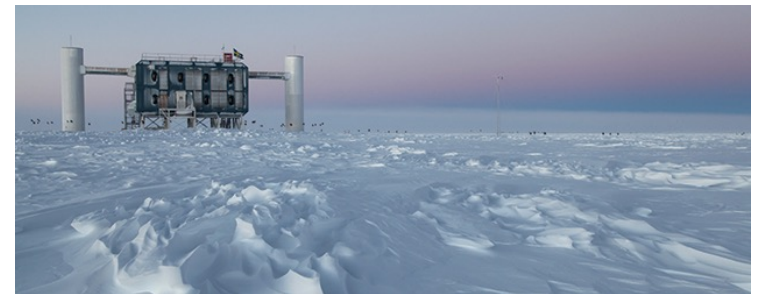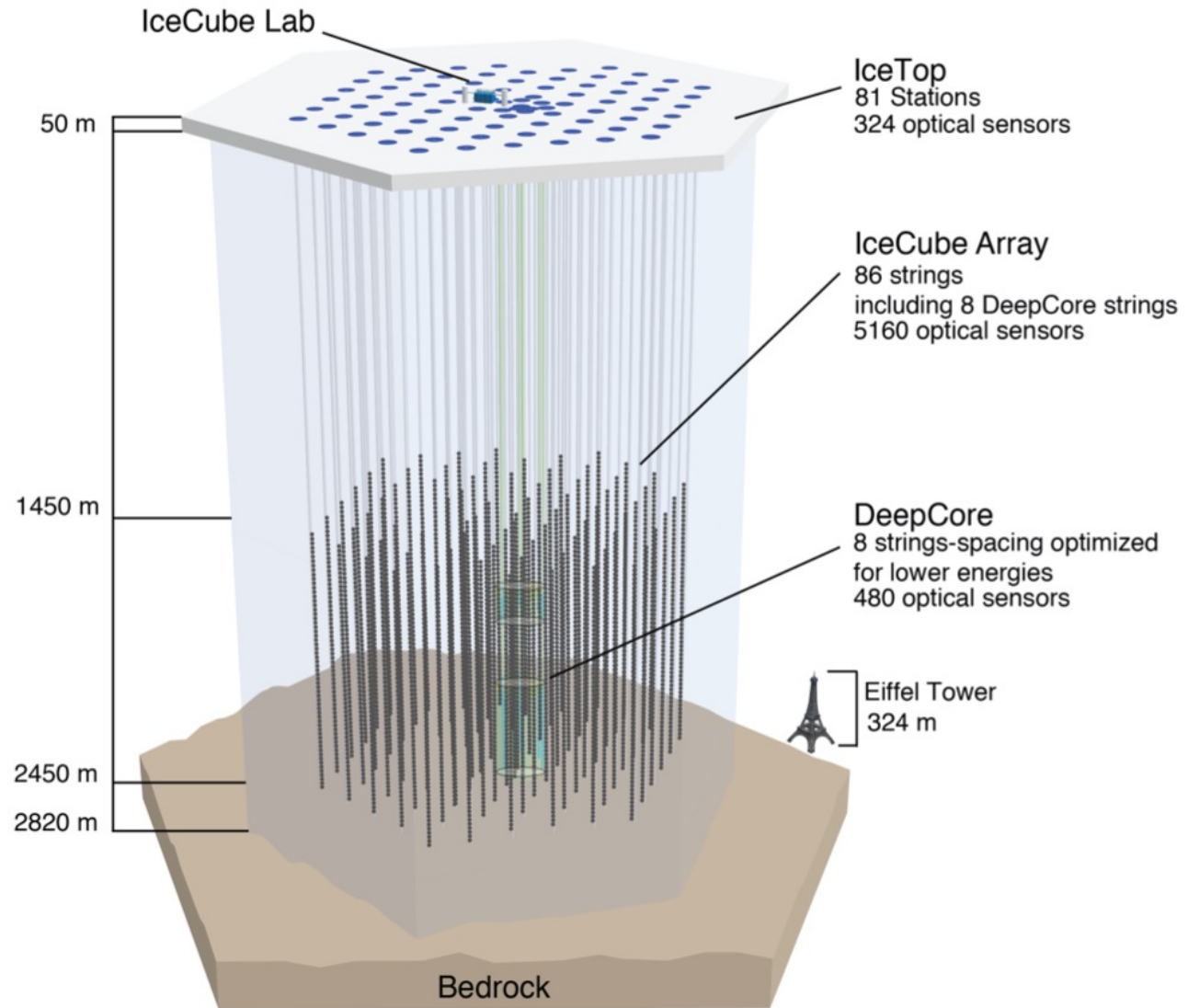# IceCube calibration: ice properties

Dmitry Chirkin, UW Madison
IceCube summer school 2024
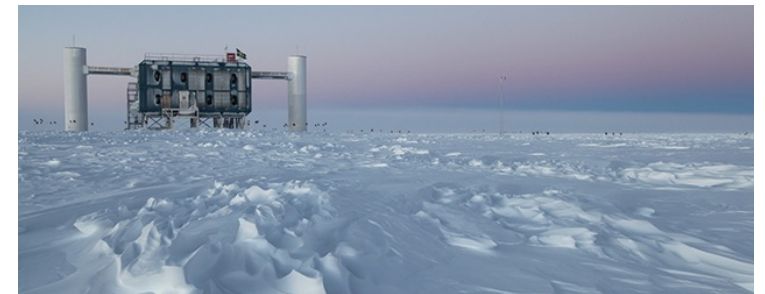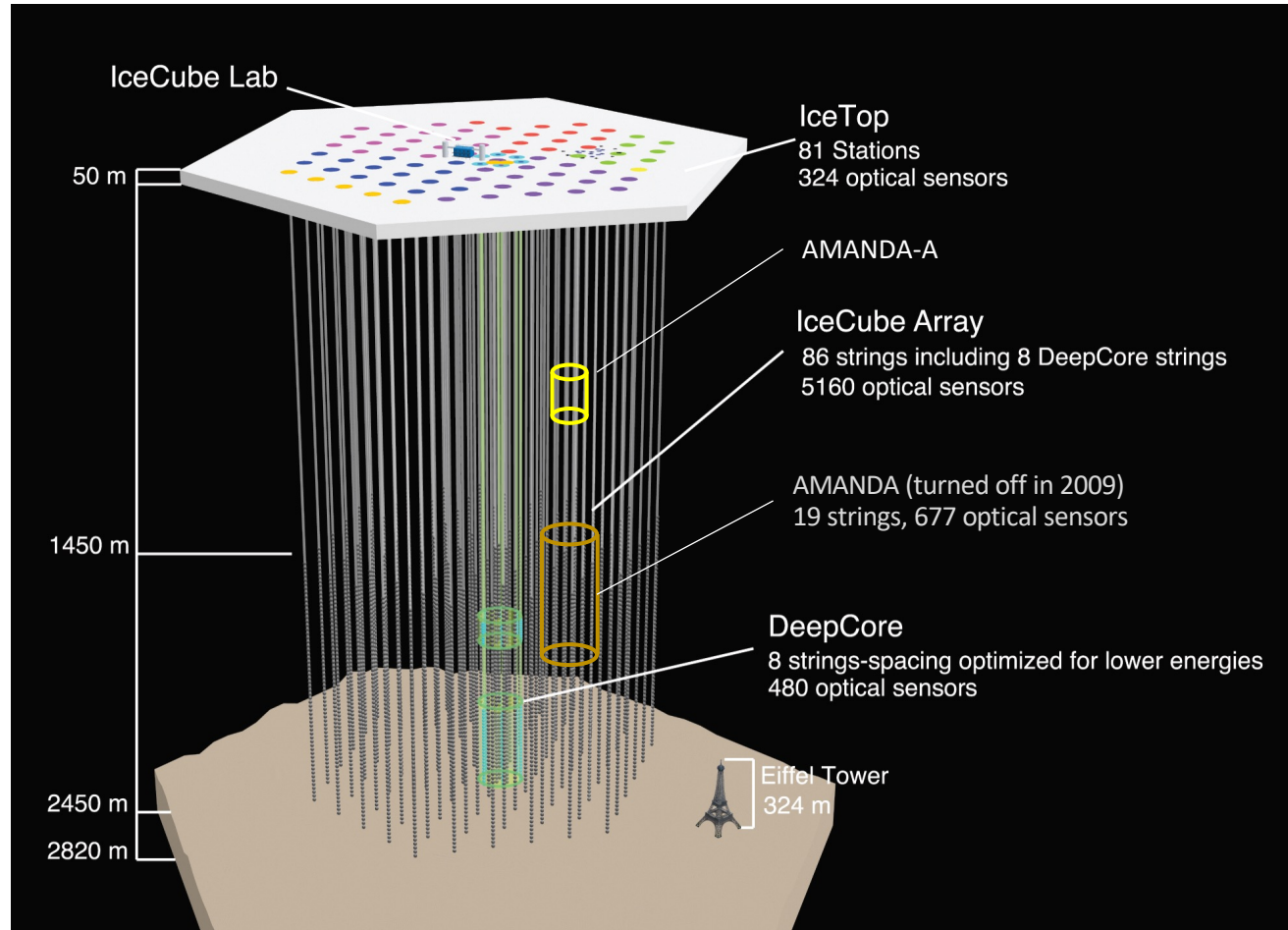
Dmitry Chirkin, UW Madison
IceCube summer school 2024

Ice model evolution
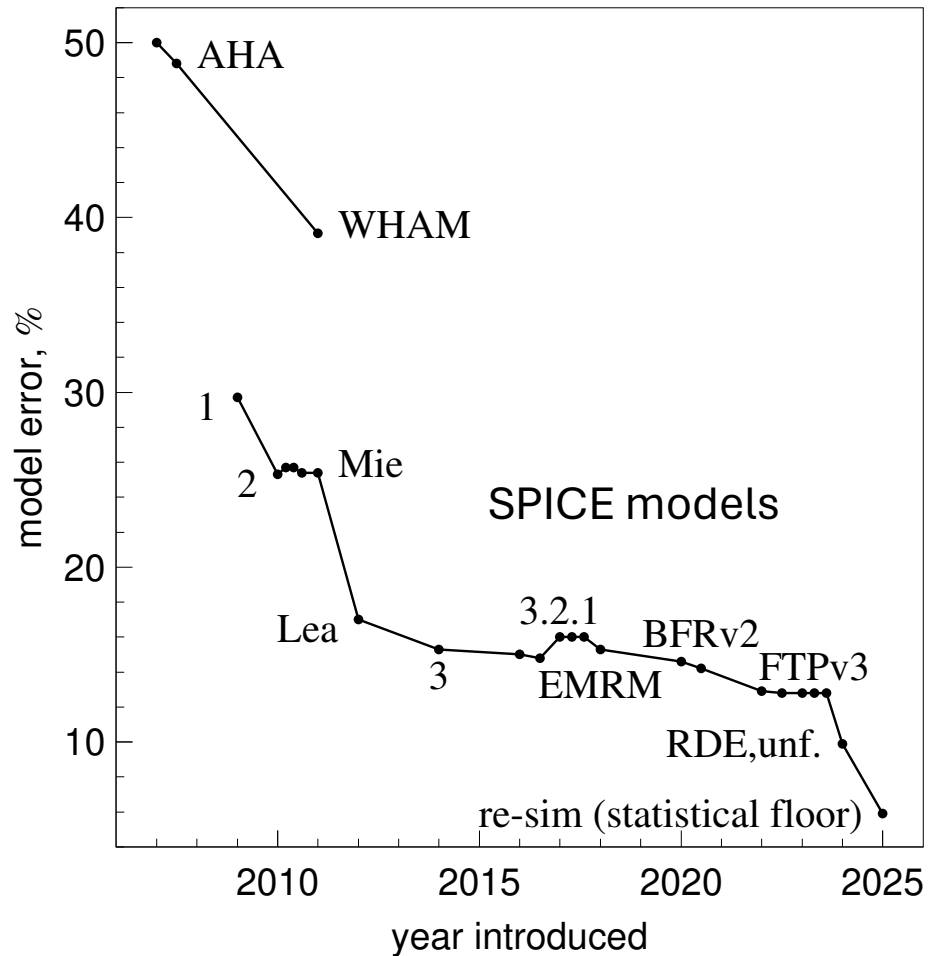
AMANDA-A (1994): dominated by air bubbles

AMANDA II (2006): clear ice at depths 1.4-2.3 km

IceCube (2013): layer tilt, ice anisotropy

IceCube (2023): birefringence, precise 2d tilt

Ice model evolution
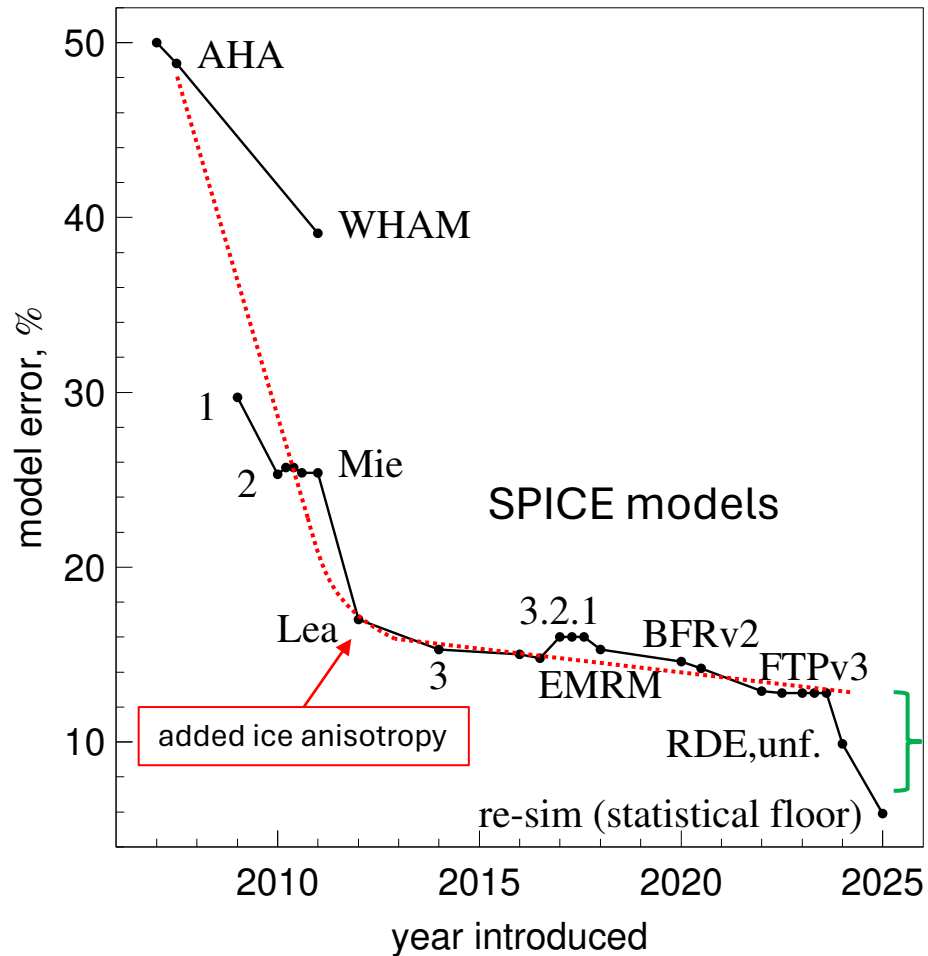

AMANDA-A (1994): dominated by air bubbles

AMANDA II (2006): clear ice at depths 1.4-2.3 km

IceCube (2013): layer tilt, ice anisotropy

IceCube (2023): birefringence, precise 2d tilt
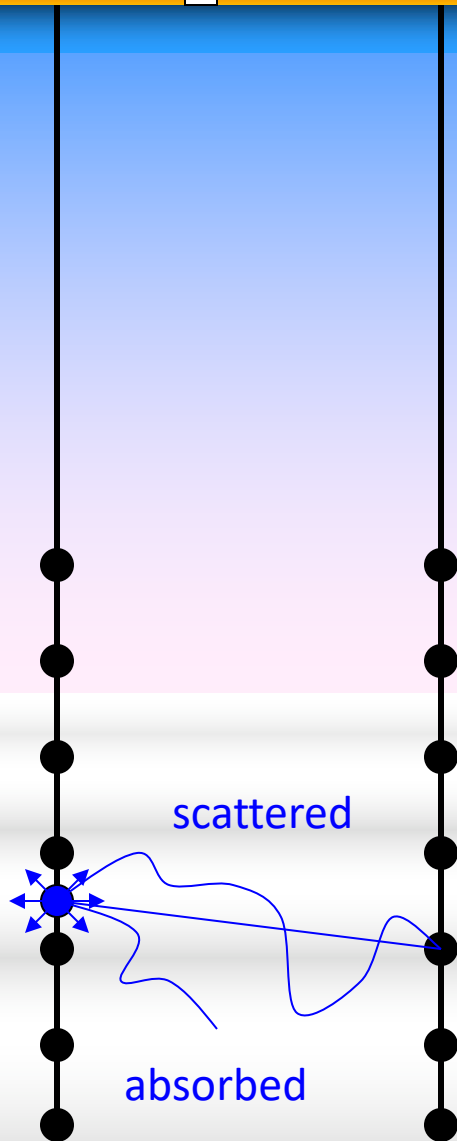
Measuring Scattering & Absorption

- Install **light sources** in the ice

- Use light sensors to:

  - Measure how long it takes
    for light to travel through ice

  - Measure how much light is delayed

  - Measure how much light does not
    arrive

- Use different wavelengths

- Do above at many different depths

scattered

absorbed

AMANDA-A: scattering on air bubbles!
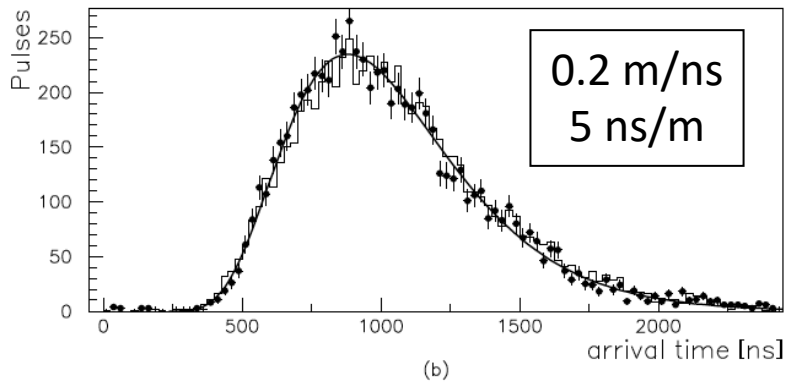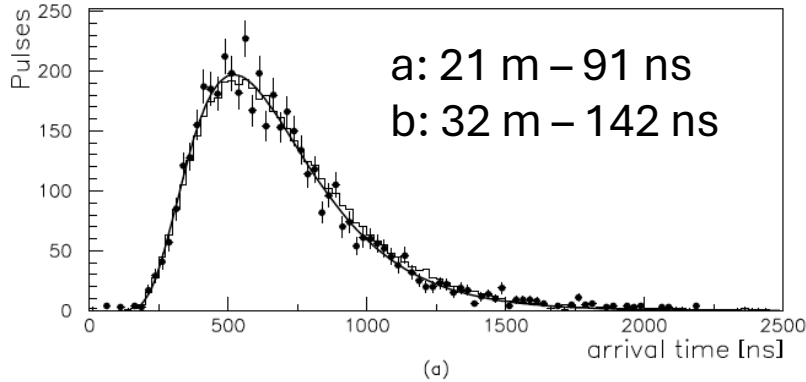
a: 21 m – 91 ns
b: 32 m – 142 ns

0.2 m/ns
5 ns/m

$$u(d,t) = \frac{1}{(4\pi Dt)^{3/2}} e^{\frac{-d^2}{4Dt}} e^{\frac{-c_i t}{\lambda_a}}$$

Analytical description (diffusive regime)
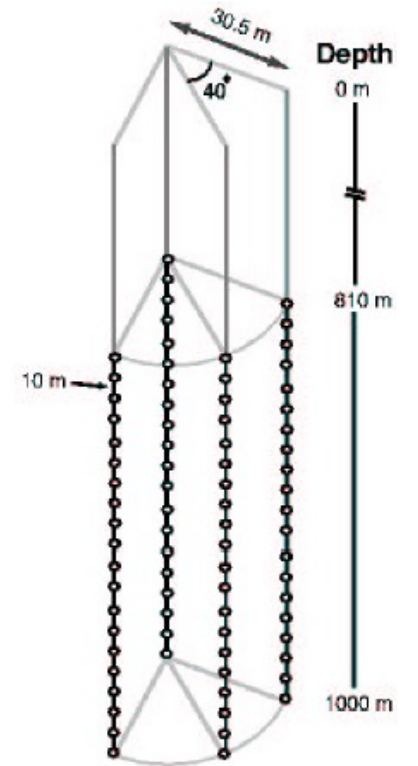Possible due to very small scattering length

1994

astro-ph/9412028   08 Dec 1994

Optical Properties of the South Pole Ice at Depths Between 0.8 and 1 km

P. Askebjer, S.W. Barwick, L. Bergström, A. Bouchta, S. Carius, A. Coulthard,
K. Engel, B. Erlandsson, A. Goobar, L. Gray, A. Hallgren, F. Halzen,
P.O. Hulth, J. Jacobsen, S. Johansson, V. Kandhadai, I. Liubarsky, D. Lowder,
T. Miller, P.C. Mock, R. Morse, R. Porrata, P.B. Price, A. Richards,
H. Rubinstein, E. Schneider, Q. Sun, S. Tilav, C. Walck & G. Yodh

The optical properties of the ice at the geographical South Pole have been investigated at depths between 0.8 and 1 kilometers. The absorption and scattering lengths of visible light (~515 nm) have been measured *in situ* using the laser calibration setup of the AMANDA neutrino detector. The ice is intrinsically extremely transparent. The measured absorption length is 59 ± 3 meters, comparable with the quality of the ultra-pure water used in the IMB and Kamiokande proton-decay and neutrino experiments and more than two times longer than the best value reported for laboratory ice. Due to a residual density of air bubbles at these depths, the trajectories of photons in the medium are randomized. Assuming bubbles are smooth and spherical, the average distance between collisions at 1 km depth is about 25 cm. The measured inverse scattering length on bubbles decreases linearly with increasing depth in the volume of ice investigated.
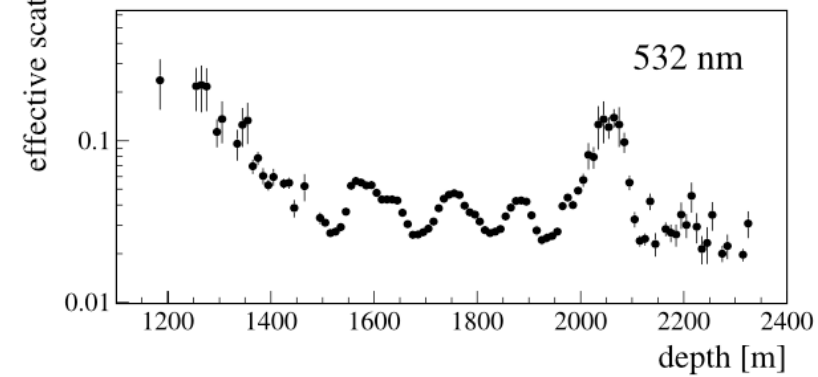
The AMANDA (Antarctic Muon And Neutrino Detector Array) project was conceived to exploit polar ice as a transparent and sterile detection medium to attain large detection volumes for muons and neutrinos from astrophysical sources. Photomultiplier tubes (PMTs) deployed in the South Pole

30.5 m
40°
Depth
0 m
810 m
10 m
1000 m
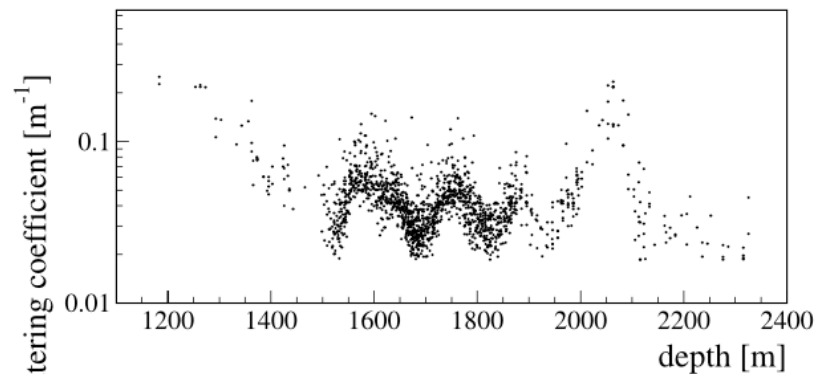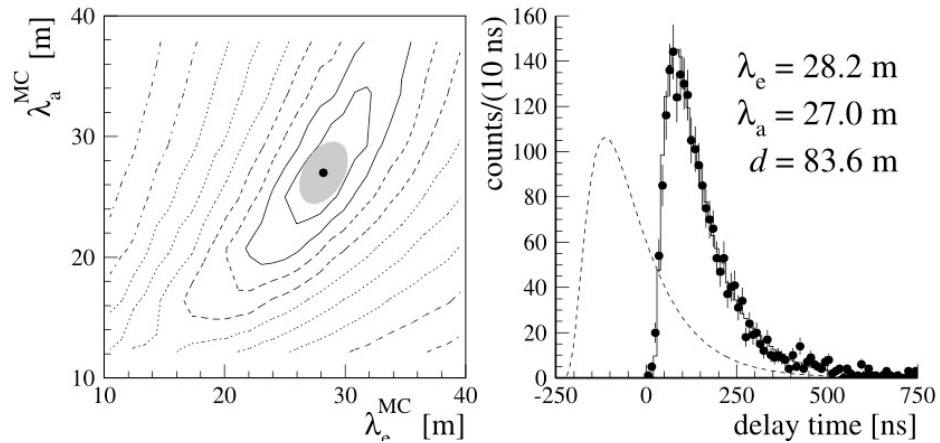
$\lambda_a = 59 \pm 1$ m, and

$$\frac{1}{\lambda_{bub}} = \frac{(28.6 \pm 1.1) - (0.025 \pm 0.001)z}{4(1-\tau)} \ m^{-1}$$

AMANDA-II: comprehensive ice model

2006

Optical properties of deep glacial ice at the South Pole

M. Ackermann,[1] J. Ahrens,[2] X. Bai,[3] M. Bartelt,[4] S. W. Barwick,[5] R. C. Bay,[6] T. Becka,[2] J. K. Becker,[4] K.-H. Becker,[7] P. Berghaus,[8] E. Bernardini,[1] D. Bertrand,[8] D. J. Boersma,[9] S. Böser,[1] O. Botner,[10] A. Bouchta,[10] O. Bouhali,[8] C. Burgess,[11] T. Burgess,[11] T. Castermans,[12] D. Chirkin,[13] B. Collin,[14] J. Conrad,[10] J. Cooley,[9] D. F. Cowen,[14] A. Davour,[10] C. De Clercq,[15] C. P. de los Heros,[10] P. Desiati,[9] T. DeYoung,[14] P. Ekström,[11] T. Feser,[2] T. K. Gaisser,[3] R. Ganugapati,[9] H. Geenen,[7] L. Gerhardt,[5] A. Goldschmidt,[13] A. Groß,[4] A. Hallgren,[10] F. Halzen,[9] K. Hanson,[9] D. H. Hardtke,[6] T. Harenberg,[7] T. Hauschildt,[3] K. Helbing,[13] M. Hellwig,[2] P. Herquet,[12] G. C. Hill,[9] J. Hodges,[9] D. Hubert,[15] B. Hughey,[9] P. O. Hulth,[11] K. Hultqvist,[11] S. Hundertmark,[11] J. Jacobsen,[13] K. H. Kampert,[7] A. Karle,[9] M. Kestel,[14] G. Kohnen,[12] L. Köpke,[2] M. Kowalski,[1] K. Kuehn,[5] R. Lang,[1] H. Leich,[1] M. Leuthold,[1] I. Liubarsky,[16] J. Lundberg,[10] J. Madsen,[17] P. Marciniewski,[10] H. S. Matis,[13] C. P. McParland,[13] T. Messarius,[4] Y. Minaeva,[11] P. Miočinović,[6] R. Morse,[9] K. Münich,[4] R. Nahnhauer,[1] J. W. Nam,[5] T. Neunhöffer,[2] P. Niessen,[3] D. R. Nygren,[13] P. Olbrechts,[15] A. C. Pohl,[10] R. Porrata,[6] P. B. Price,[6] G. T. Przybylski,[13] K. Rawlins,[9] E. Resconi,[1] W. Rhode,[4] M. Ribordy,[12] S. Richter,[9] J. Rodríguez Martino,[11] H.-G. Sander,[2] S. Schlenstedt,[1] D. Schneider,[9] R. Schwarz,[9] A. Silvestri,[5] M. Solarz,[6] G. M. Spiczak,[17] C. Spiering,[1] M. Stamatikos,[9] D. Steele,[9] P. Steffen,[1] R. G. Stokstad,[13] K.-H. Sulanke,[1] I. Taboada,[6] O. Tarasova,[1] L. Thollander,[11] S. Tilav,[3] W. Wagner,[4] C. Walck,[11] M. Walter,[1] Y.-R. Wang,[9] C. H. Wiebusch,[7] R. Wischnewski,[1] H. Wissing,[1] and K. Woschnagg[6]

[1] We have remotely mapped optical scattering and absorption in glacial ice at the South Pole for wavelengths between 313 and 560 nm and depths between 1100 and 2350 m. We used pulsed and continuous light sources embedded with the AMANDA neutrino telescope, an array of more than six hundred photomultiplier tubes buried deep in the ice. At depths greater than 1300 m, both the scattering coefficient and absorptivity follow vertical variations in concentration of dust impurities, which are seen in ice cores from other Antarctic sites and which track climatological changes. The scattering coefficient varies by a factor of seven, and absorptivity (for wavelengths less than ~450 nm) varies by a factor of three in the depth range between 1300 and 2300 m, where four dust peaks due to stadials in the late Pleistocene have been identified. In our absorption data, we also identify a broad peak due to the Last Glacial Maximum around 1300 m. In the scattering data, this peak is partially masked by scattering on residual air bubbles, whose contribution dominates the scattering coefficient in shallower ice but vanishes at
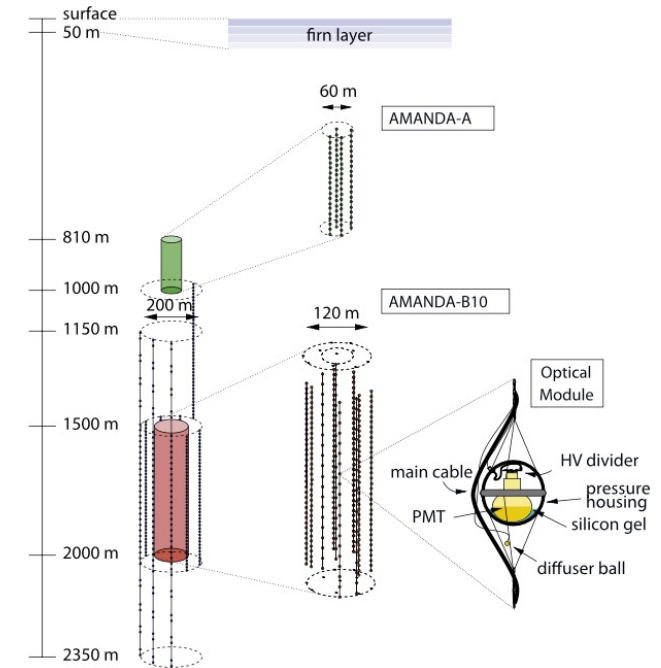
"millennium" ice model followed up with AHA (unfolded and extrapolated) and WHAM! (updated with IceCube flasher data)

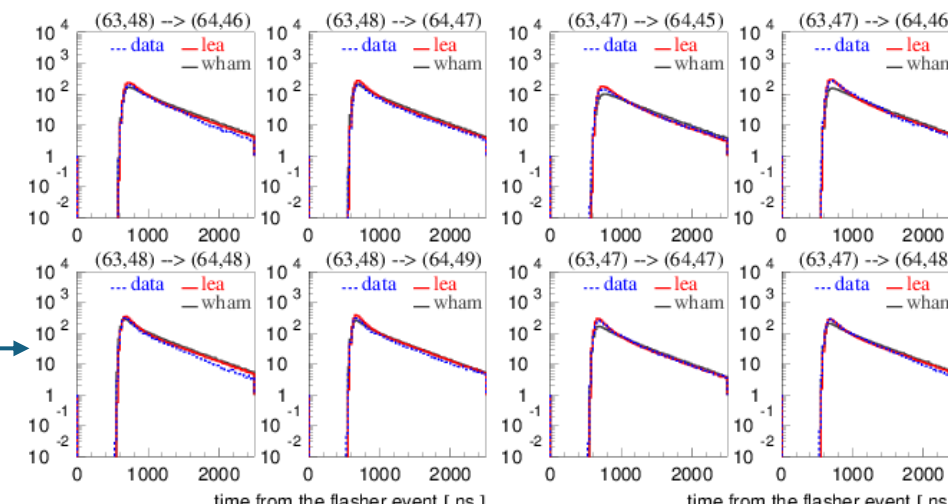# AMANDA-era ice models

2011
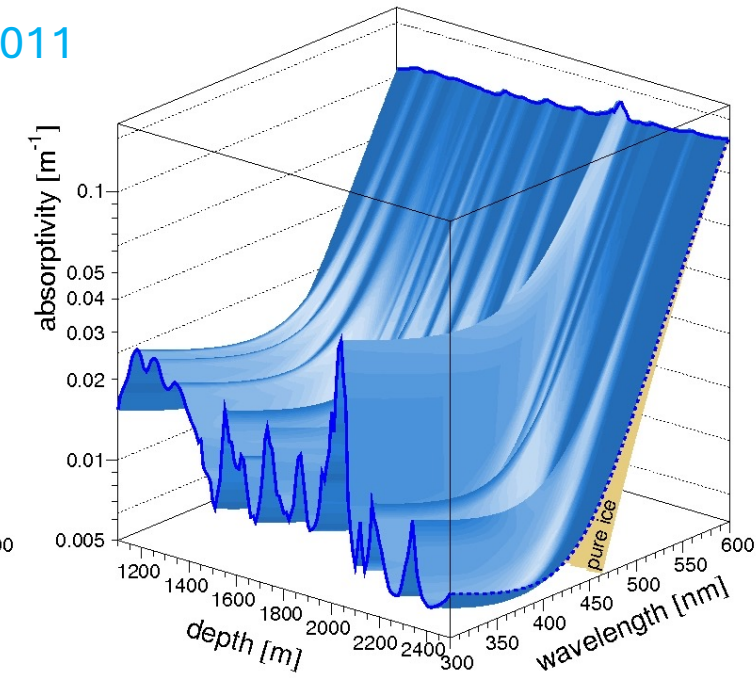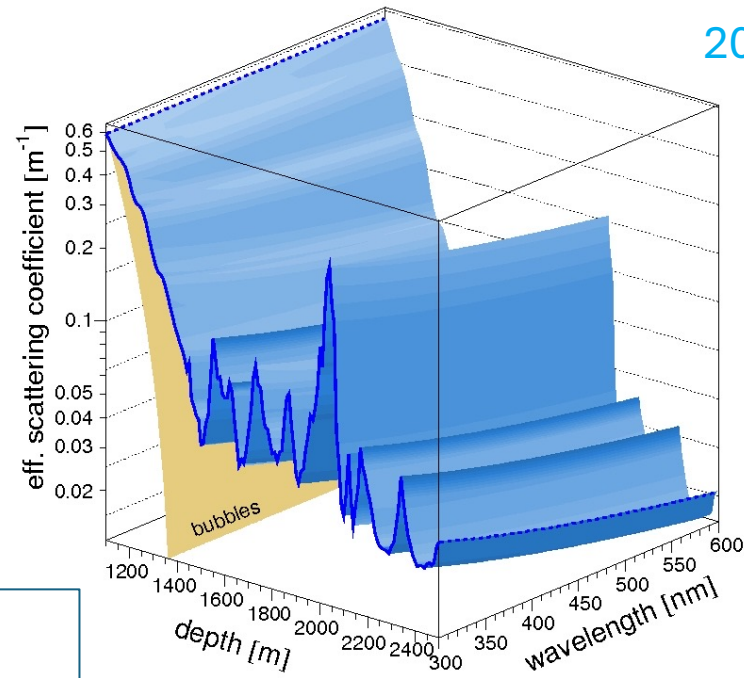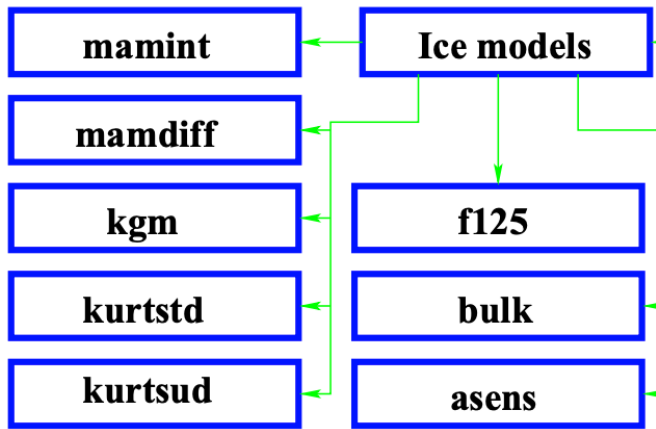
Kurt
KGM (Kurt-Gary)
MAM (modified absorption)   } 1995-2003
Millennium/Y2K

AHA   2006-2007

Lordi

WHAM! (Water Hardened Antarctic Measurement)

Models with an IceCube wiki page

Comparison with SPICE family (lea)

mamint
mamdiff
kgm
kurtstd
kurtsud

Ice models
f125
bulk
asens

AMANDA-II: comprehensive ice model
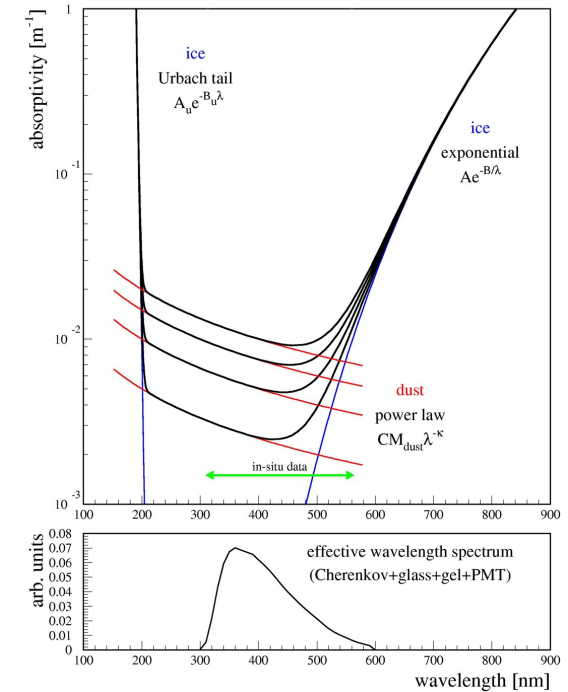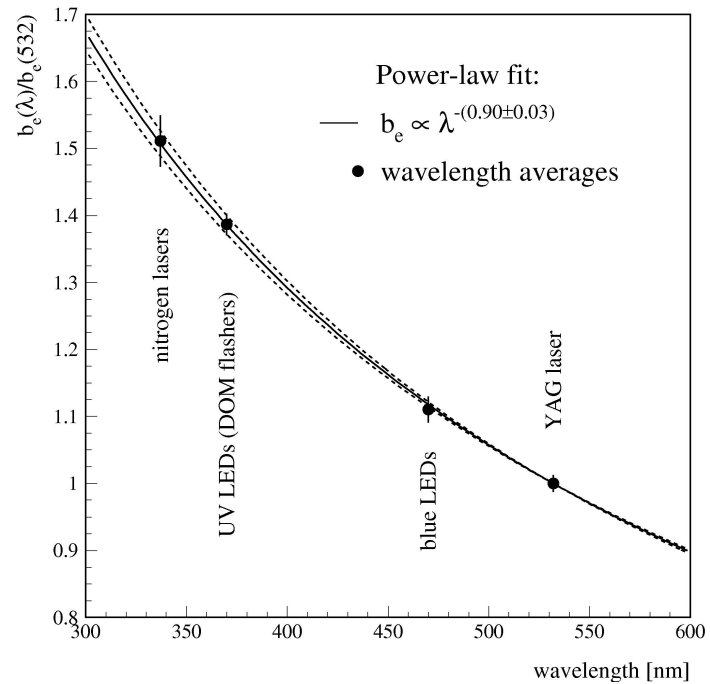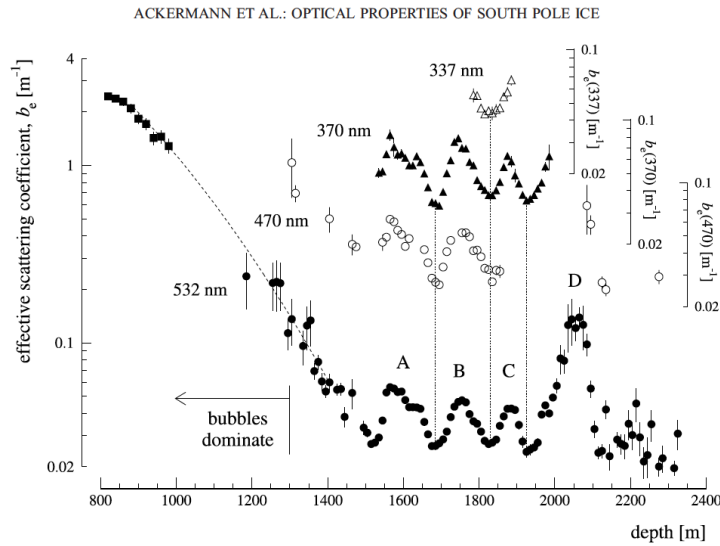
Ice is extremely transparent between 200 nm and 500 nm
Ice is very transparent at depths below 1350 m
Scattering and absorption are determined by dust concentration
Wavelength dependence of dust scattering and absorption follow power law
Wavelength dependence was verified with IceCube, but is still used basically unchanged

Trapped air bubbles and their conversion into air hydrates

At some depth between 0 and 200 m air bubbles become trapped and are squeezed into the ice as ice packs under pressure.
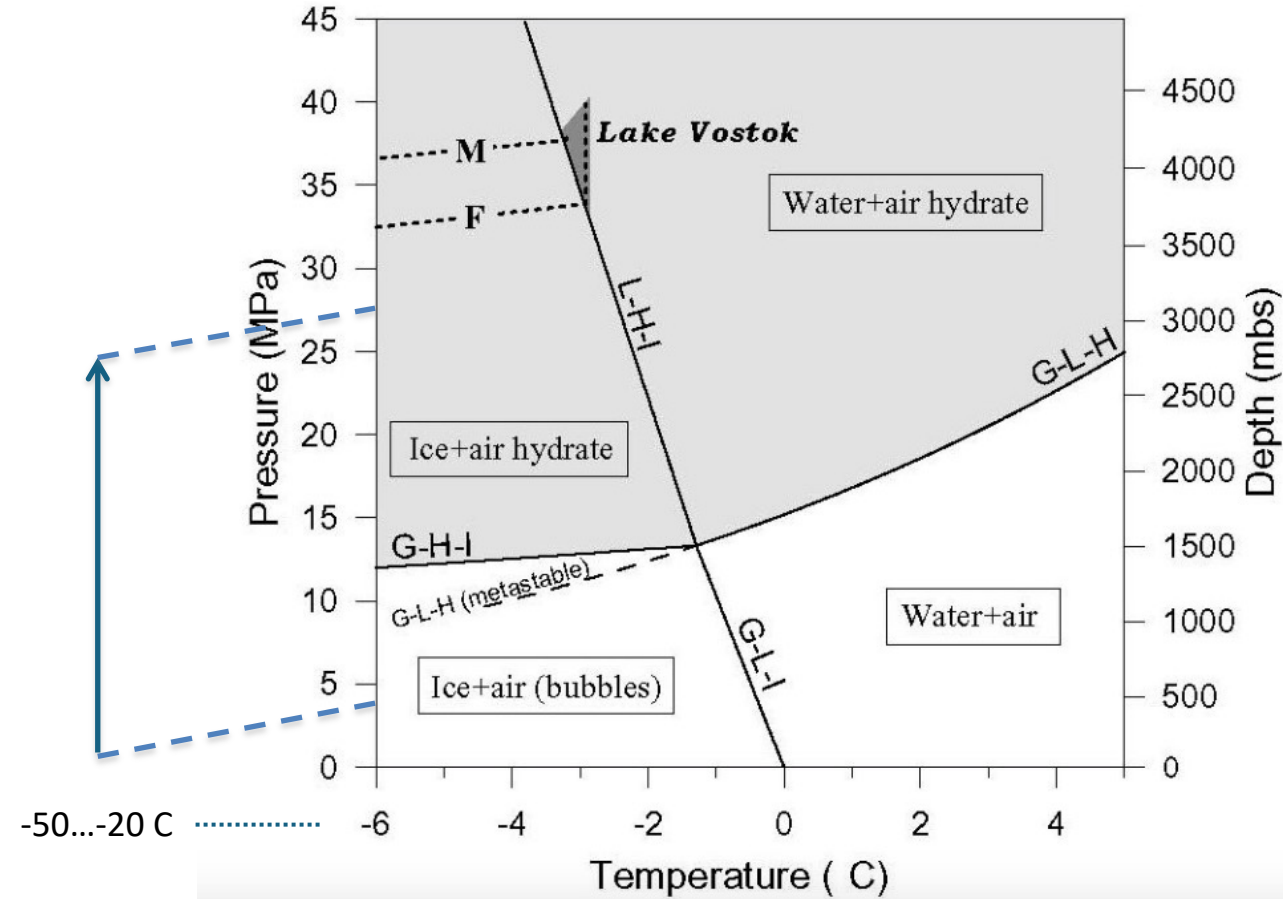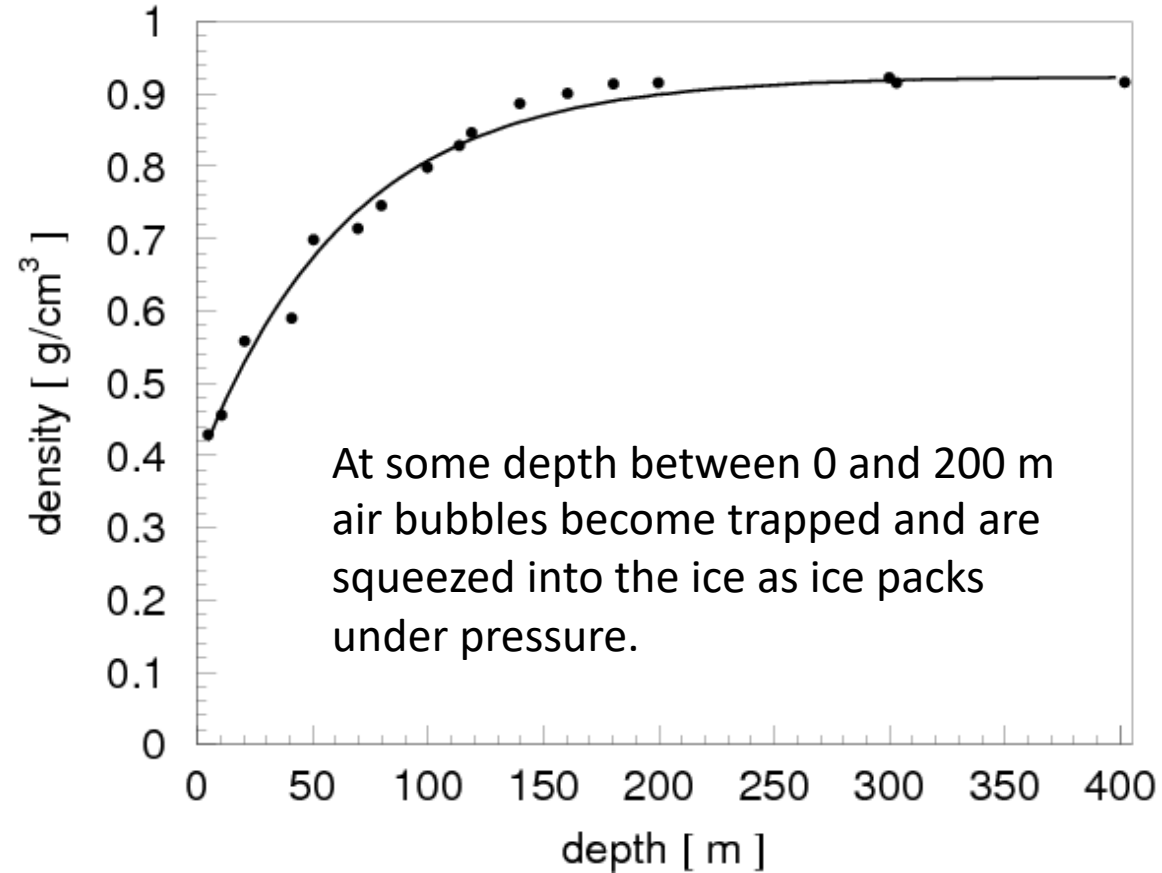
At depth of 1350 m all air bubbles have converted into air hydrates, which have the same refractive index as ice, so no longer a nuisance

Ice layer parametrization
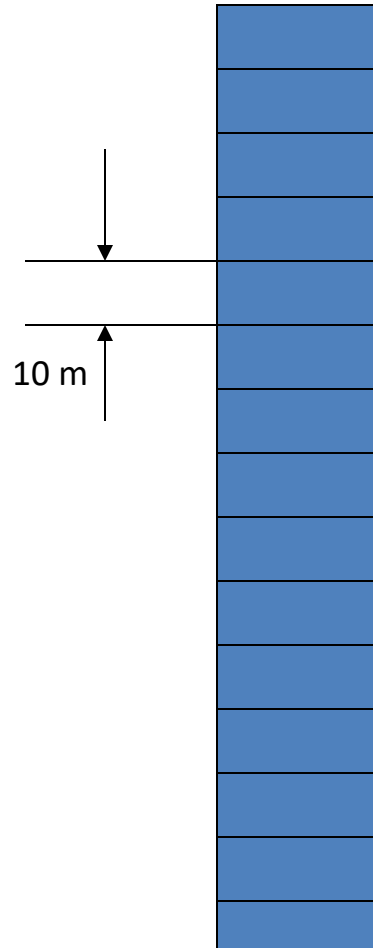
In each 10-meter layer define:
- scattering
- absorption
- ice crystal density

10 m
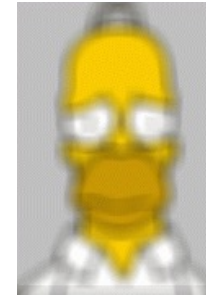
scattering → Source is blurred

absorption → Source is dimmer

a = inverse absorption length $(1/\lambda_{abs})$
b = inverse scattering length $(1/\lambda_{sca})$

Photon tracking with tables
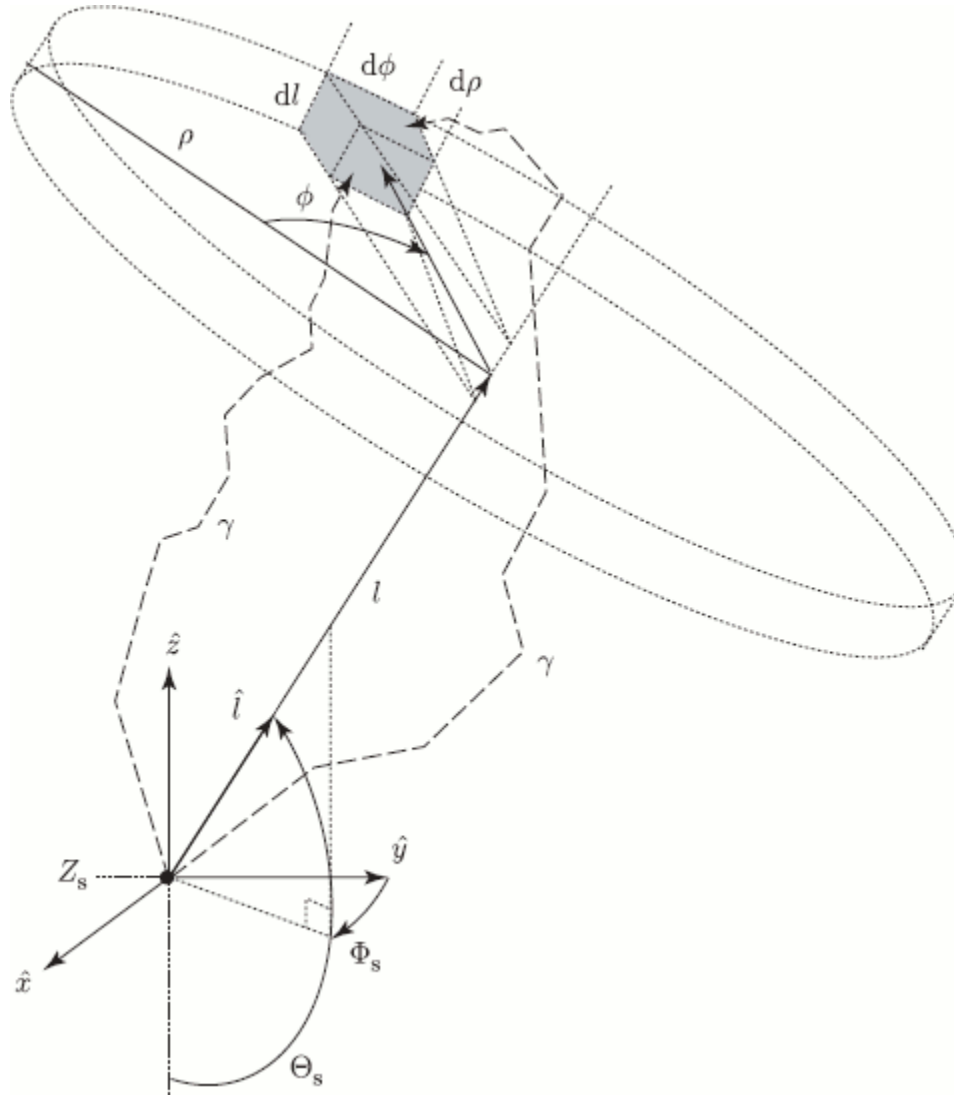
• First, run photonics to fill space with photons, tabulate the result

• Create such tables for nominal light sources: cascade and uniform half-muon

• Simulate photon propagation by looking up photon density in tabulated distributions

→ Table generation is slow
→ Simulation suffers from a wide range of binning artifacts
→ Simulation is also slow! (most time is spent loading the tables)

Direct photon tracking

photon propagation code (ppc) or OpenCL simulation (clsim)

propagate photons directly when needed

```
insert photon
     │
     ▼
length to absorption ──────► distance to next scatter
                                      │
                                      ▼
scatter ◄──── propagate to next scatter
   ▲                    ▲              │
   │                    │              ▼
```

insert photon

length to absorption → distance to next scatter

scatter ← propagate to next scatter

check for intersection with OMs → hit

Check for distance to absorption → lost
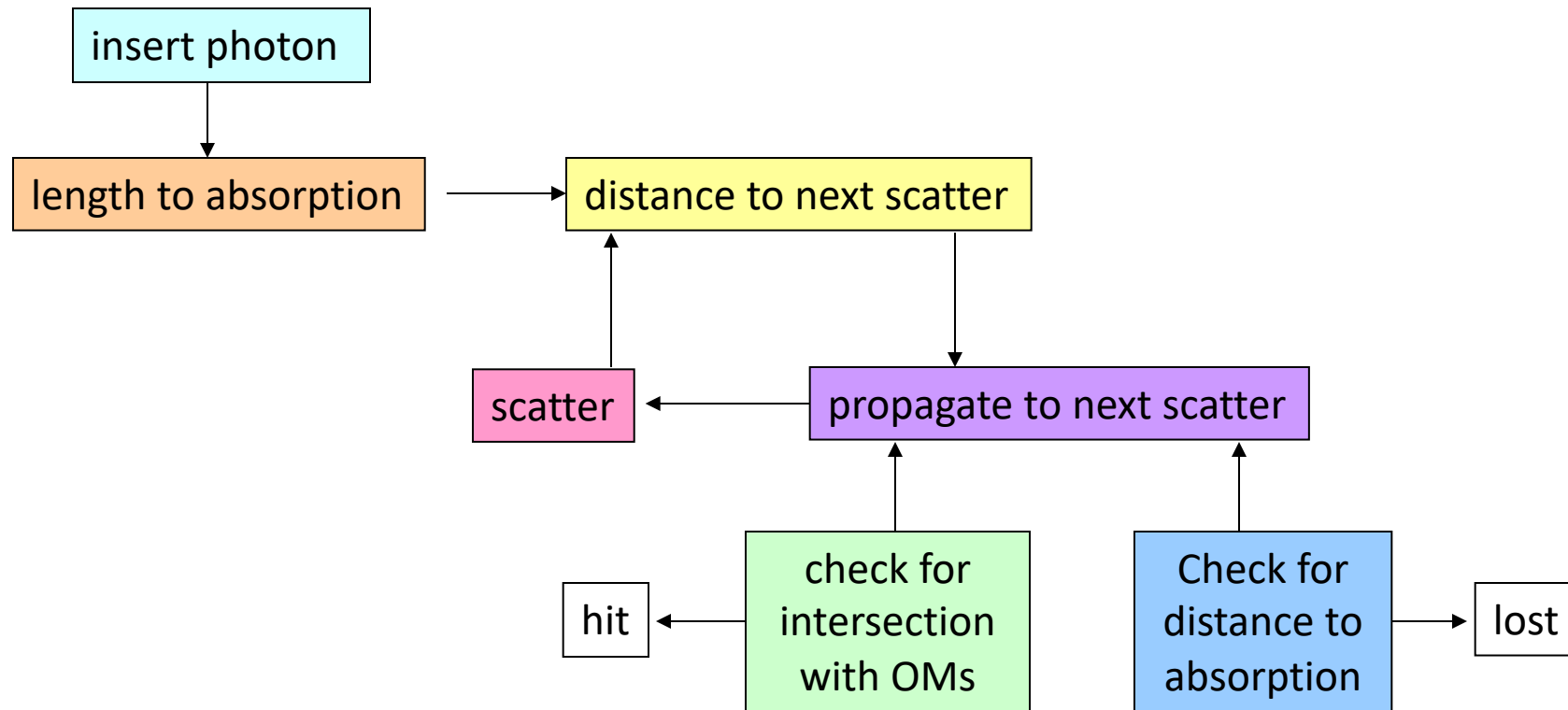
Simulation: Direct photon tracking

execution threads

propagation steps

scattering (rotation)

photon absorbed

new photon created
(taken from the pool)

threads complete
their execution
(no more photons)

Same code used for both
flasher simulation/ice
calibration and
muon/physics data
simulation
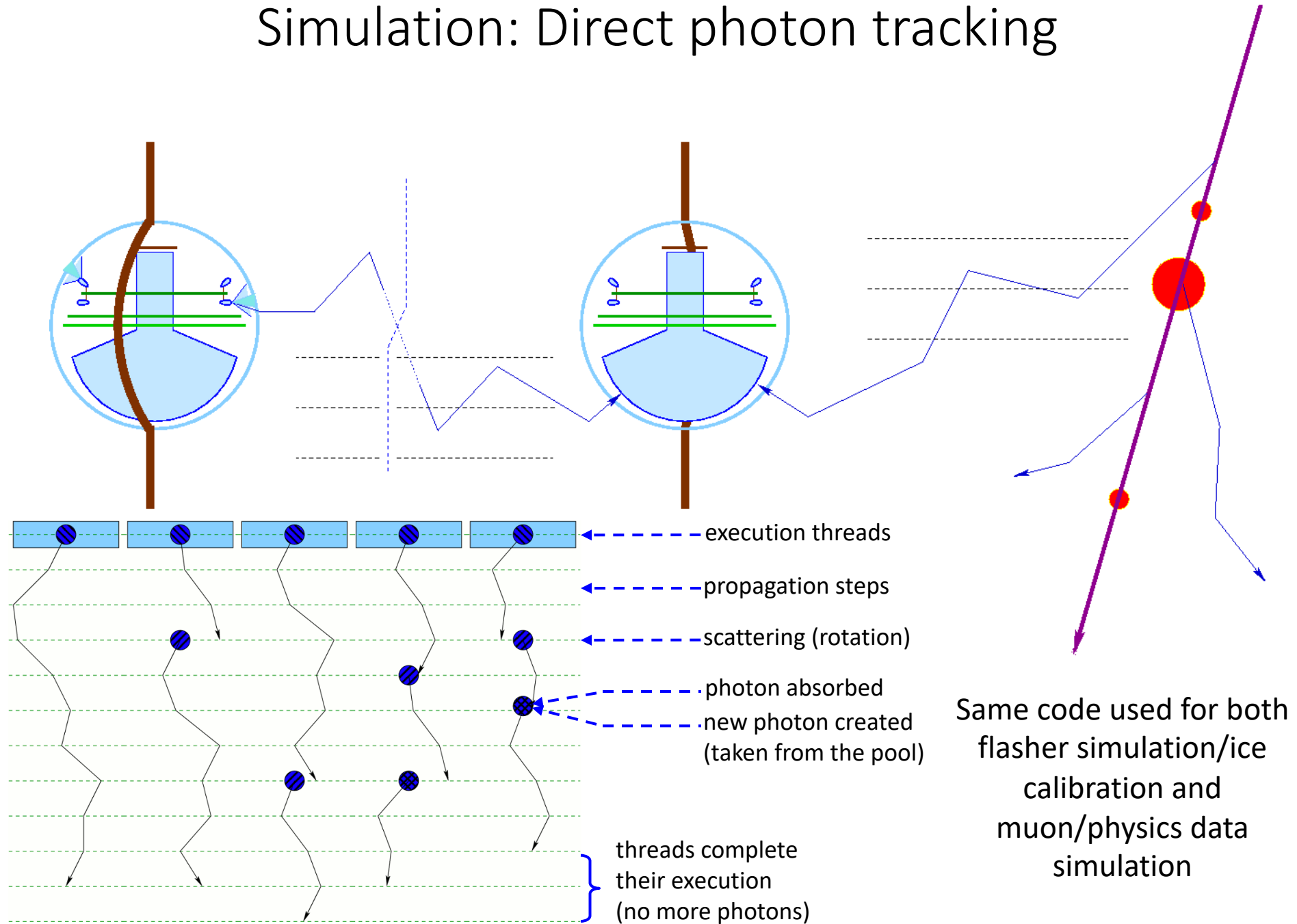
Oversized DOM treatment

This is a crucial optimization.

The oversize model was chosen carefully to produce the best possible agreement with the nominal x1 case.

nominal DOM
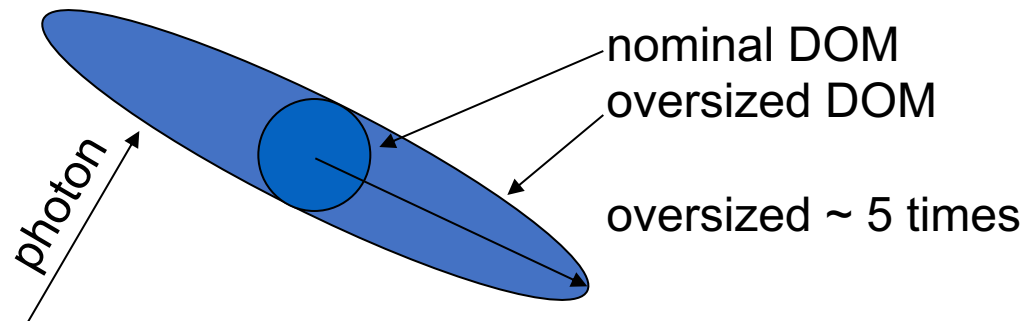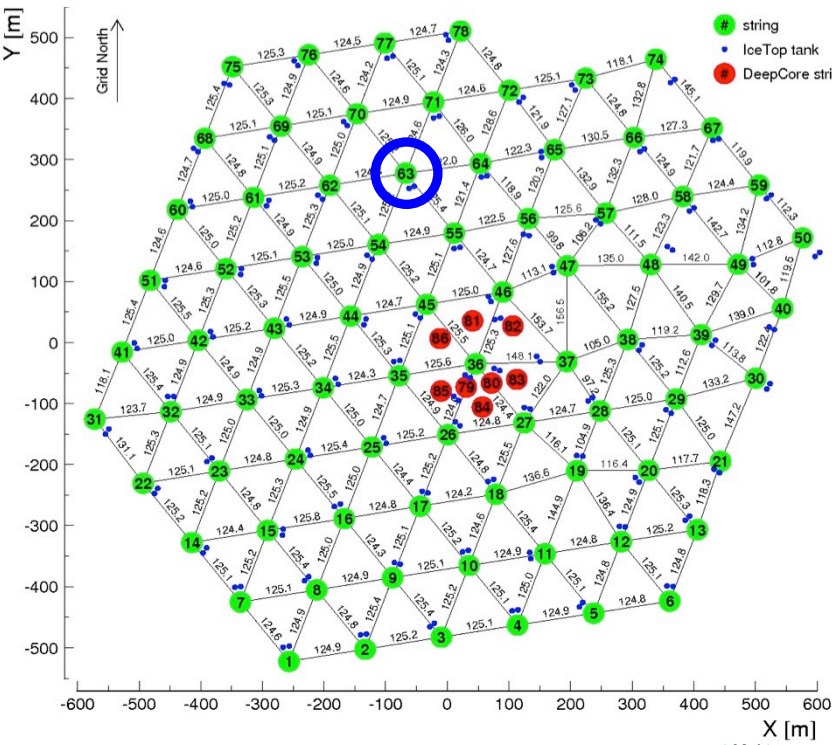oversized DOM

photon

oversized ~ 5 times

Some bias is unavoidable since DOMs occupy larger space:
      x1: diameter of 33 cm
      x5: 1.65 m
      x16: 5.3 m

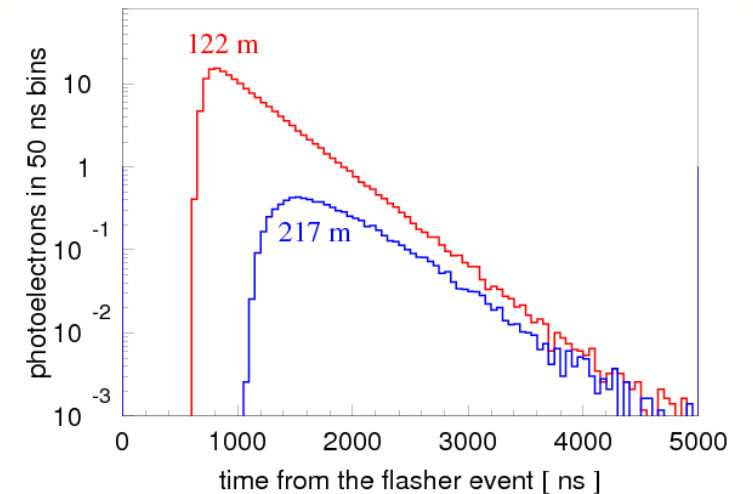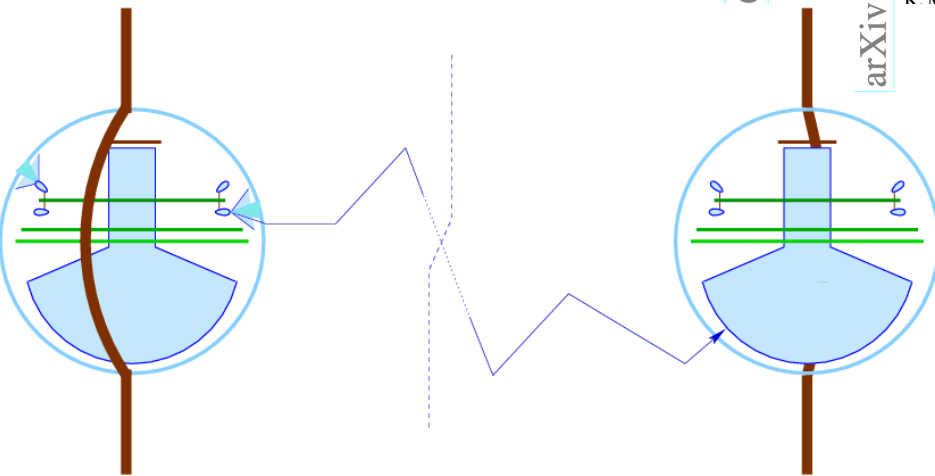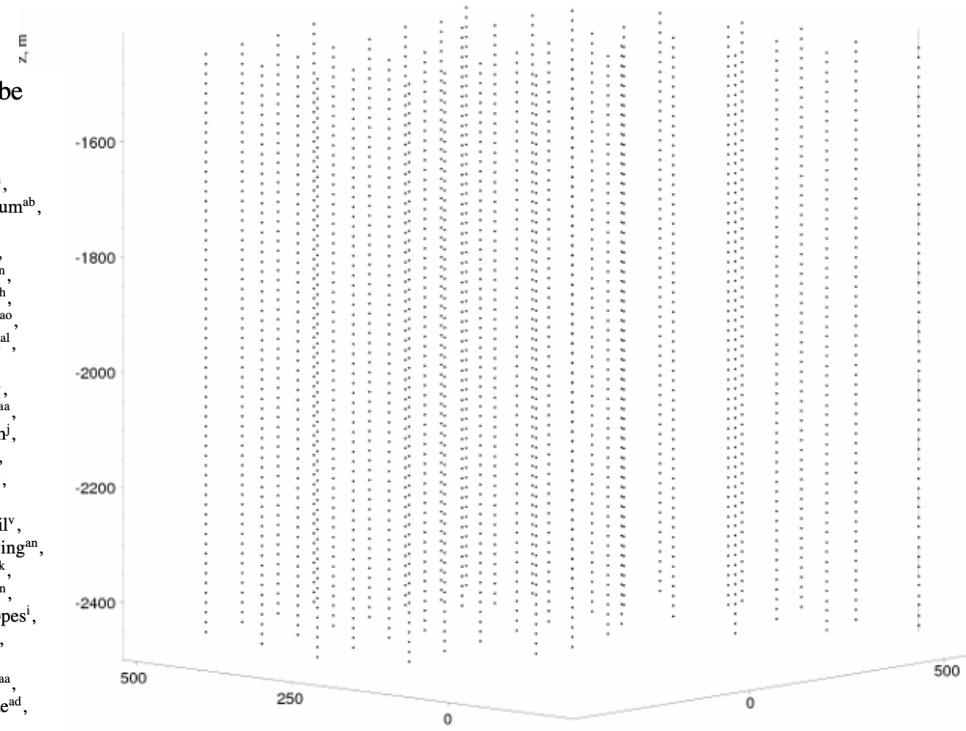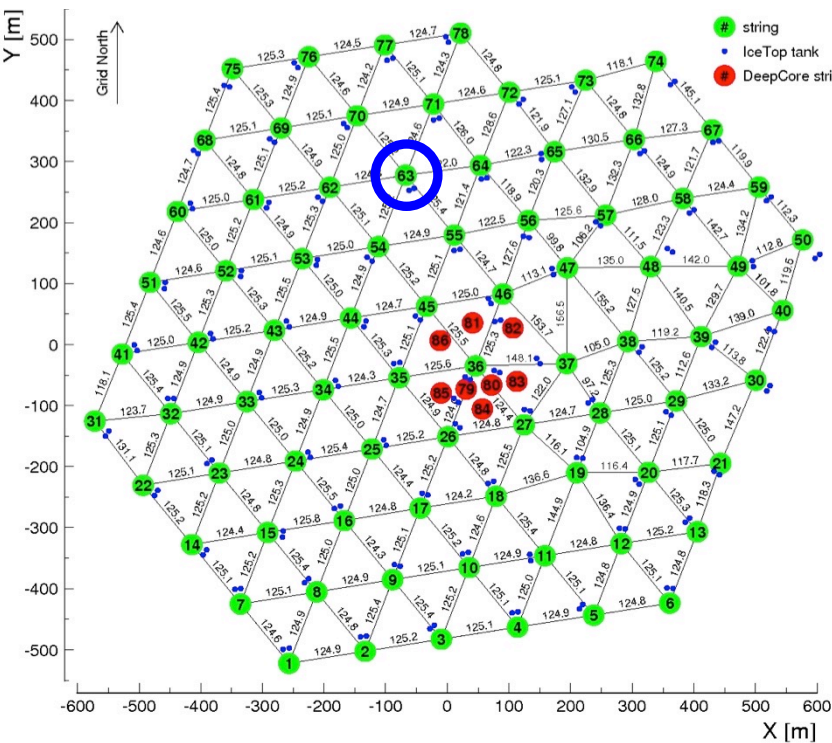# SPICE models: simultaneous direct fit to all layers

Measurement of South Pole ice transparency with the IceCube LED calibration system

2013

M. G. Aartsen[b], R. Abbasi[aa], Y. Abdou[v], M. Ackermann[ao], J. Adams[o], J. A. Aguilar[u], M. Ahlers[aa], D. Altmann[i], J. Auffenberg[aa], X. Bai[ae,1], M. Baker[aa], S. W. Barwick[w], V. Baum[ab], R. Bay[g], J. J. Beatty[q,r], S. Bechet[l], J. Becker Tjus[j], K.-H. Becker[an], M. Bell[al], M. L. Benabderrahmane[ao], S. BenZvi[aa], J. Berdermann[ao], P. Berghaus[ao], D. Berley[p], E. Bernardini[ao], A. Bernhard[ad], D. Bertrand[l], D. Z. Besson[y], G. Binder[h,g], D. Bindig[an], M. Bissok[a], E. Blaufuss[p], J. Blumenthal[a], D. J. Boersma[am], S. Bohaichuk[t], C. Bohm[ah], D. Bose[m], S. Böser[k], O. Botner[am], L. Brayeur[m], A. M. Brown[o], R. Bruijn[x], J. Brunner[ao], S. Buitink[m], M. Carson[v], J. Casey[e], M. Casier[m], D. Chirkin[aa,5,*], B. Christy[p], K. Clark[al], F. Clevermann[s], S. Cohen[x], D. F. Cowen[al,ak], A. H. Cruz Silva[ao], M. Danninger[ah], J. Daughhetee[e], J. C. Davis[q], C. De Clercq[m], S. De Ridder[v], P. Desiati[aa], M. de With[i], T. DeYoung[al], J. C. Díaz-Vélez[aa], M. Dunkman[al], R. Eagan[al], B. Eberhardt[ab], J. Eisch[aa], R. W. Ellsworth[p], S. Euler[a], P. A. Evenson[ae], O. Fadiran[a], A. R. Fazely[f], A. Fedynitch[j], J. Feintzeig[aa], T. Feusels[v], K. Filimonov[g], C. Finley[ah], T. Fischer-Wasels[an], S. Flis[ah], A. Franckowiak[k], R. Franke[ao], K. Frantzen[s], T. Fuchs[s], T. K. Gaisser[ae], J. Gallagher[z], L. Gerhardt[h,g], L. Gladstone[aa], T. Glüsenkamp[ao], A. Goldschmidt[h], G. Golup[m], J. A. Goodman[p], D. Góra[ao], D. Grant[t], A. Groß[ad], M. Gurtner[an], C. Ha[h,g], A. Haj Ismail[v], A. Hallgren[am], F. Halzen[aa], K. Hanson[l], D. Heereman[l], P. Heimann[a], D. Heinen[a], K. Helbing[an], R. Hellauer[p], S. Hickford[o], G. C. Hill[b], K. D. Hoffman[p], R. Hoffmann[an], A. Homeier[k], K. Hoshina[aa], W. Huelsnitz[p,2], P. O. Hulth[ah], K. Hultqvist[ah], S. Hussain[ae], A. Ishihara[n], E. Jacobi[ao], J. Jacobsen[aa], G. S. Japaridze[d], K. Jero[aa], O. Jlelati[v], B. Kaminsky[ao], A. Kappes[i], T. Karg[ao], A. Karle[aa], J. L. Kelley[aa], J. Kiryluk[ai], F. Kislat[ao], J. Kläs[an], S. R. Klein[h,g], J.-H. Köhne[s], G. Kohnen[ac], H. Kolanoski[i], L. Köpke[ab], C. Kopper[a], S. Kopper[an], D. J. Koskinen[al], M. Kowalski[k], M. Krasberg[aa], G. Kroll[ab], J. Kunnen[m], N. Kurahashi[aa], T. Kuwabara[ae], M. Labare[m], H. Landsman[aa], M. J. Larson[aj], M. Lesiak-Bzdak[ai], J. Leute[ad], J. Lünemann[ab], J. Madsen[ag], R. Maruyama[aa], K. Mase[n], H. S. Matis[h], F. McNally[aa], K. Meagher[p], M. Merck[aa], P. Mészáros[ak,al], T. Meures[l], S. Miarecki[h,g], E. Middell[ao], N. Milke[s], J. Miller[m], L. Mohrmann[ao], T. Montaruli[u,3], R. Morse[aa], R. Nahnhauer[ao], U. Naumann[an], H. Niederhausen[ai], S. C. Nowicki[t], D. R. Nygren[h], A. Obertacke[an], S. Odrowski[ad], A. Olivas[p], M. Olivo[j], A. O'Murchadha[l], L. Paul[a], J. A. Pepper[aj], C. Pérez de los Heros[am], C. Pfendner[q], D. Pieloth[s], N. Pirk[ao], J. Posselt[an], P. B. Price[g], G. T. Przybylski[h], L. Rädel[a], K. Rawlins[c], P. Redl[p], E. Resconi[ad], W. Rhode[s], M. Ribordy[x], M. Richman[p], B. Riedel[aa], J. P. Rodrigues[aa], F. Scott[q], T. Ruhe[s], B. Ruzybayev[ae], D. Ryckbosch[v], S. M. Saba[j], T. Salameh[al], H.-G. Sander[ab], M. Santander[aa], S. Sarkar[af], K. Schatto[ab], M. Scheel[a], F. Scheriau[s], T. Schmidt[p], M. Schmitz[s], S. Schoenen[a], S. Schöneberg[j], L. Schönherr[a], A. Schönwald[ao], A. Schukraft[a], L. Schulte[k], O. Schulz[ad], D. Seckel[ae], S. H. Seo[ah], Y. Sestayo[ad], S. Seunarine[ag], C. Sheremata[t], M. W. E. Smith[al], M. Soiron[a], D. Soldin[an], G. M. Spiczak[ag], C. Spiering[ao], M. Stamatikos[q,4], T. Stanev[ae], A. Stasik[k], T. Stezelberger[h], R. G. Stokstad[h], A. Stößl[ao], E. A. Strahler[m], R. Ström[am], G. W. Sullivan[p], H. Taavola[am], I. Taboada[e], A. Tamburro[ae], S. Ter-Antonyan[f], S. Tilav[ae], P. A. Toale[aj], S. Toscano[aa], M. Usner[k], D. van der Drift[h,g], N. van Eijndhoven[m], A. Van Overloop[v], J. van Santen[aa], M. Vehring[a], M. Voge[k], M. Vraeghe[v], C. Walck[ah], T. Waldenmaier[i], M. Wallraff[a], R. Wasserman[al], Ch. Weaver[aa], M. Wellons[aa], C. Wendt[aa], S. Westerhoff[aa], N. Whitehorn[aa], K. Wiebe[ab], C. H. Wiebusch[a], D. R. Williams[aj], H. Wissing[p], M. Wolf[ah], T. R. Wood[t], C. Xu[ae], D. L. Xu[aj], X. W. Xu[f], J. P. Yanez[ao], G. Yodh[w], S. Yoshida[n],

122 m

217 m

SPICE models: simultaneous direct fit to all layers

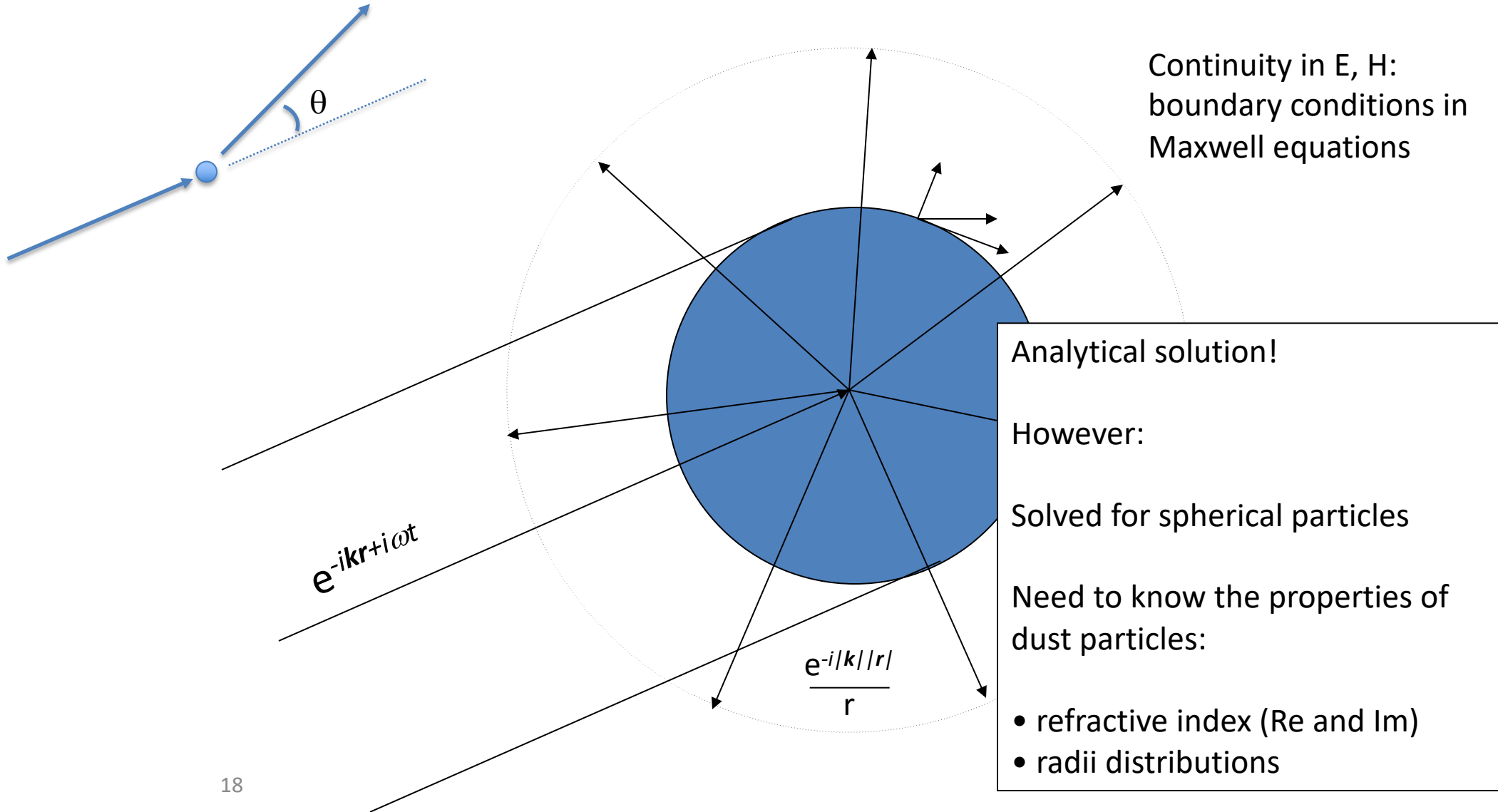## Measurement of South Pole ice transparency with the IceCube LED calibration system

2013

M. G. Aartsen[b], R. Abbasi[aa], Y. Abdou[v], M. Ackermann[ao], J. Adams[o], J. A. Aguilar[u], M. Ahlers[aa], D. Altmann[i], J. Auffenberg[aa], X. Bai[ae,1], M. Baker[aa], S. W. Barwick[w], V. Baum[ab], R. Bay[g], J. J. Beatty[q,r], S. Bechet[l], J. Becker Tjus[j], K.-H. Becker[an], M. Bell[al], M. L. Benabderrahmane[ao], S. BenZvi[aa], J. Berdermann[ao], P. Berghaus[ao], D. Berley[p], E. Bernardini[ao], A. Bernhard[ad], D. Bertrand[l], D. Z. Besson[y], G. Binder[h,g], D. Bindig[an], M. Bissok[a], E. Blaufuss[p], J. Blumenthal[a], D. J. Boersma[am], S. Bohaichuk[t], C. Bohm[ah], D. Bose[m], S. Böser[k], O. Botner[am], L. Brayeur[m], A. M. Brown[o], R. Bruijn[x], J. Brunner[ao], S. Buitink[m], M. Carson[v], J. Casey[e], M. Casier[m], D. Chirkin[aa,5,*], B. Christy[p], K. Clark[al], F. Clevermann[s], S. Cohen[x], D. F. Cowen[al,ak], A. H. Cruz Silva[ao], M. Danninger[ah], J. Daughhetee[e], J. C. Davis[q], C. De Clercq[m], S. De Ridder[v], P. Desiati[aa], M. de With[i], T. DeYoung[al], J. C. Díaz-Vélez[aa], M. Dunkman[al], R. Eagan[al], B. Eberhardt[ab], J. Eisch[aa], R. W. Ellsworth[p], S. Euler[a], P. A. Evenson[ae], O. Fadiran[a], A. R. Fazely[f], A. Fedynitch[j], J. Feintzeig[aa], T. Feusels[v], K. Filimonov[g], C. Finley[ah], T. Fischer-Wasels[an], S. Flis[ah], A. Franckowiak[k], R. Franke[ao], K. Frantzen[s], T. Fuchs[s], T. K. Gaisser[ae], J. Gallagher[z], L. Gerhardt[h,g], L. Gladstone[aa], T. Glüsenkamp[ao], A. Goldschmidt[h], G. Golup[m], J. A. Goodman[p], D. Góra[ao], D. Grant[t], A. Groß[ad], C. Ha[h,g], A. Haj Ismail[v], A. Hallgren[am], F. Halzen[aa], K. Hanson[l], D. Heereman[l], P. Heimann[a], D. Heinen[a], K. Helbing[an], R. Hellauer[p], S. Hickford[o], G. C. Hill[b], K. D. Hoffman[p], R. Hoffmann[an], A. Homeier[k], K. Hoshina[aa], W. Huelsnitz[p,2], P. O. Hulth[ah], K. Hultqvist[ah], S. Hussain[ae], A. Ishihara[n], E. Jacobi[ao], J. Jacobsen[aa], G. S. Japaridze[d], K. Jero[aa], O. Jlelati[v], B. Kaminsky[ao], A. Kappes[i], T. Karg[ao], A. Karle[aa], J. L. Kelley[aa], J. Kiryluk[ai], F. Kislat[ao], J. Kläs[an], S. R. Klein[h,g], J.-H. Köhne[s], G. Kohnen[ac], H. Kolanoski[i], L. Köpke[ab], C. Kopper[aa], S. Kopper[an], D. J. Koskinen[al], M. Kowalski[k], M. Krasberg[aa], G. Kroll[ab], J. Kunnen[m], N. Kurahashi[aa], T. Kuwabara[ae], M. Labare[m], H. Landsman[aa], M. J. Larson[aj], M. Lesiak-Bzdak[ai], J. Leute[ad], J. Lünemann[ab], J. Madsen[ag], R. Maruyama[aa], K. Mase[n], H. S. Matis[h], F. McNally[aa], K. Meagher[p], M. Merck[aa], P. Mészáros[ak,al], T. Meures[l], S. Miarecki[h,g], E. Middell[ao], N. Milke[s], J. Miller[m], L. Mohrmann[ao], T. Montaruli[u,3], R. Morse[aa], R. Nahnhauer[ao], U. Naumann[an], H. Niederhausen[ai], S. C. Nowicki[t], D. R. Nygren[h], A. Obertacke[an], S. Odrowski[ad], A. Olivas[p], M. Olivo[j], A. O'Murchadha[l], L. Paul[a], J. A. Pepper[aj], C. Pérez de los Heros[am], C. Pfendner[q], D. Pieloth[s], N. Pirk[ao], J. Posselt[an], P. B. Price[g], G. T. Przybylski[h], L. Rädel[a], K. Rawlins[c], P. Redl[p], E. Resconi[ad], W. Rhode[s], M. Ribordy[x], M. Richman[p], B. Riedel[aa], J. P. Rodrigues[aa], F. Scott[q], T. Ruhe[s], B. Ruzybayev[ae], D. Ryckbosch[v], S. M. Saba[j], T. Salameh[al], H.-G. Sander[ab], M. Santander[aa], S. Sarkar[af], K. Schatto[ab], M. Scheel[a], F. Scheriau[s], T. Schmidt[p], M. Schmitz[s], S. Schoenen[a], S. Schöneberg[j], L. Schönherr[a], A. Schönwald[ao], A. Schukraft[a], L. Schulte[k], O. Schulz[ad], D. Seckel[ae], S. H. Seo[ah], Y. Sestayo[ad], S. Seunarine[ag], C. Sheremata[t], M. W. E. Smith[al], M. Soiron[a], D. Soldin[an], G. M. Spiczak[ag], C. Spiering[ao], M. Stamatikos[q,4], T. Stanev[ae], A. Stasik[k], T. Stezelberger[h], R. G. Stokstad[h], A. Stößl[ao], E. A. Strahler[m], R. Ström[am], G. W. Sullivan[p], H. Taavola[am], I. Taboada[e], A. Tamburro[ae], S. Ter-Antonyan[f], S. Tilav[ae], P. A. Toale[aj], S. Toscano[aa], M. Usner[k], D. van der Drift[h,g], N. van Eijndhoven[m], A. Van Overloop[v], J. van Santen[aa], M. Vehring[a], M. Voge[k], M. Vraeghe[v], C. Walck[ah], T. Waldenmaier[i], M. Wallraff[a], R. Wasserman[al], Ch. Weaver[aa], M. Wellons[aa], C. Wendt[aa], S. Westerhoff[aa], N. Whitehorn[aa], K. Wiebe[ab], C. H. Wiebusch[a], D. R. Williams[aj], H. Wissing[p], M. Wolf[ah], T. R. Wood[t], C. Xu[ae], D. L. Xu[aj], X. W. Xu[f], J. P. Yanez[ao], G. Yodh[w], S. Yoshida[n],

Mie scattering theory

θ

$e^{-ikr+i\omega t}$

$$\frac{e^{-i|k||r|}}{r}$$

Continuity in E, H: boundary conditions in Maxwell equations

Analytical solution!

However:

Solved for spherical particles

Need to know the properties of dust particles:

- refractive index (Re and Im)
- radii distributions

18

Approximation to Mie scattering
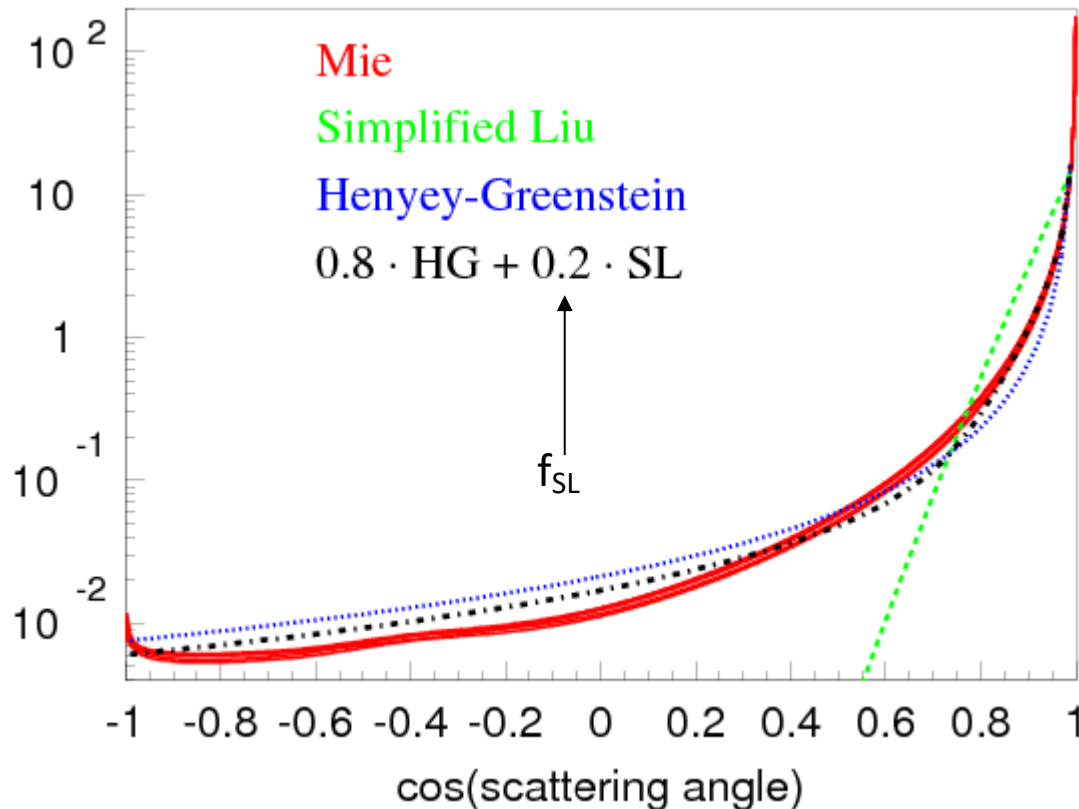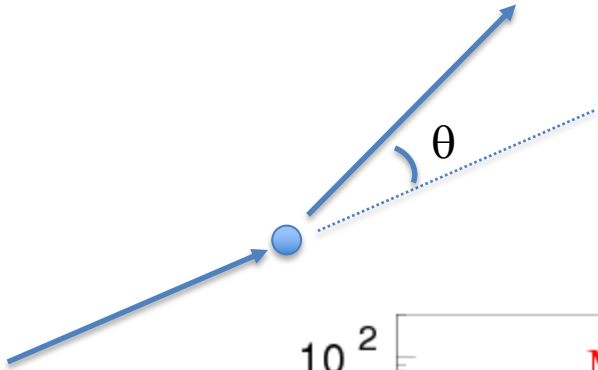
Simplified Liu:

$$p(\cos\theta) \sim (1 + \cos\theta)^\alpha, \quad \text{with} \quad \alpha = \frac{2g}{1-g}$$

Henyey-Greenstein:

$$p(\cos\theta) = \frac{1}{2}\frac{1-g^2}{[1+g^2 - 2g\cdot\cos\theta]^{3/2}}$$

Mie:

Describes scattering on acid, mineral, salt, and soot with concentrations and radii at SP collected in ice cores elsewhere in Antarctica
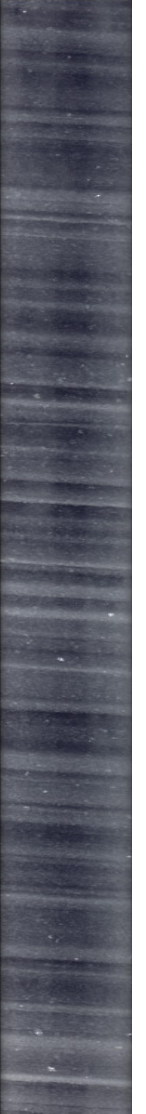
Dust logger mapping of the ice tilt
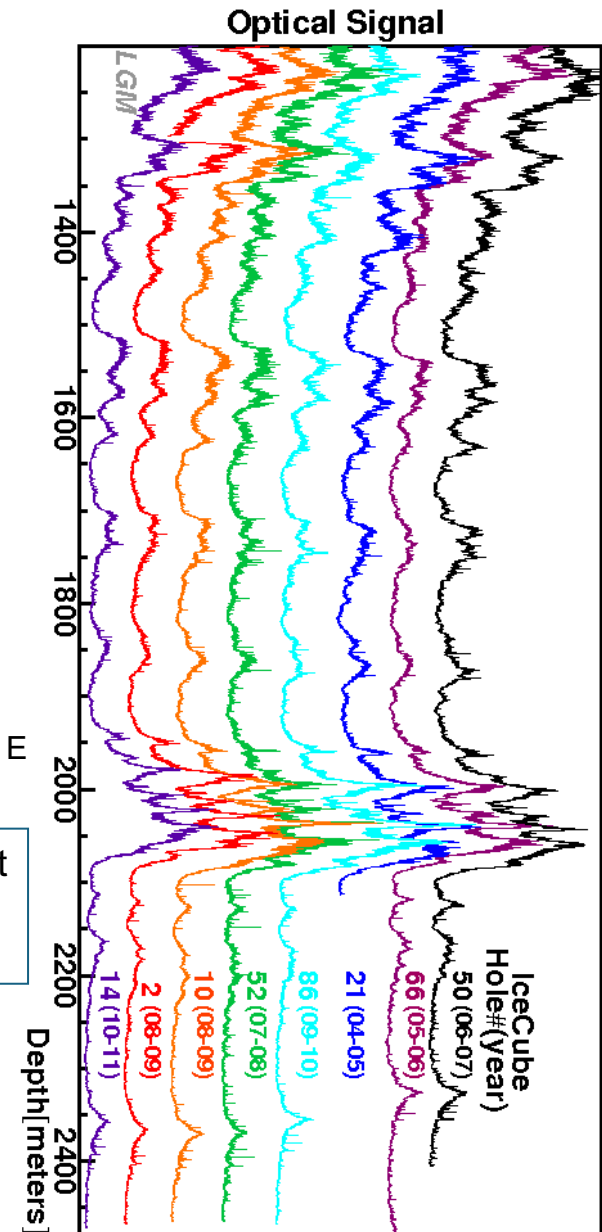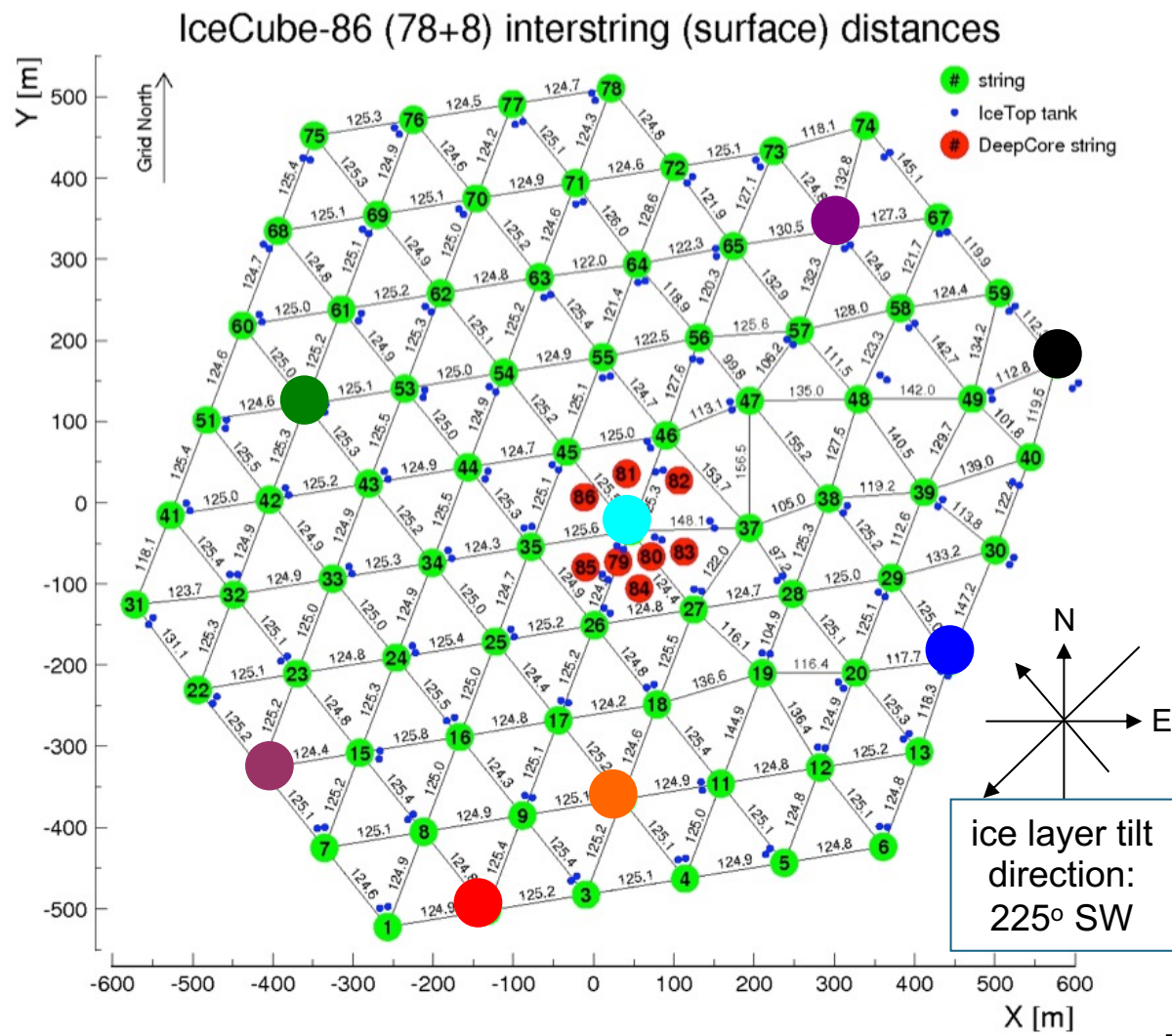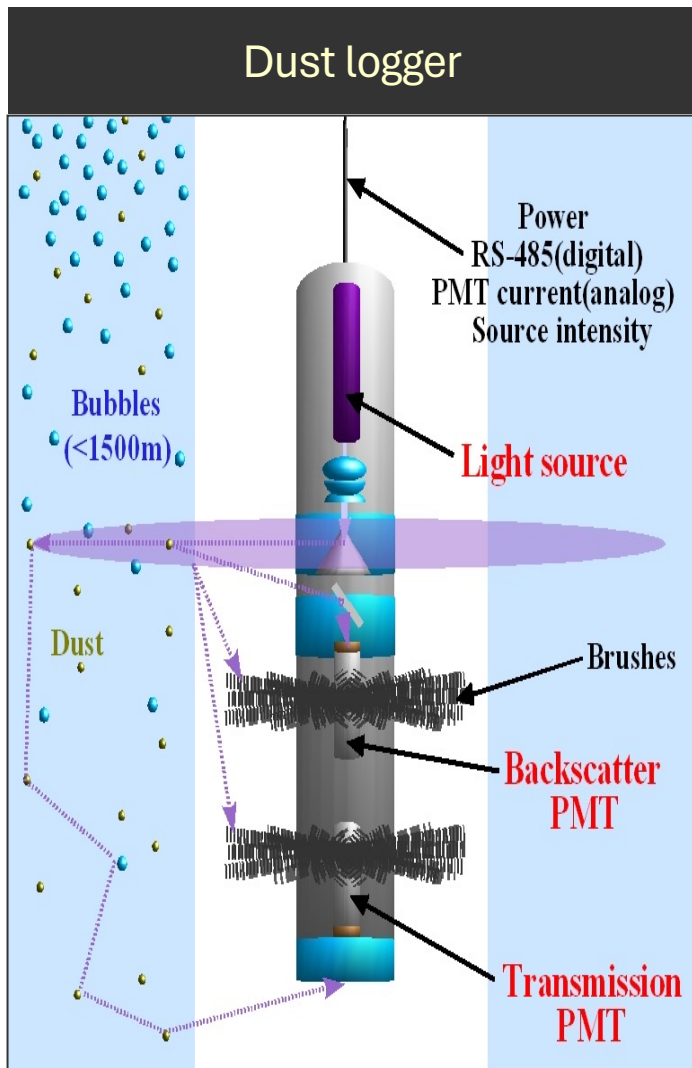
The ice layers (i.e. layers of ice with similar optical properties) change in depth by as much as 60 m when going from NE to SW corners of the detector

Dust logger mapping of the ice tilt

Dust logger

- Power
- RS-485(digital)
- PMT current(analog)
- Source intensity

Light source

Bubbles (<1500m)

Dust

Brushes

Backscatter PMT

Transmission PMT

South Pole glacial climate reconstruction from multi-borehole laser particulate stratigraphy

The IceCube Collaboration*

2013

*For full author list, see Appendix

ABSTRACT. The IceCube Neutrino Observatory and its prototype, AMANDA, were built in South Pole ice, using powerful hot-water drills to cleanly bore >100 holes to depths up to 2500 m. The construction of these particle physics detectors pro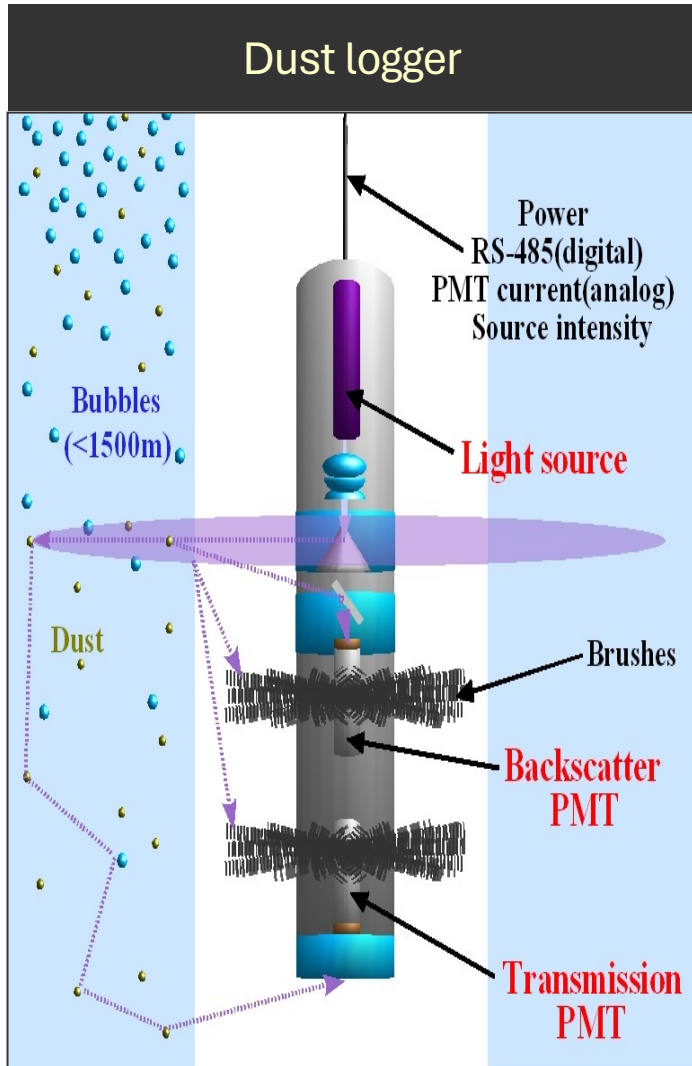vided a unique opportunity to examine the deep ice sheet using a variety of novel techniques. We made high-resolution particulate profiles with a laser dust logger in eight of the boreholes during detector commissioning between 2004 and 2010. The South Pole laser logs are among the most clearly resolved measurements of Antarctic dust strata during the last glacial period and can be used to reconstruct paleoclimate records in exceptional detail. Here we use manual and algorithmic matching to synthesize our South Pole measurements with ice-core and logging data from Dome C, East Antarctica. We derive impurity concentration, precision chronology, annual-layer thickness, local spatial variability, and identify several widespread volcanic ash depositions useful for dating. We also examine the interval around ~74 ka recently isolated with radiometric dating to bracket the Toba (Sumatra) supereruption.

INTRODUCTION

More than 50 years ago, Markov and Zheleznykh proposed using gigatons of transparent material underground as a detector of cosmic neutrinos (see Markov and Zheleznykh, 1986, and references therein). The IceCube Neutrino Observatory completed in December 2010 (IceCube Collaboration, 2006) and its predecessor, AMANDA, (Antarctic Muon and Neutrino Detector Array; AMANDA Collaboration, 2001), have applied this concept in the deep ice at the South Pole to study fundamental questions in physics and astrophysics. These telescopes use large volumes of ice to observe the subatomic charged particles produced by energetic neutrinos, that have fortuitously interacted via the weak force with nucleons in the ice near the detector. Muons, hadronic cascades and electromagnetic cascades generated by the neutrinos can be tracked via charged-particle Cherenkov radiation at ultraviolet and visible wavelengths with an embedded matrix of sensitive photo-multipliers. The density of sensors and size of the instrumented volume determine the threshold, resolution and practicably attainable upper limit of detected neutrino energies. Since the spectrum of cosmic neutrinos is presumed to roughly follow that of cosmic rays and fall steeply with energy, IceCube was designed at the kilometer scale to detect small fluxes of neutrinos in the 1 TeV to 1 PeV energy range over the lifetime of the experiment.

The buried component of IceCube consists of 5160 photomultiplier tubes, frozen into 86 boreholes and arrayed over 1 km³ from 1450 m to 2450 m depth (IceCube Collaboration, 2009). IceCube and AMANDA rely on the extreme clarity of Antarctic ice, at sufficient depths that all residual air bubbles originally trapped in surface snow have converted to hydrates. Air clathrate hydrate crystals have almost exactly the same refractive index as ice ($\Delta n/n \approx 4 \times 10^{-3}$; Uchida and others, 1995) and so are
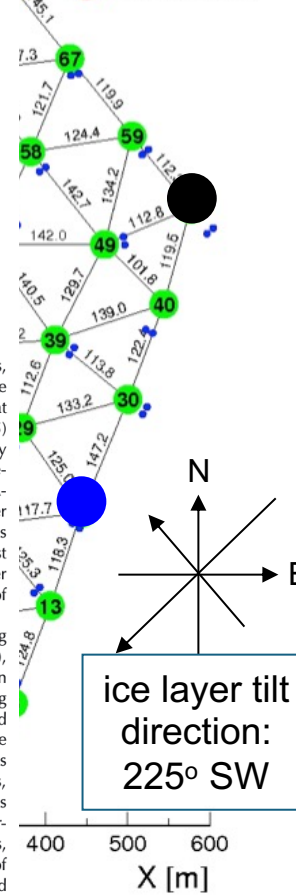
out a painstaking analysis of fresh Vostok ice-core samples, crucially, within a few weeks of coring and before the hydrates could revert back to air bubbles upon relaxation at the surface. Their work (Barkov and Lipenkov, 1985) presaged our discovery that South Pole ice is still bubbly at depths shallower than 1300 m. Bubble scattering prevented accurate directional reconstruction, and AMANDA-A was mainly effective as a subatomic particle calorimeter (Askebjer and others, 1995) but not as a telescope. Bubbles decrease in size with depth but persist until at least ~1350 m at South Pole, and to comparable or greater depths at every location we have studied in the interiors of Antarctica and Greenland.

IceCube construction depended critically on the drilling team and the 5 MW Enhanced Hot-Water Drill (EHWD), capable of boring 20 holes, each 2500 m deep and 60 cm in diameter, in a 2 month season. This massive ice-drilling project has enabled us to investigate South Pole ice and create synergies with other disciplines. Our studies to date include precision measurements of optical properties (Woschnagg and Price, 2001; Ackermann and others, 2006; IceCube Collaboration, 2013); acoustic properties (IceCube Collaboration, 2010, 2011); glaciological properties such as flow, shear and temperature (Price and others, 2002); and paleoclimatology, including a reconstruction of surface roughness as a proxy for cyclonic activity (Bay and others, 2010).

A principal aspect of calibrating the IceCube detector has been to map scattering and absorption of light in the deep ice. Bubble-free Antarctic ice is the purest natural solid on Earth, and the most transparent at ultraviolet to visible wavelengths. Photons with wavelengths shorter than ~200 nm are strongly attenuated by electronic absorption; for wavelengths longer than ~600 nm, molecular absorption dominates. Between 200 and 600 nm, transmis-

tances
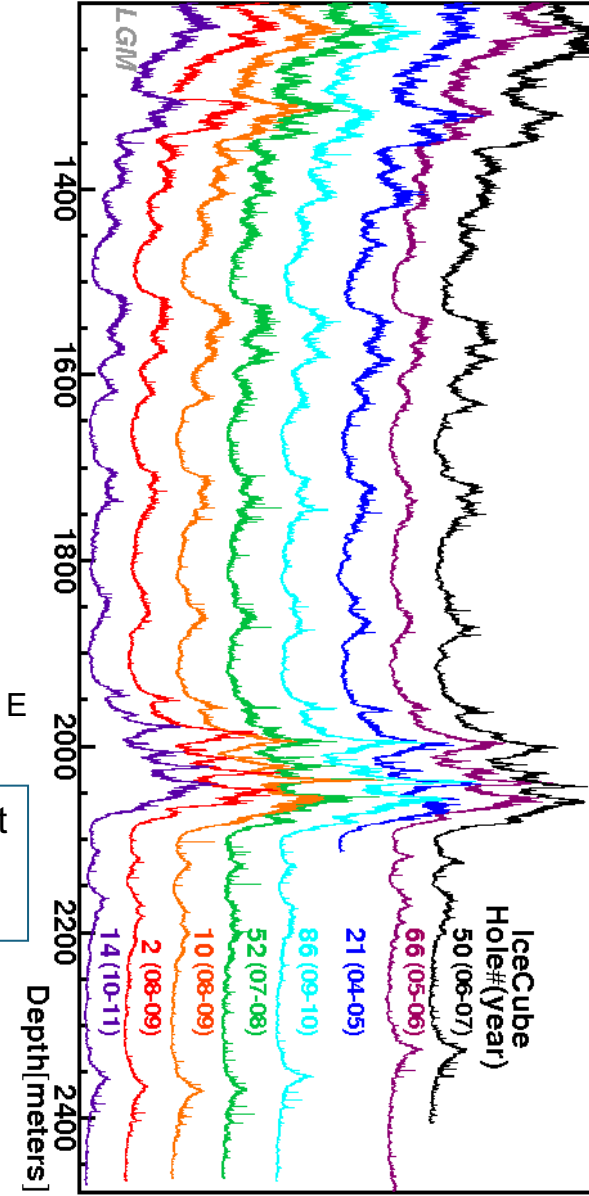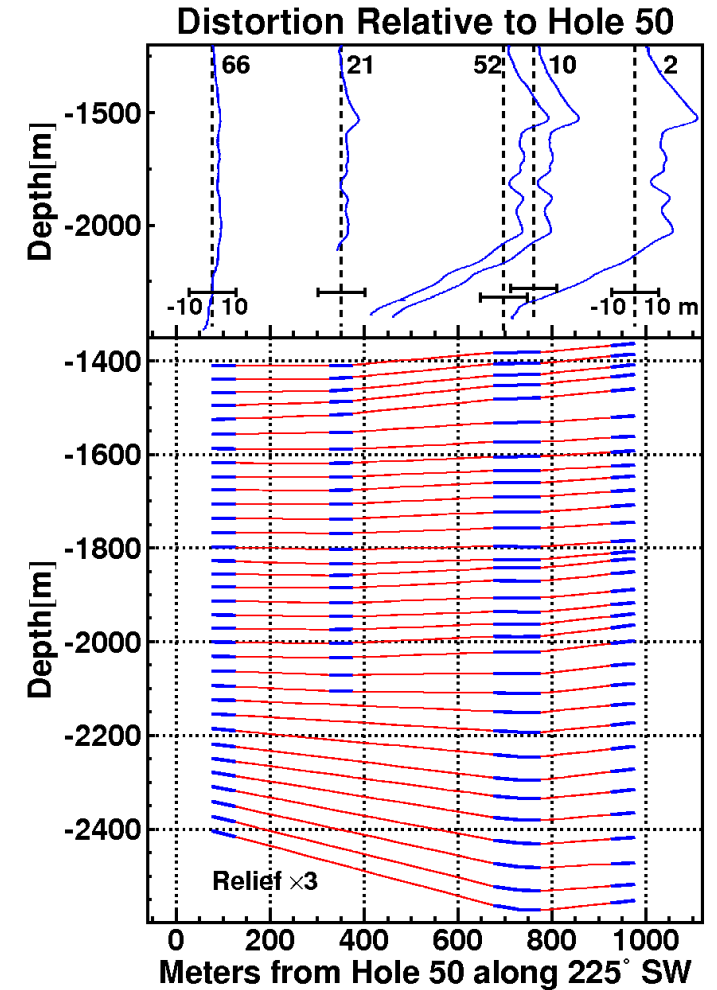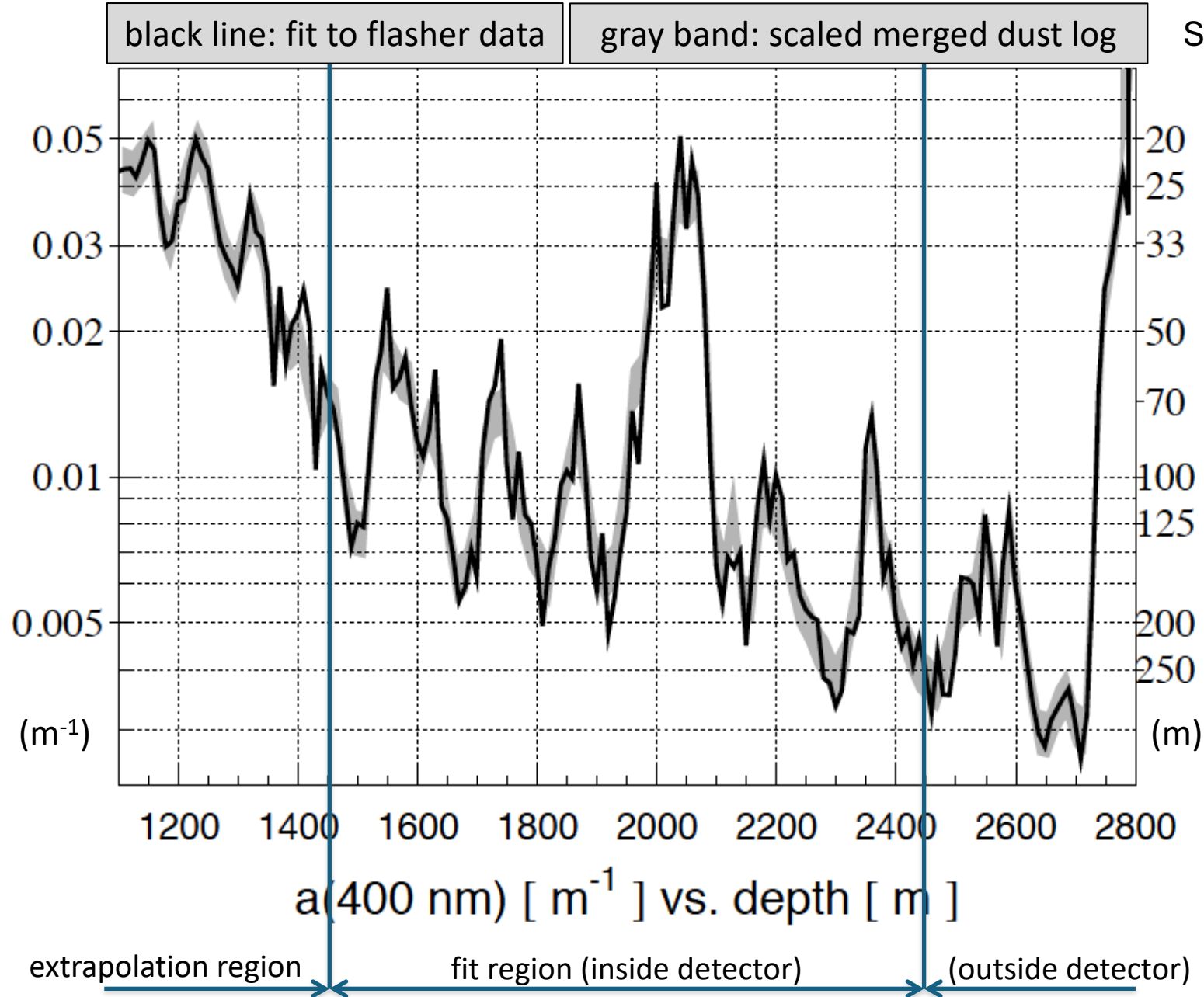
- ● string
- ● IceTop tank
- ● DeepCore string

N
E

ice layer tilt direction: 225° SW

X [m]

Optical Signal

1400
1600
1800
2000
2200
2400

Depth[meters]

IceCube Hole#(year)

14 (10-11)
2 (08-09)
10 (08-09)
52 (07-08)
86 (09-10)
21 (04-05)
66 (05-06)
50 (06-07)

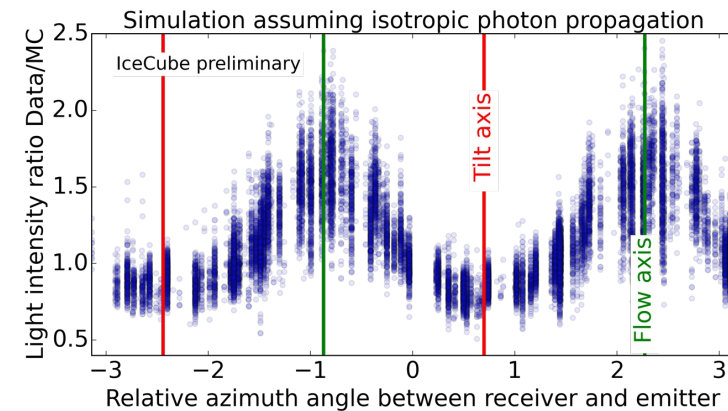The ice layers (i.e. layers ... in depth by as much as 60 m w... ctor

Correlation of fitted optical properties with dust logger data

black line: fit to flasher data

gray band: scaled merged dust log

SPICE 2

a(400 nm) [m^{-1}] vs. depth [m]

(m^{-1})   (m)

extrapolation region   fit region (inside detector)   (outside detector)

Distortion Relative to Hole 50

Depth[m]

66   21   52   10   2

-10 10   -10 10 m

Depth[m]

Relief ×3

Meters from Hole 50 along 225° SW

Glacial ice flow, ice layer tilt, and optical anisotropy

SPICE Lea

Legend:
- # string
- IceTop tank
- # DeepCore string

Ice Layer tilt direction
225° SW

Ice flow direction
41° NW

Less attenuation
41° NW

z-coordinate at string 50 [m]

Relief x3

Meters from Hole 50 along 225° SW

Simulation assuming isotropic photon propagation

IceCube preliminary

Tilt axis

Flow axis

Light intensity ratio Data/MC

Relative azimuth angle between receiver and emitter

South Pole Station

1999

2015

Models of optical ice anisotropy in IceCube

1. Scattering (mainly): direction dependent scattering function (ICRC 2013)
2. Absorption (mainly): direction dependent absorption (studied in 2018)
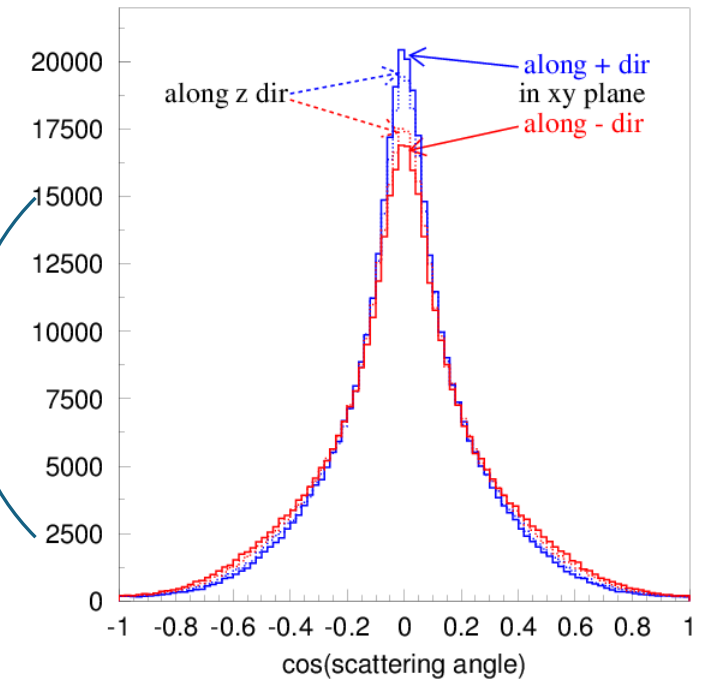
Introduced depth-dependence (2017)

Discrepancies between data and simulation remain

Cannot simultaneously fit total charge and
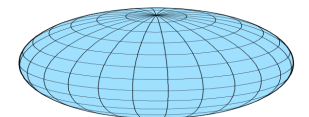arrival time distribution to statistical precision
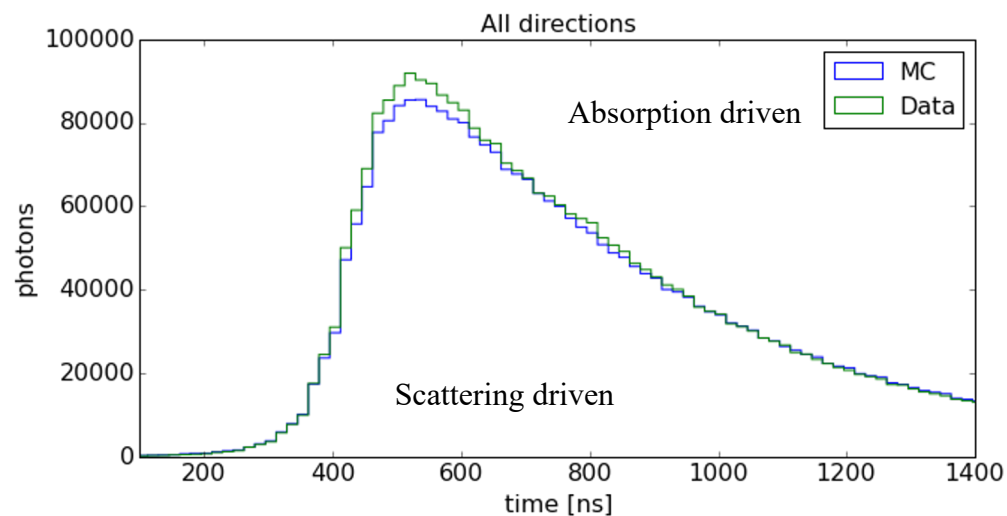
scattering-based

SPICE Lea, 3.2.x
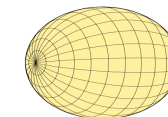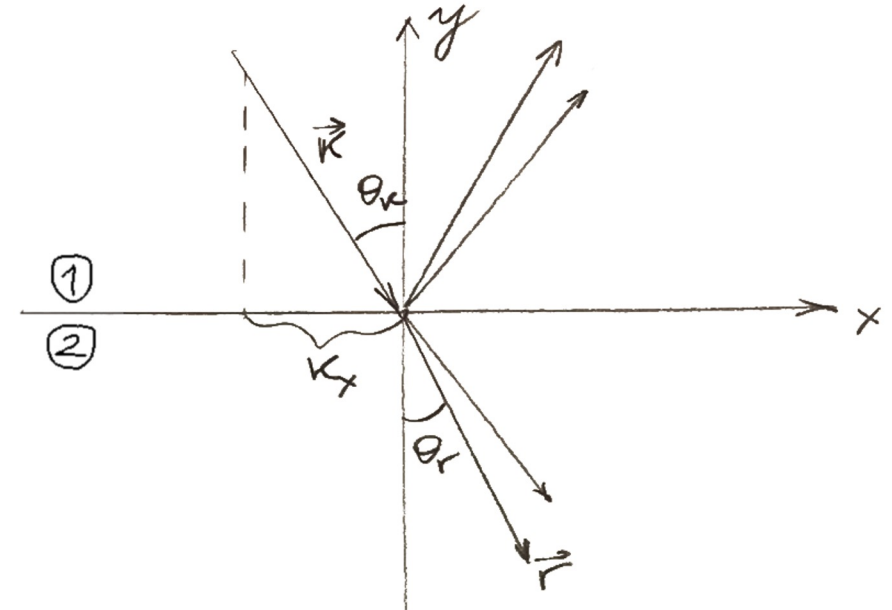
absorption-based

prolate   oblate

SPICE EMRM

Birefringence

wavelength λ (nm)	n_o	n_e
405	1.3185	1.3200
436	1.3161	1.3176
492	1.3128	1.3143
546	1.3105	1.3119
624	1.3091	1.3105
691	1.3067	1.3081

- Ice is a birefringent material with $n_e - n_o = 0.0015$. This tiny difference builds to a macroscopic effect due to 1000s of ice crystal boundaries crossed per meter of traveled distance

- At each grain boundary every ray is split into two reflected and two refracted rays, one ordinary and one extraordinary ray each

- Wave vector component parallel to surface is conserved, norm is proportional to the refractive index

- Poynting vectors are derived from wave vectors and boundary conditions

- Outgoing ray is randomly sampled from Poynting vectors according to Poynting theorem (Poynting vector component through the plane is conserved)

$$\hat{n} \cdot D_2 = \hat{n} \cdot D_1$$
$$\hat{n} \cdot B_2 = \hat{n} \cdot B_1$$
$$\hat{n} \times E_2 = \hat{n} \times E_1$$
$$\hat{n} \times H_2 = \hat{n} \times H_1.$$

Hence we can make the following observations:

1. Normal components of D and B are continuous across a dielectric interface

2. Tangential components of E, H are continuous across a dielectric surface

Scattering patterns birefringent ice

Running MC simulation with realistic crystal size, elongation, and orientation distributions (correlated to flow direction):

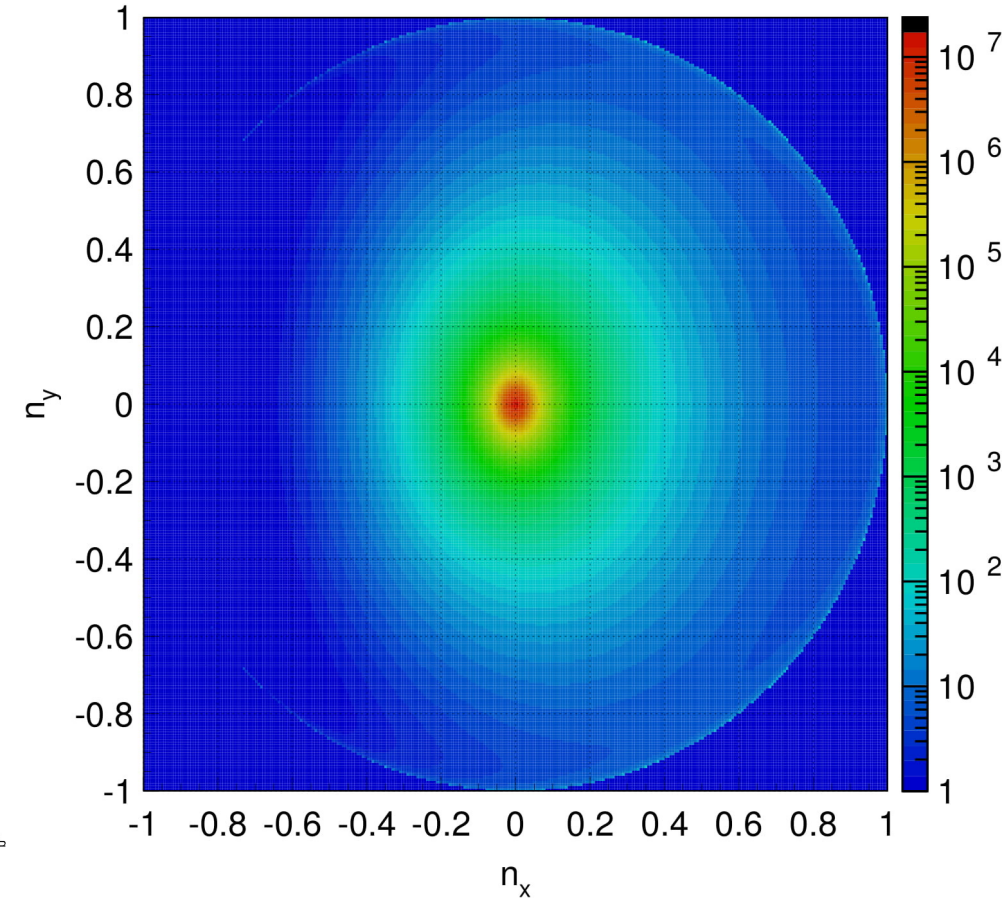Diffusion is largest on flow axis and smallest orthogonal to it

Photons on average get deflected towards the flow axis
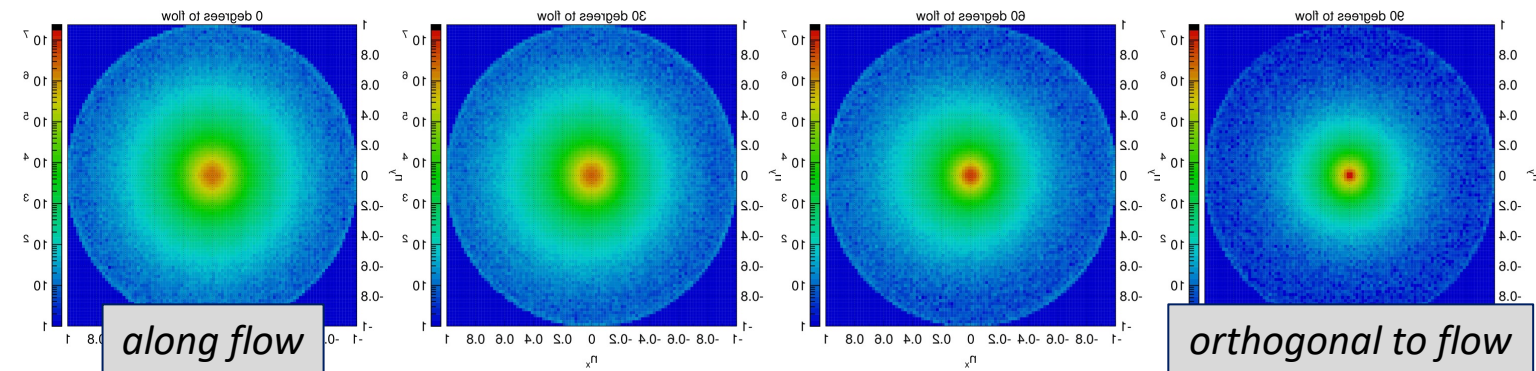
→ photons effectively fly a curve towards the flow axis

along flow

orthogonal to flow
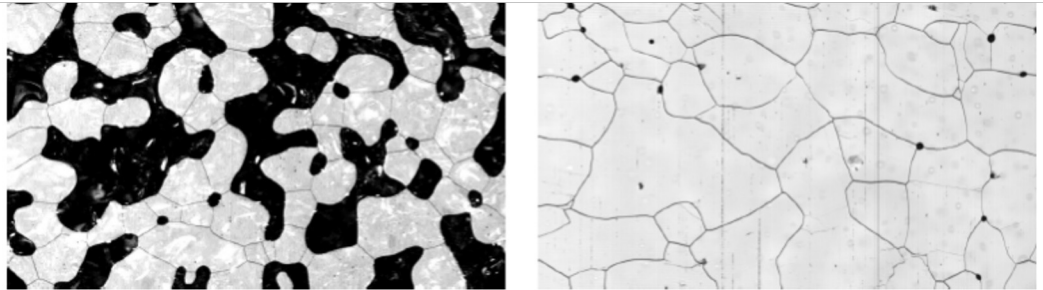
after ~ 1 m of propagation:

45 degrees to flow

towards flow

Scattering patterns birefringent ice
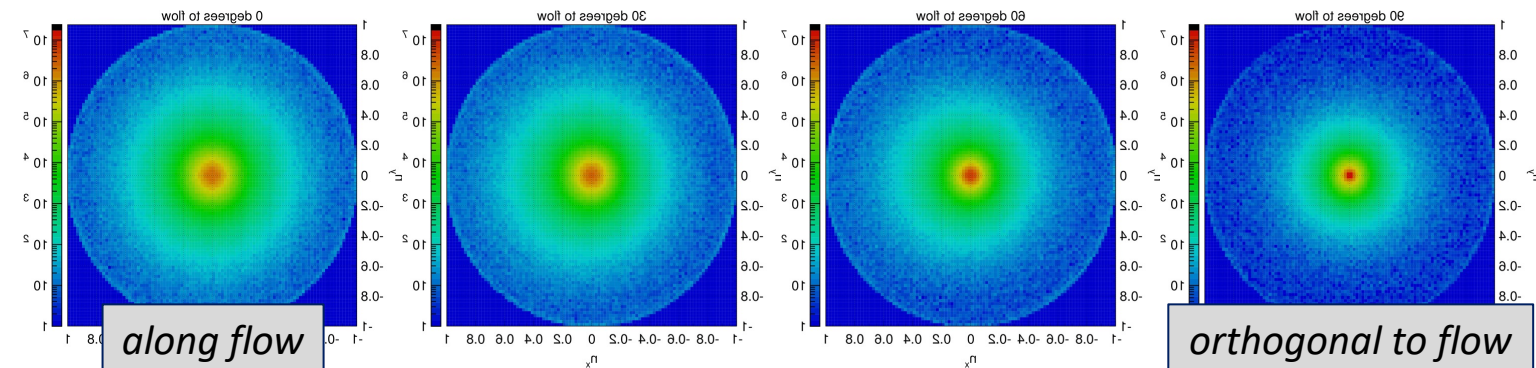
The Cryosphere · Open Access · EGU
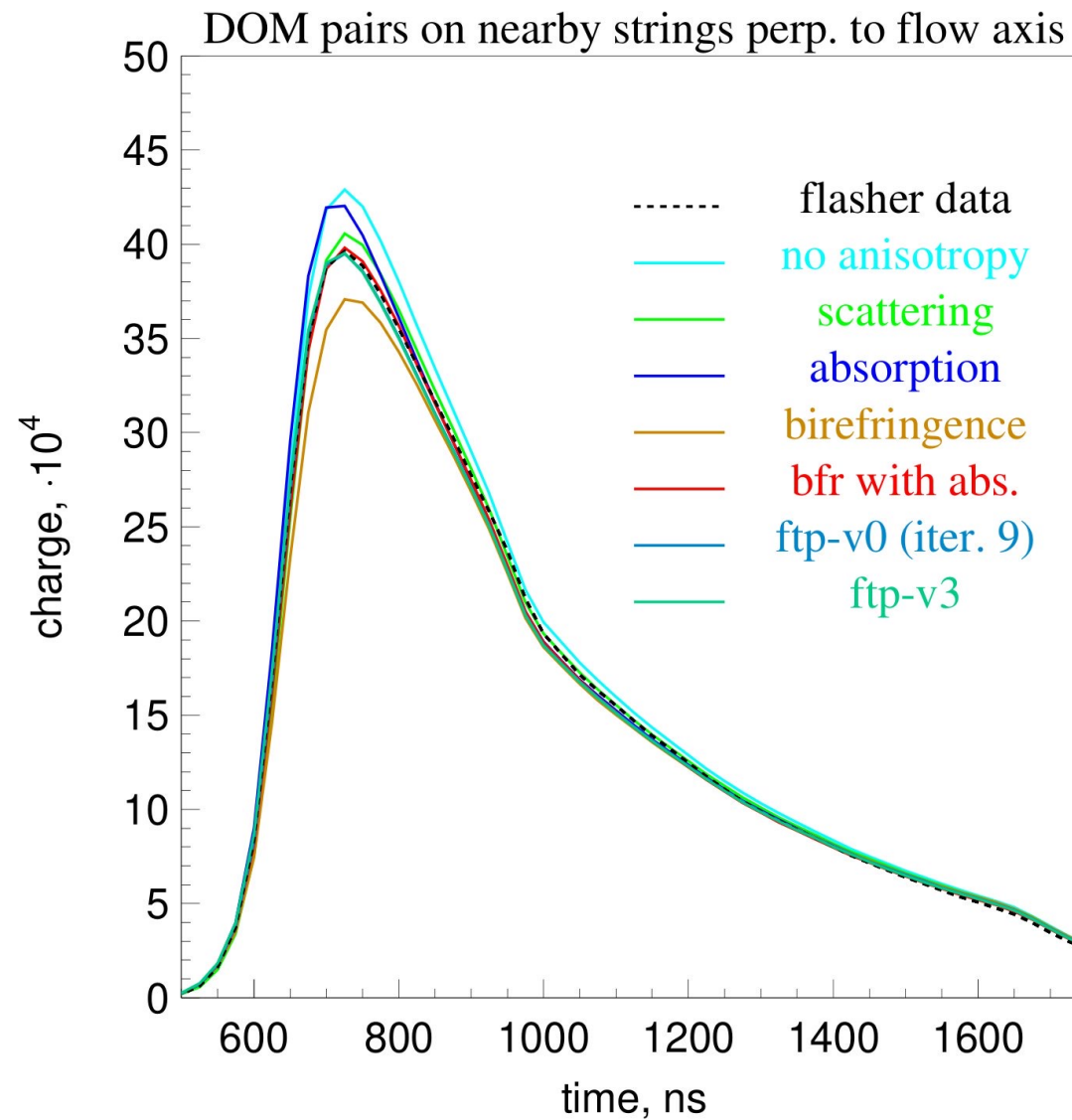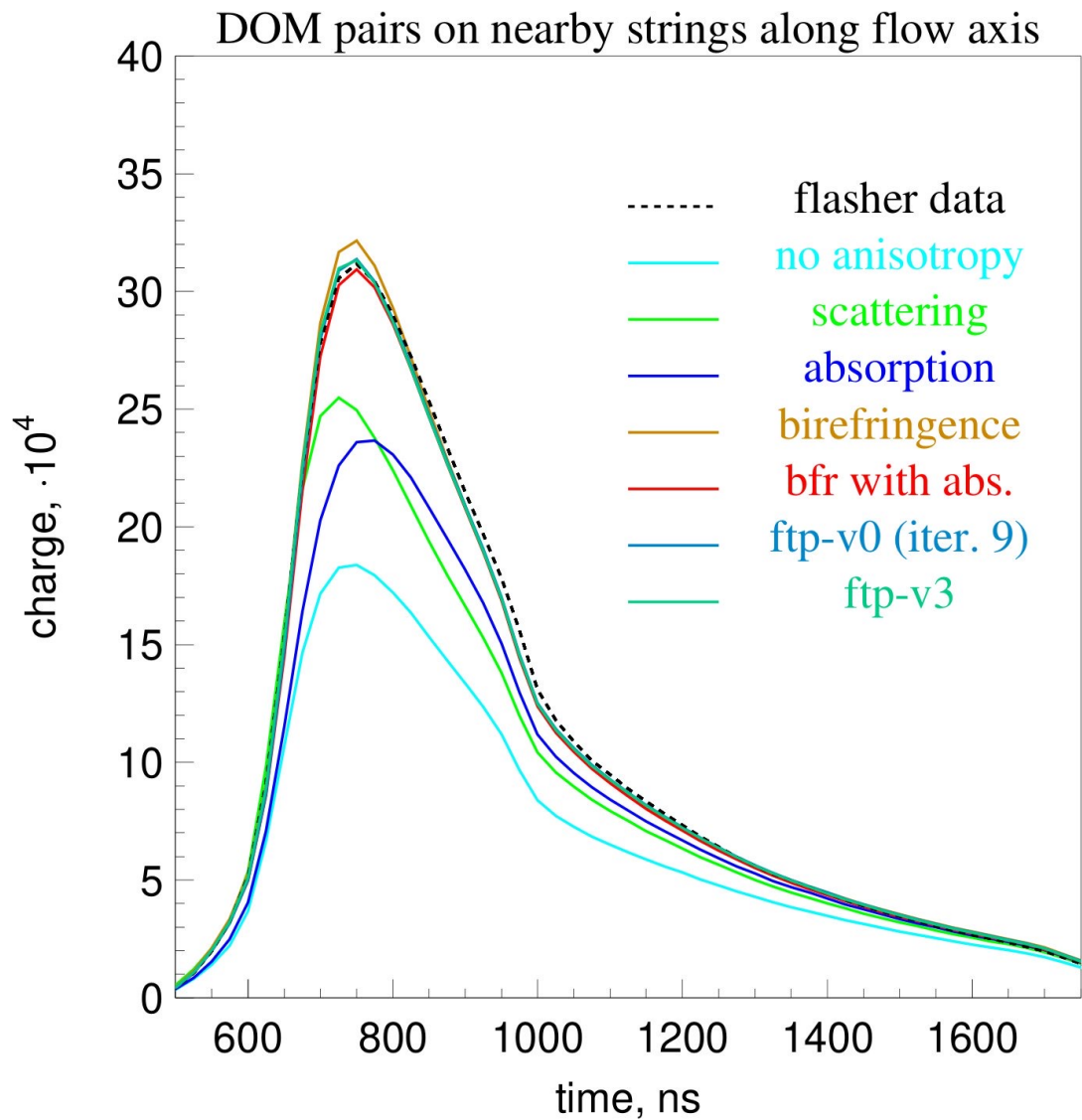
after ~ 1 m of propagation:

2024

45 degrees to flow

In situ estimation of ice crystal properties at the South Pole using
LED calibration data from the IceCube Neutrino Observatory

No birefringence

Birefringence

ice flow

along flow

orthogonal to flow
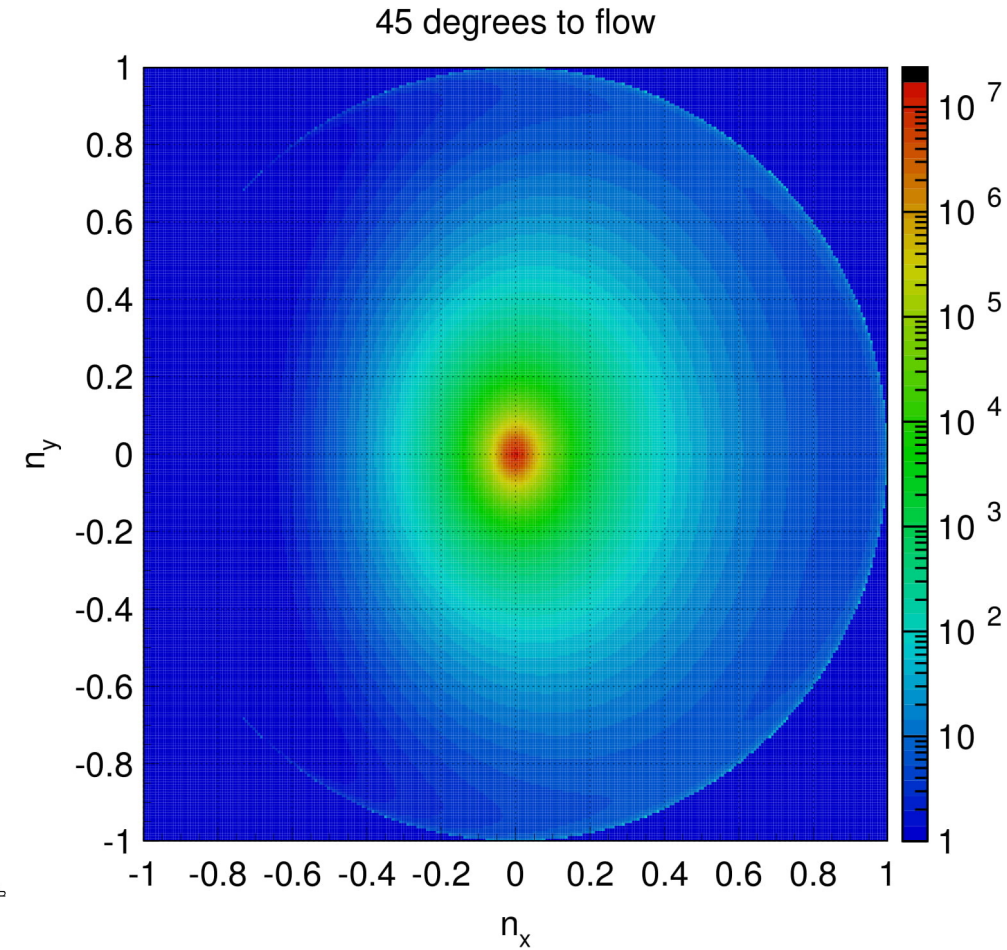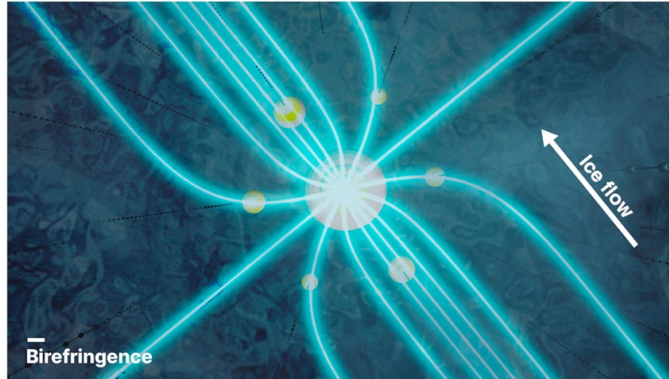
towards flow

Average (at ~125 m) waveform

DOM pairs on nearby strings along flow axis

- flasher data
- no anisotropy
- scattering
- absorption
- birefringence
- bfr with abs.
- ftp-v0 (iter. 9)
- ftp-v3

charge, $\cdot 10^4$ — time, ns

DOM pairs on nearby strings perp. to flow axis

- flasher data
- no anisotropy
- scattering
- absorption
- birefringence
- bfr with abs.
- ftp-v0 (iter. 9)
- ftp-v3

charge, $\cdot 10^4$ — time, ns

Ice layer tilt

Ice at the South Pole is flowing downhill at a rate of ~10 m/year

While the surface of the ice is flat, the bottom of the ice sheet rests atop of bedrock, which has irregular features such as hills and valleys

The ice sheet deforms as it flows through these features, and this results in lower ice layers following the shape of the bedrock; the closer to bedrock, the more the ice layers deviate from the flat that we see on the surface

An ice layer consists of ice deposited at around the same time, so should have the same concentration of impurities across the layer, thus same scattering and absorption properties. The "dirtier" layers will create bands of reflected radar signal
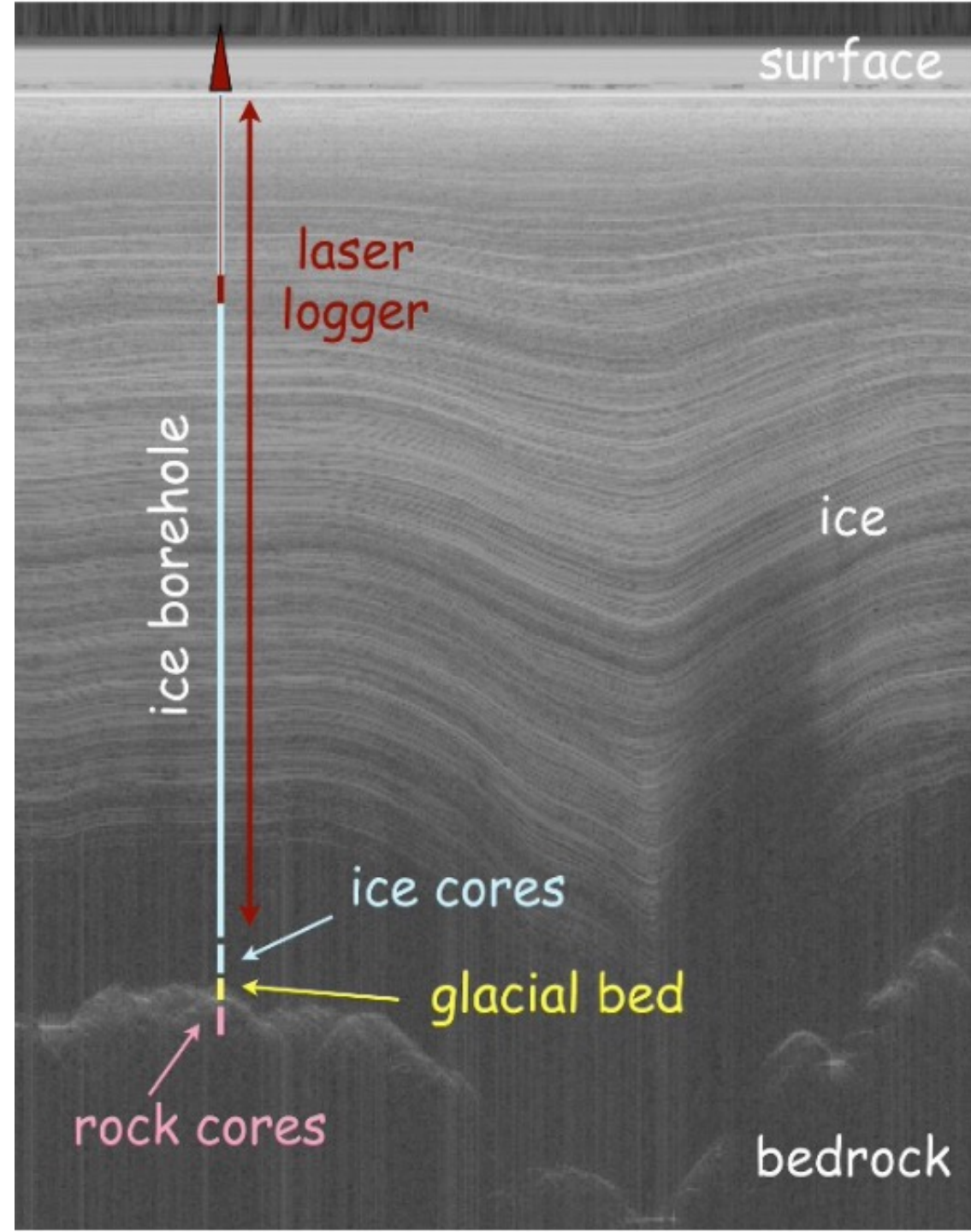
Per-DOM flasher fits

- Tilt correction in the vicinity of each DOM fitted by globally shifting the stratigraphy when optimizing its emitter flasher LLH

- Statistical uncertainty ~1m

- Extremely simple & quick fit, but with large individual biases, & methodological inconsistencies (reference stratigraphy no longer applicable)

Slide by M. Rongen
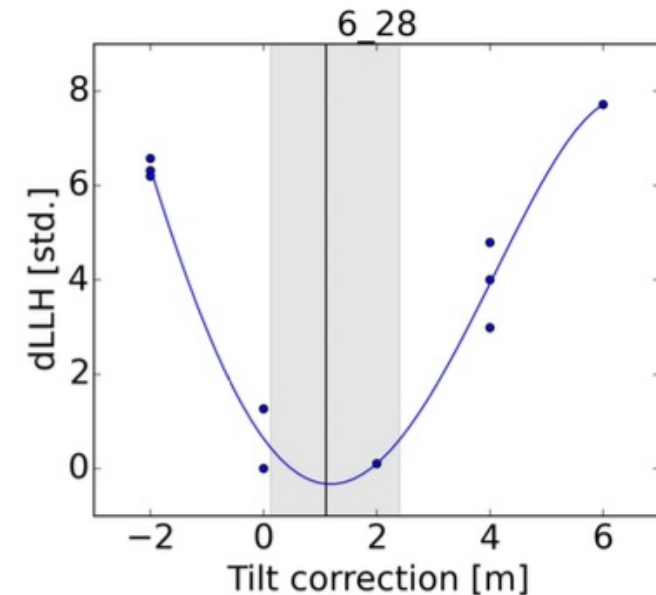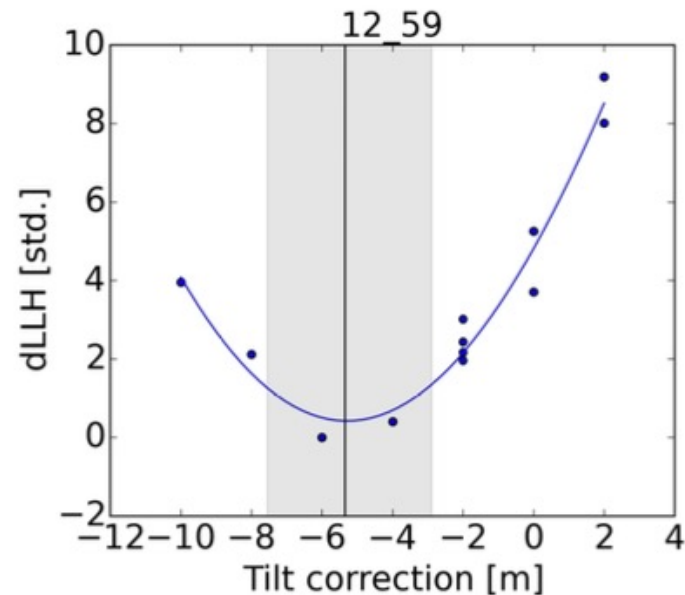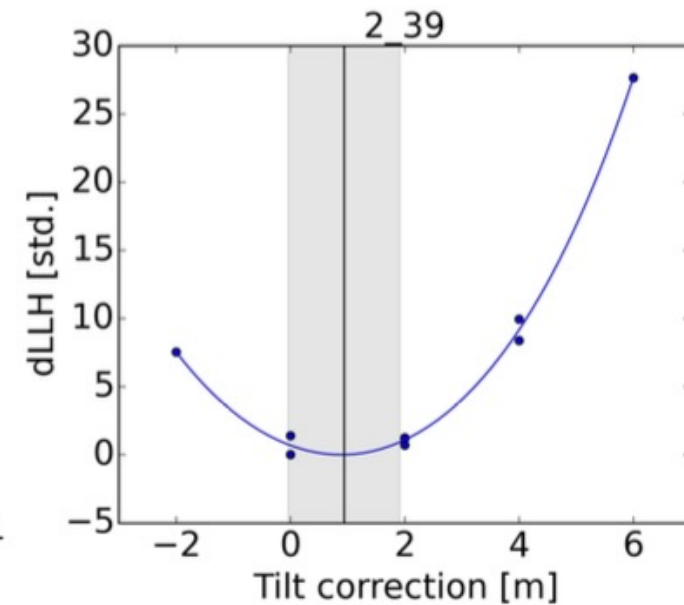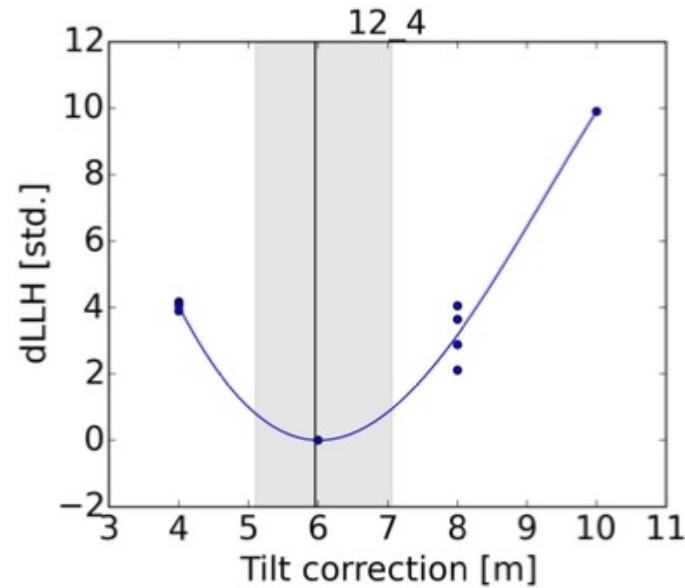
Iterative Positive-Definite Fit (IPDF)

- A second-order Taylor expansion is used to fit the shape of the llh in the vicinity of best previous solution
  i.e., a paraboloid fit
  llh values are computed for nominal+100-1000 random perturbations set of simulations at each iteration

- Some regularizations are necessary
  - α: stiffness of paraboloid fit (curvature)
  - β: correlation terms (to smooth unnecessary up/down oscillations in solution)
  - γ: norm of solution (to keep it in bounds of the perturbation set)

- Search for solution (minimization)
  A direct matrix regularized inversion was tried first but often resulted in non-positive-def solutions
  Newton's gradient descent method was adopted with explicit positive-definite curvature matrix

N_{par} dimensional paraboloid describing LLH(perturbation)   **Regularization terms with tunable regularization strengths α, β, γ**
α: Stiffness of paraboloid; β: norm of solution; γ: smoothing correlation terms
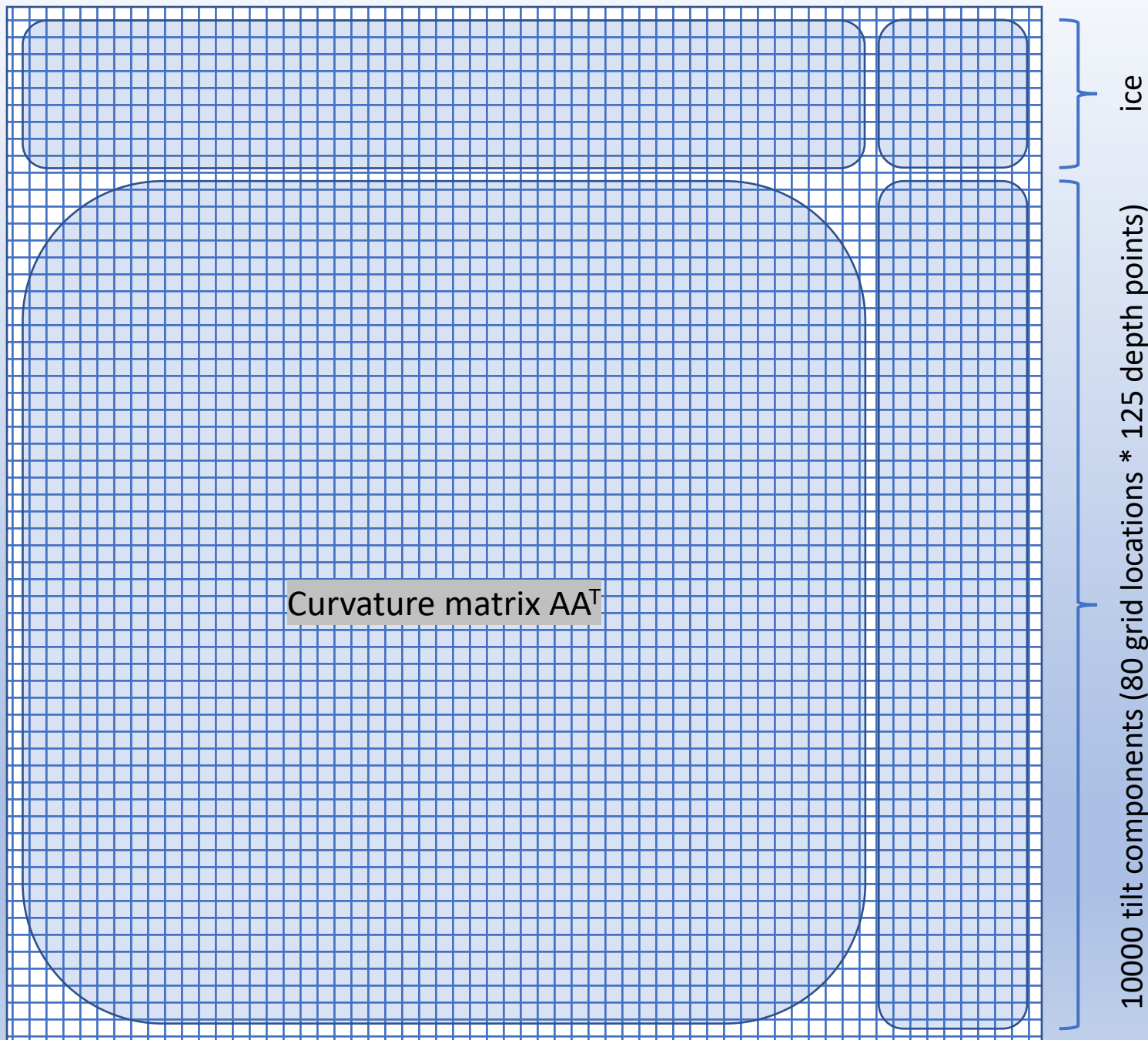
$$L = \sum_{i=1}^{N_{sim}} (Q^i + C_0 - h_i)^2 + \alpha \cdot \left(\sum_{k,n=1}^{N_{par}} a_{kn}^2 \right)^2 + \beta \cdot \left(\sum_{k=1}^{N_{par}} (D_{kn}(b_n + T_n))^2 \right)^2 + \gamma \cdot \left(\sum_{n=1}^{N_{par}} b_n^4 \right) \text{ where } Q^i = \sum_{k=1}^{N_{par}} (a_{kn}(\Delta_n^i - b_n))^2$$

Value of L at the minimum

regularization term (2nd derivative, etc.)

$a_{kn}a_{km}$ is curvature matrix

deviations solution vector (main result)

Paraboloid Fit

Curvature matrix AA^T

ice

10000 tilt components (80 grid locations * 125 depth points)

2nd order Taylor expansion around the (presumed) minimum is a paraboloid with the curvature expressed as AA^T (to enforce positive-definite quality)

Solution vector consists of:
- 10000 tilt corrections (on a grid of 80 xy locations, times 125 depth points)
- 513 ice parameters at grid point 36 (scattering, absorption, crystal density at 171 depth points)

The paraboloid is flat as possible, by regularization reducing the norm of AA^T

Additional regularizations to smooth the jaggedness in tilt solutions

Ice tilt fitted with IceCube calibration data
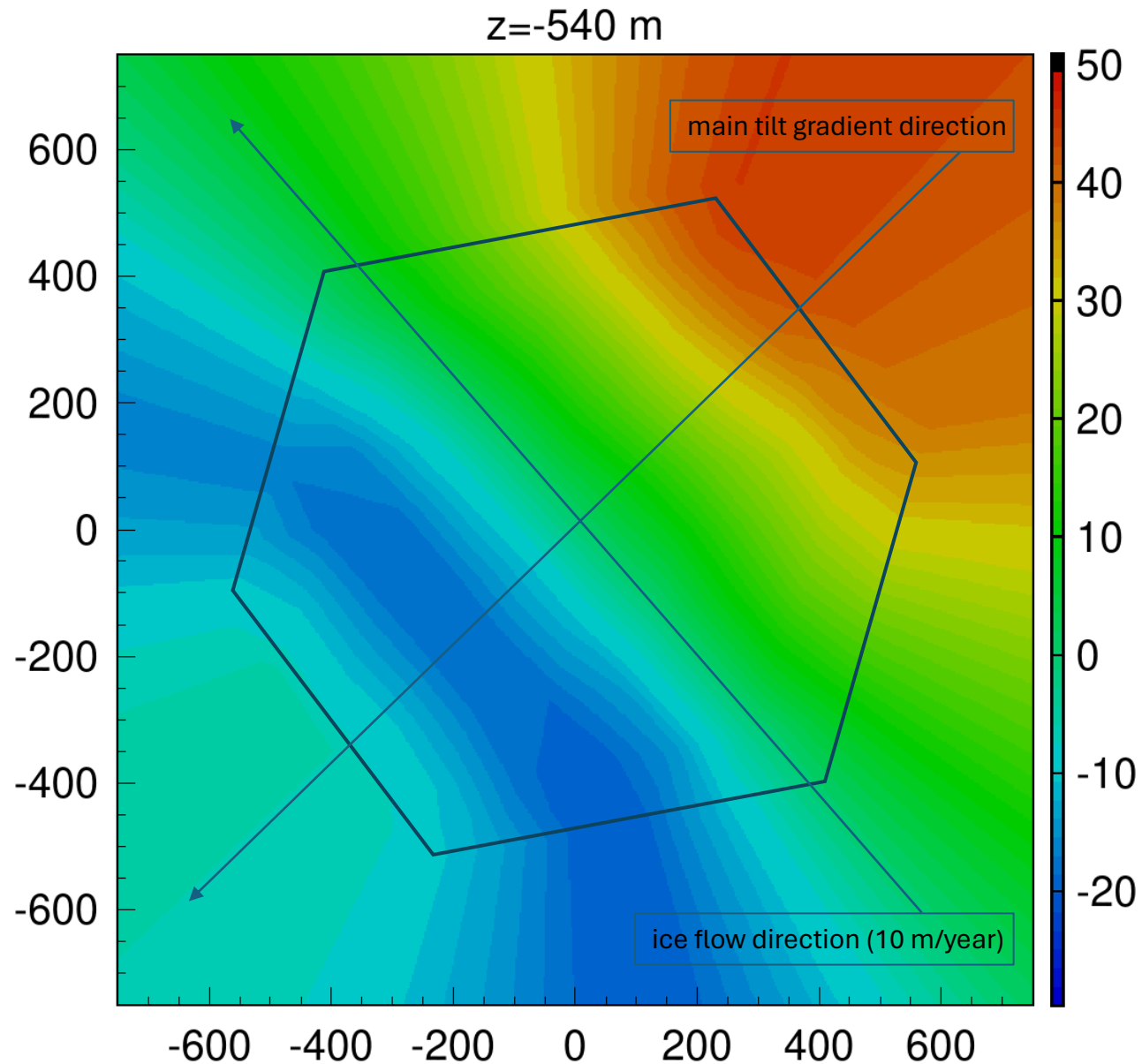
z=-540 m

main tilt gradient direction

ice flow direction (10 m/year)

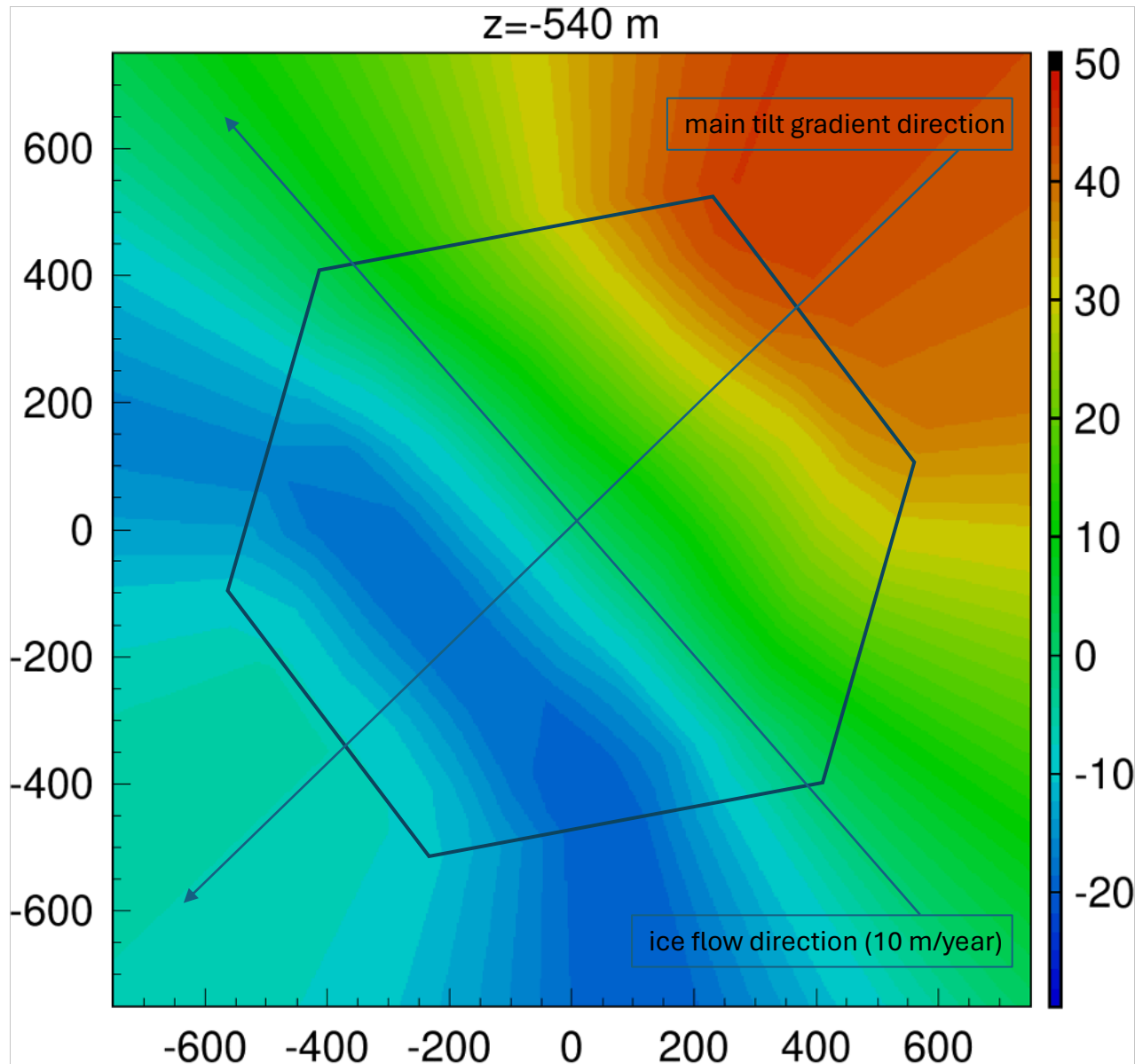Regions outside of detector hexagon outline are extrapolations

Regions above and below +-500 m are outside the detector volume, and as such, are also extrapolations

Shown are ice layer shifts wrt. a point near string 36 (close to detector center)

The 1d gradient tilt (only accounting for tilt in the direction NE-SW) appears to be a better approximation at the bottom of the detector

Across the entire fitted depth range there appears to be an additional component that changes the depth of ice layers along the ice flow (layers getting shallower downstream)

# Ice tilt fitted with IceCube calibration data

z=-540 m

main tilt gradient direction

ice flow direction (10 m/year)

Regions outside of detector hexagon outline are extrapolations

Regions above and below +-500 m are outside the detector volume, and as such, are also extrapolations

Shown are ice layer shifts wrt. a point near string 36 (close to detector center)

The 1d gradient tilt (only accounting for tilt in the direction NE-SW) appears to be a better approximation at the bottom of the detector

Across the entire fitted depth range there appears to be an additional component that changes the depth of ice layers along the ice flow (layers getting shallower downstream)

Hole ice cameras

AMANDA:
   Swedish camera deployed in 1998 in AMANDA hole 13
IceCube:
   Bubble camera deployed in the 2006/7 season with string 57
   Swedish camera deployed in the 2010/11 season with the last string (80)
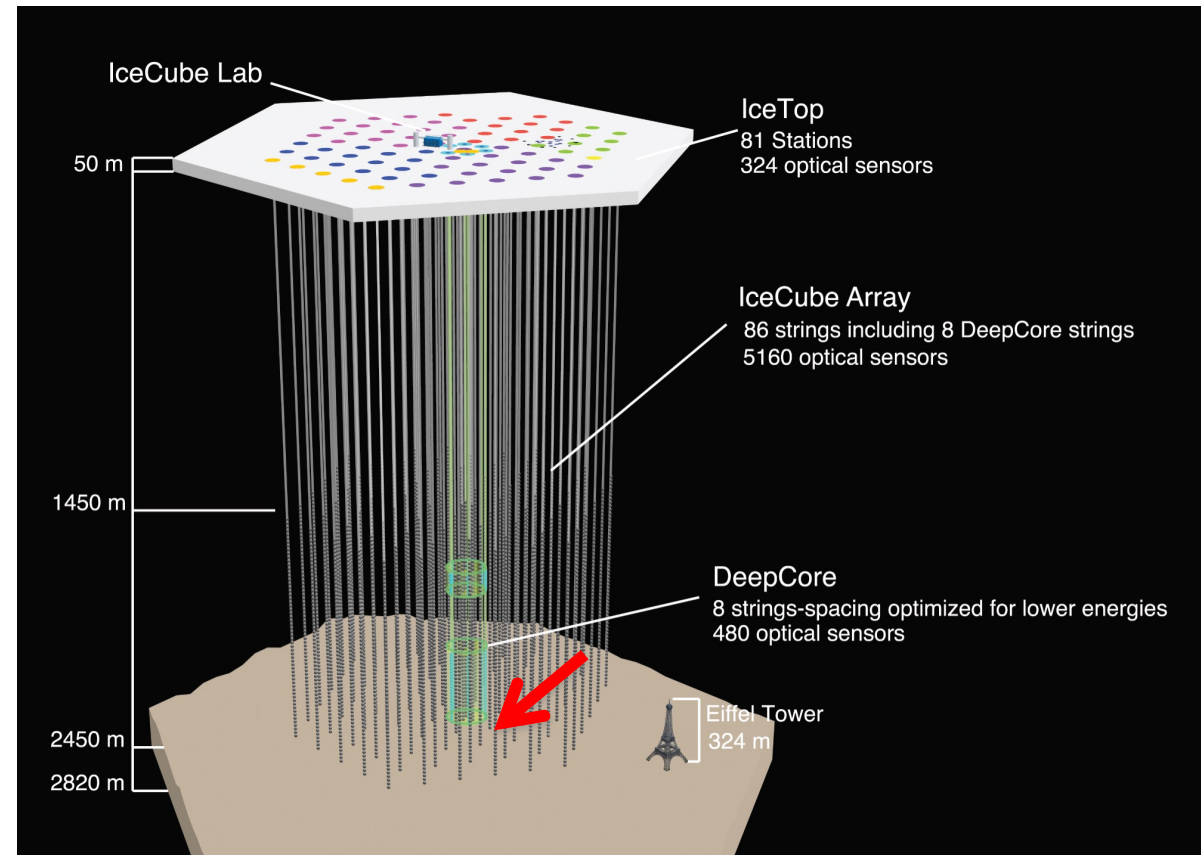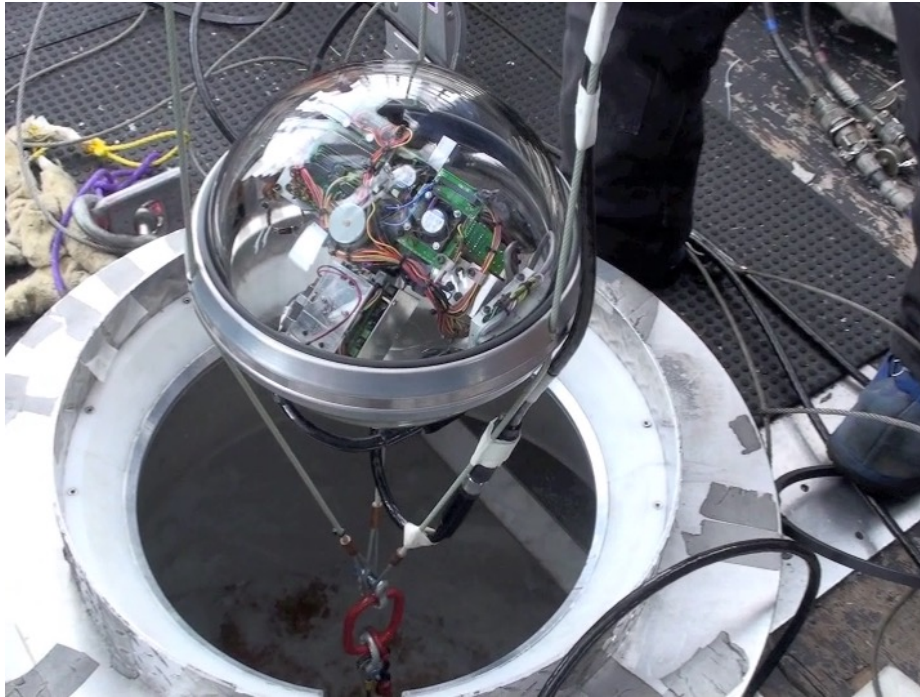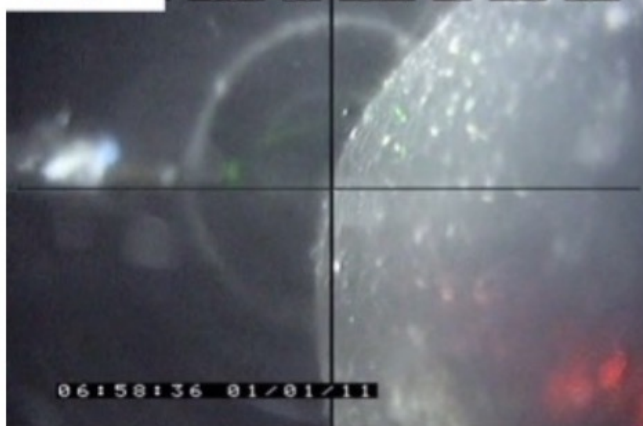
29/12/10 (d/m/yr)
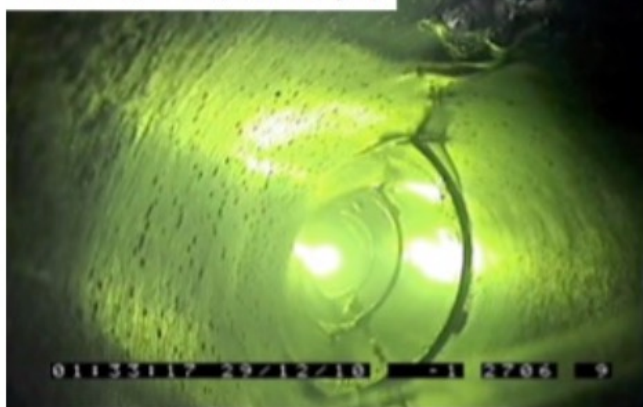
30/12/10

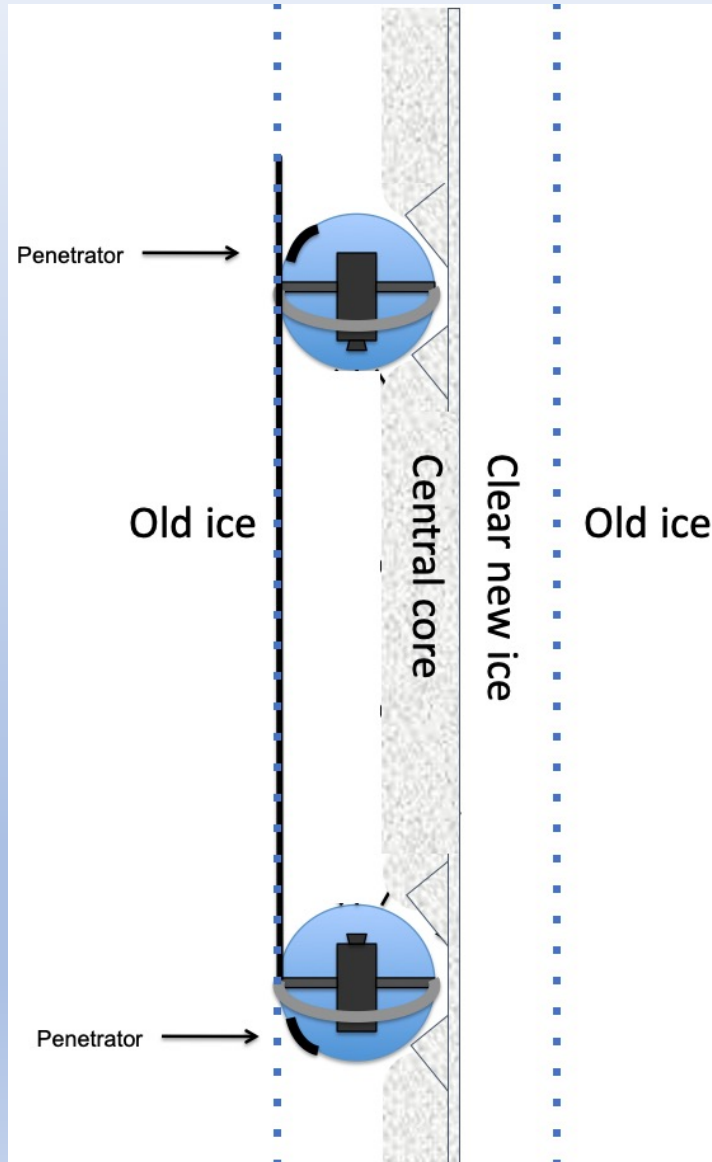31/12/10

1/1/11

2/1/11

10/2/11

4/3/11

8/4/11

9/11/11

IceCube bootcamp 2023 - Calibration - Williams

Refrozen hole ice is more complex than thought before the Swedish Camera took its pictures
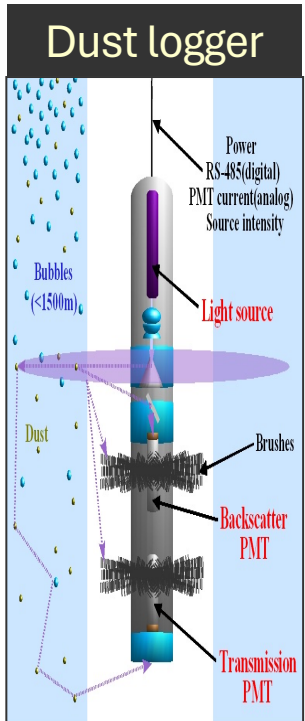

We find:
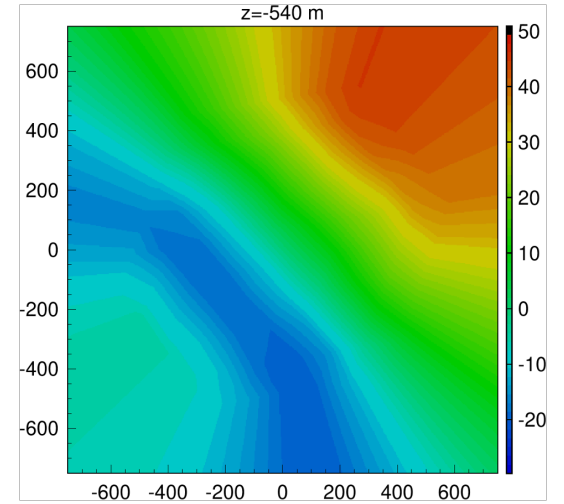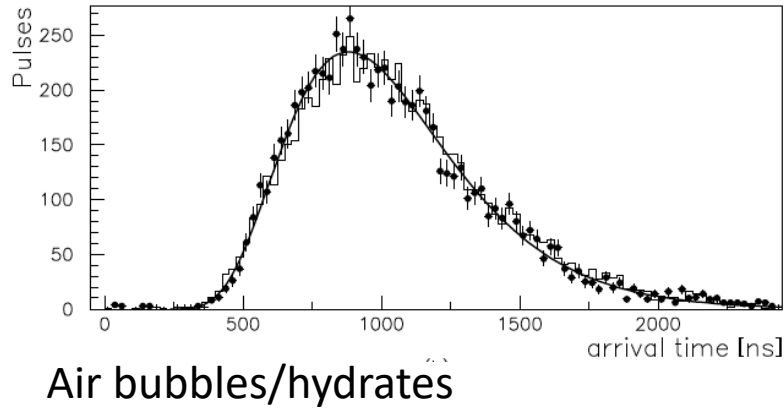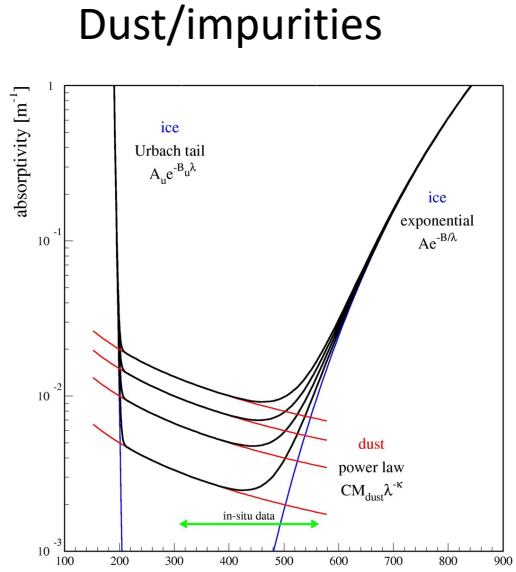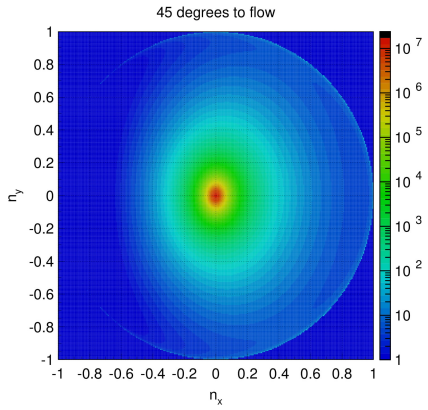
DOM touches the hole wall, is 2/3 of the hole diameter

Most of the HI is transparent, except for the milky central column centered in the hole and 1/3 of hole diameter (referred to as HI in the following, starting with the next line)

HI diameter is ½ of DOM diameter

Things we learned
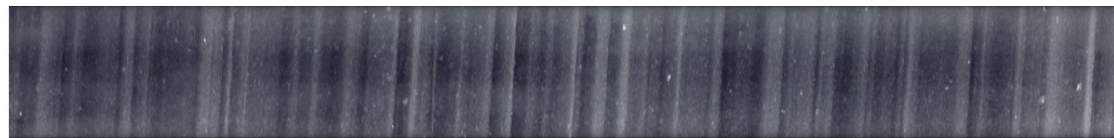

45 degrees to flow

Dust/impurities

Air bubbles/hydrates

z=-540 m

Dust logger

Ice anisotropy

Ice Layer tilt direction
225° SW

Ice flow direction
41° NW

anisotropy axis
41° NW

Hole ice

Distortion Relative to Hole 50
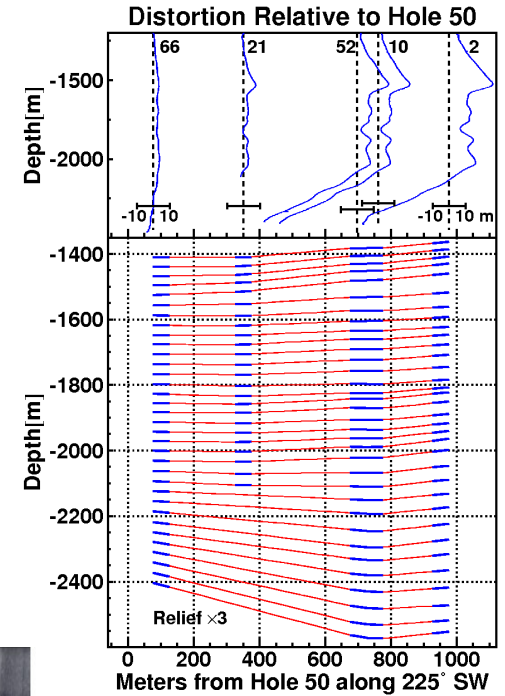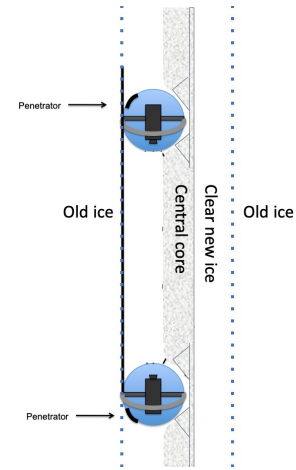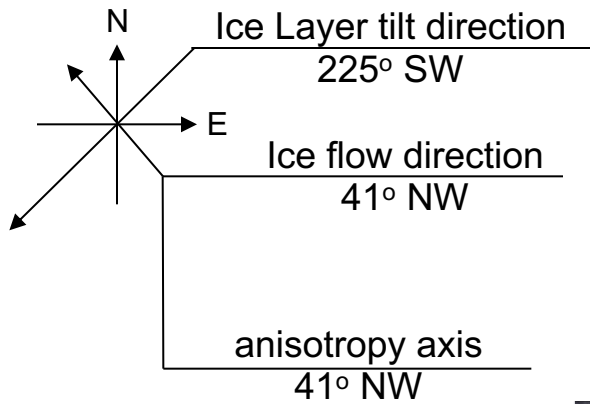
Ice tilt

Covariance matrix calculation

Direct inversion of matrix AA^T with
    tilt free to float (invert, then show ice-only components)
    tilt frozen at best solution (freeze tilt components, then invert)
        this is done with the SVD decomposition of matrix A, so SV can be calculated and shown

Now have ice model sampler, which (basically) calculates solution to Ax=$\alpha\xi$, α: scaling, ξ: normal random
    this reduces paraboloid (Ax)^2 to $\Sigma\alpha^2\xi^2$.

Sampler needs to have space of ice models constrained to regularized tilt models
    this is done by including regularization matrices into AA^T.

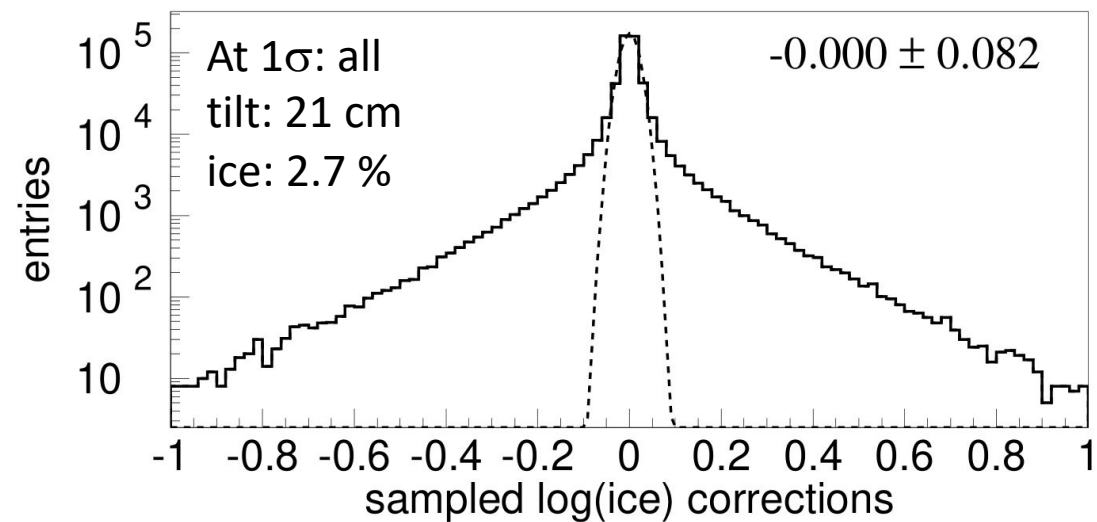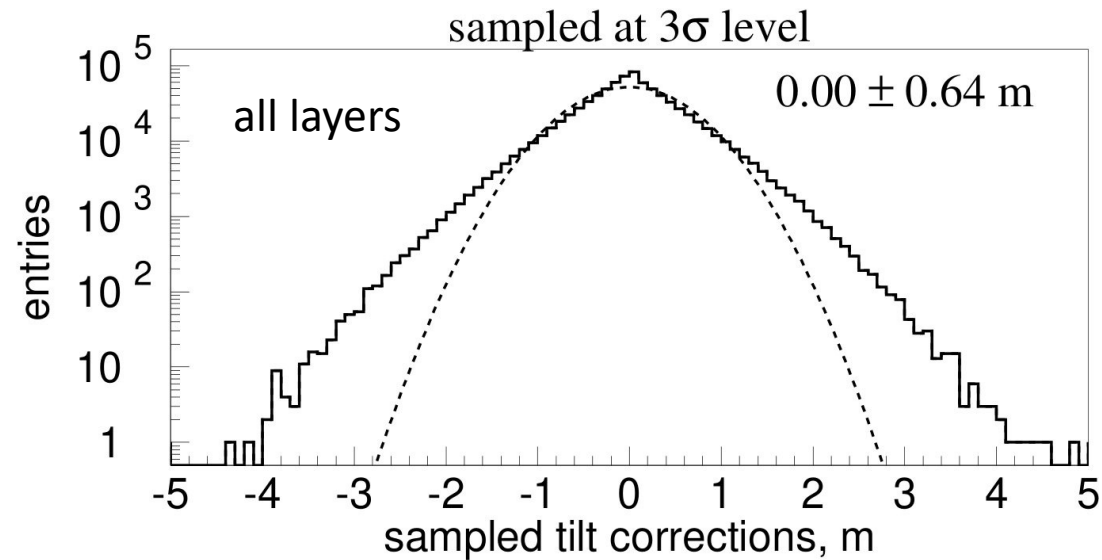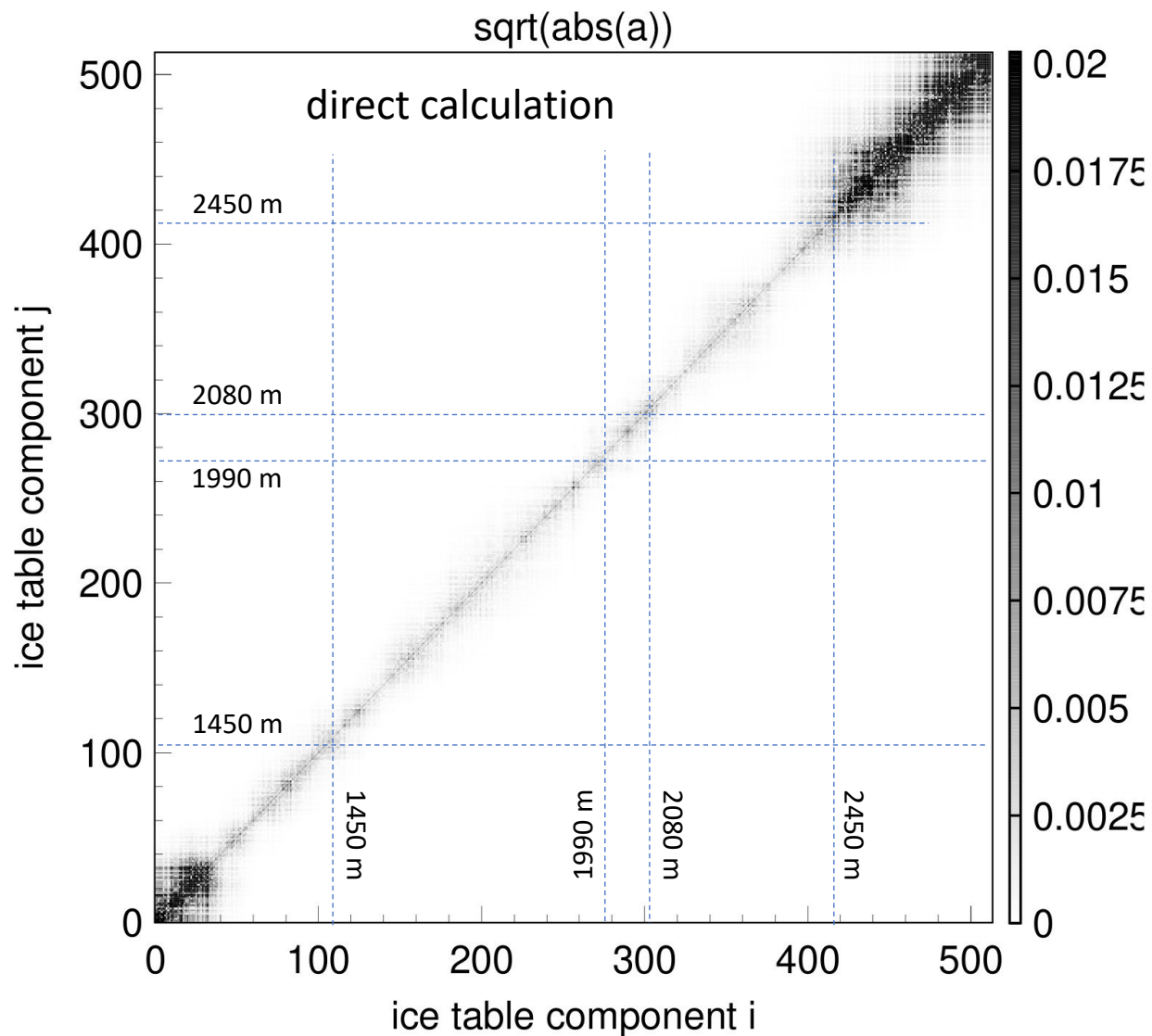Compare direct inversion with covariance calculation from ice samples

N_{par} dimensional paraboloid describing LLH(perturbation)   **Regularization terms with tunable regularization strengths α, β, γ**
α: Stiffness of paraboloid; β: norm of solution; γ: smoothing correlation terms

$$L = \sum_{i=1}^{N_{sim}}(Q^i + C_0 - h_i)^2 + \alpha \cdot \left(\sum_{k,n=1}^{N_{par}} a_{kn}^2\right)^2 + \beta \cdot \left(\sum_{k=1}^{N_{par}}(D_{kn}(b_n + T_n))^2\right)^2 + \gamma \cdot \left(\sum_{n=1}^{N_{par}} b_n^4\right) \quad \text{where} \quad Q^i = \sum_{k=1}^{N_{par}}(a_{kn}(\Delta_n^i - b_n))^2$$
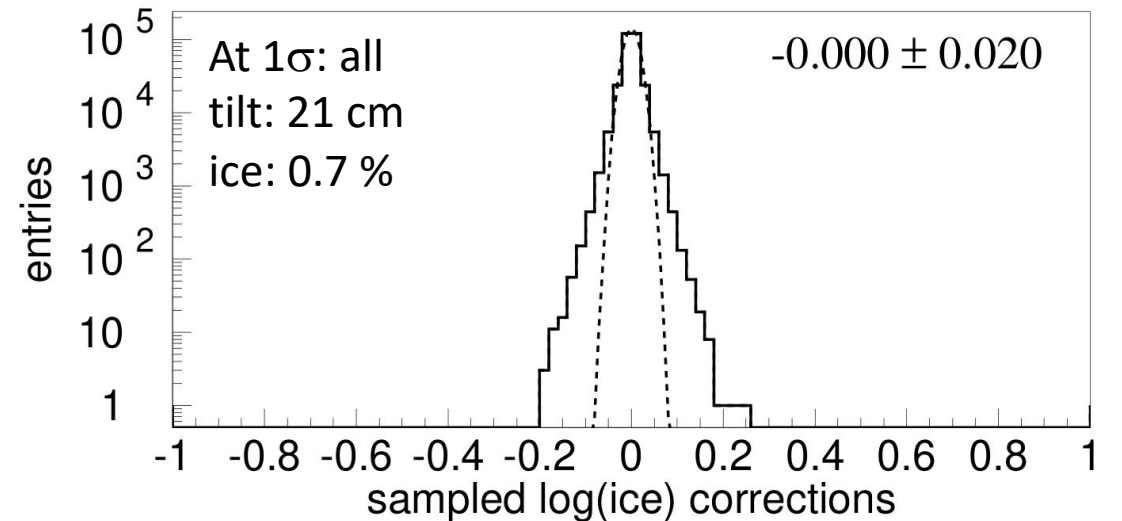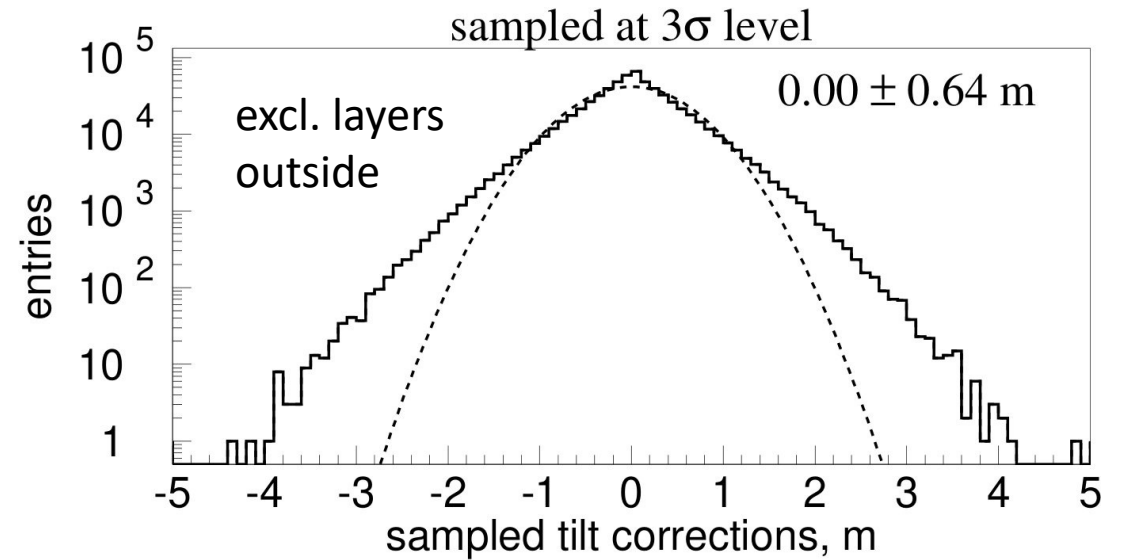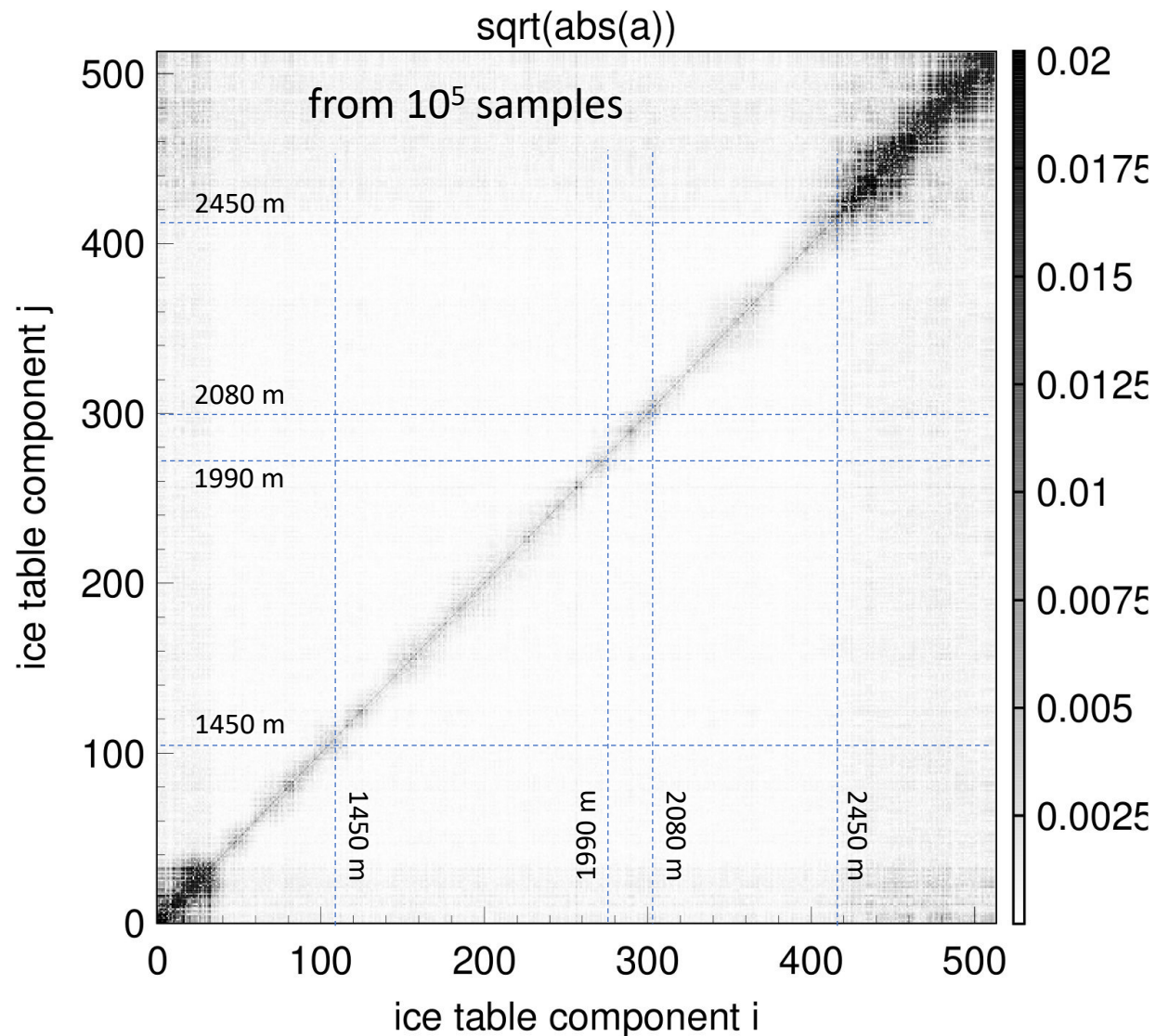
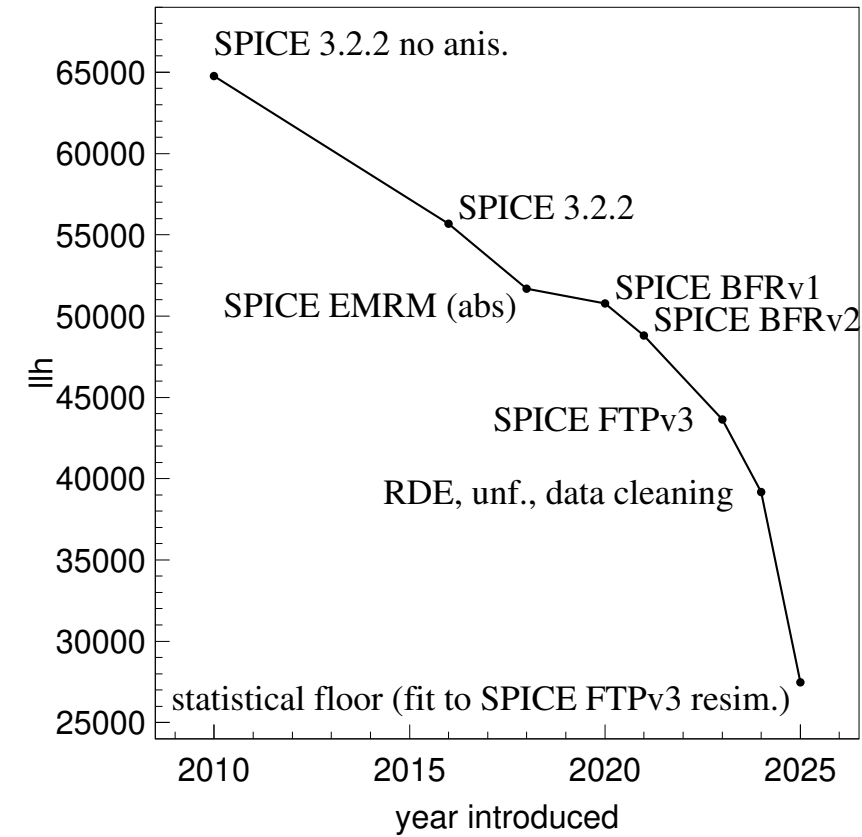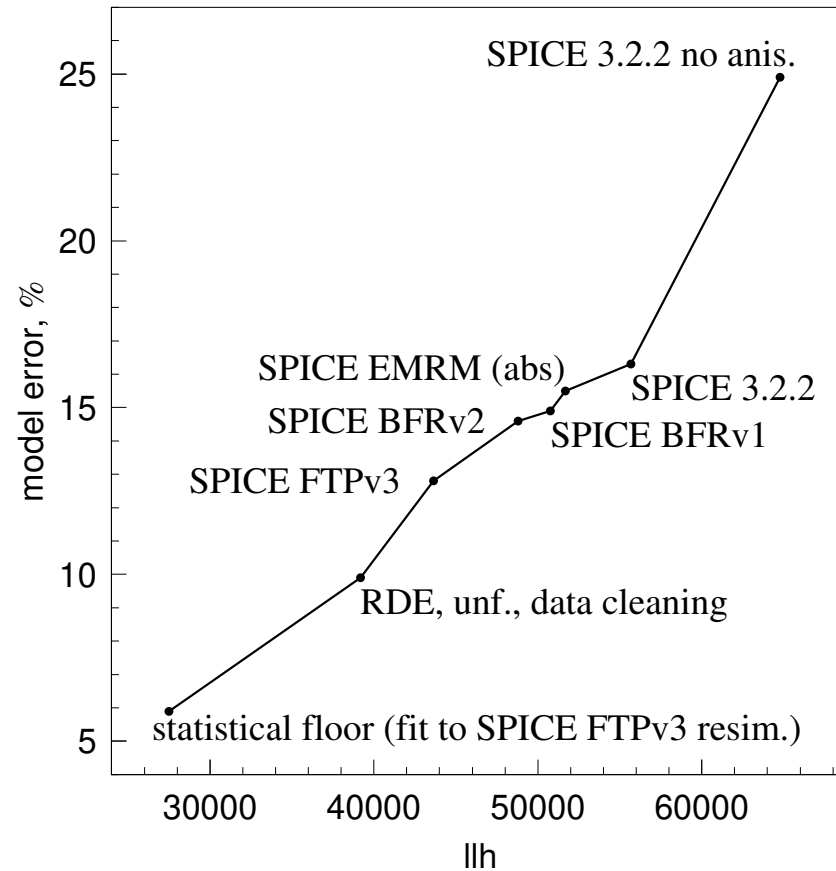# Estimated uncertainties/covariance matrix

Ice+tilt sampling

Estimated uncertainties/covariance matrix

Ice+tilt sampling

sqrt(abs(a))

from 10^5 samples

ice table component j

2450 m

2080 m

1990 m

1450 m

ice table component i

sampled at 3σ level

0.00 ± 0.64 m

excl. layers outside

entries

sampled tilt corrections, m

At 1σ: all
tilt: 21 cm
ice: 0.7 %

-0.000 ± 0.020

entries

sampled log(ice) corrections

Recent ice model progression
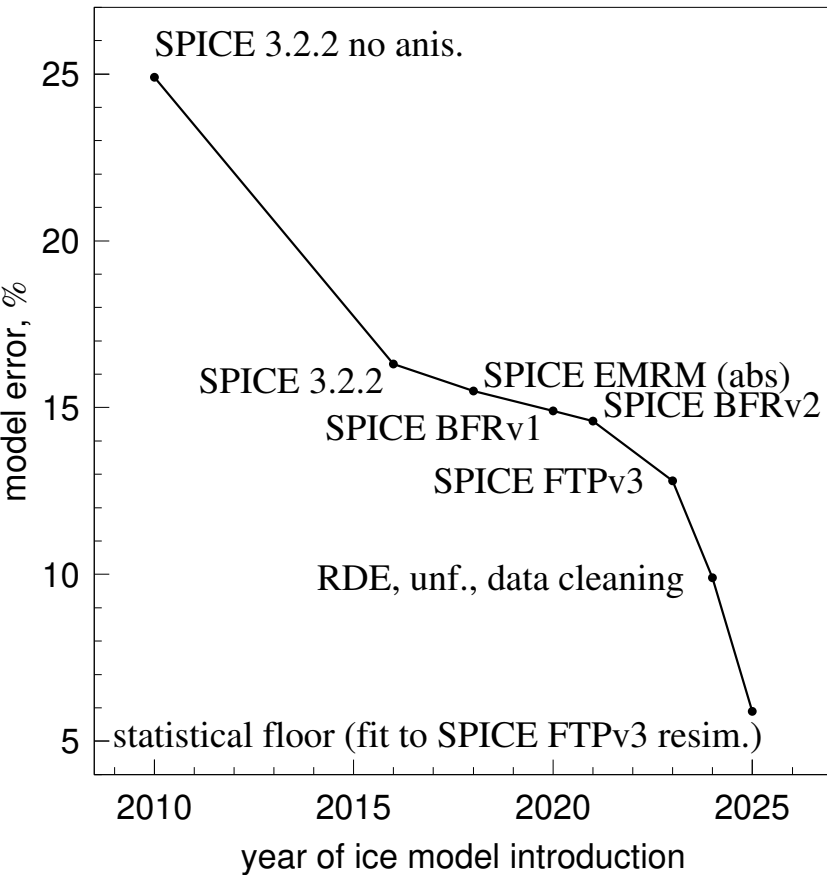
Ice model progression (zoomed out)

summary

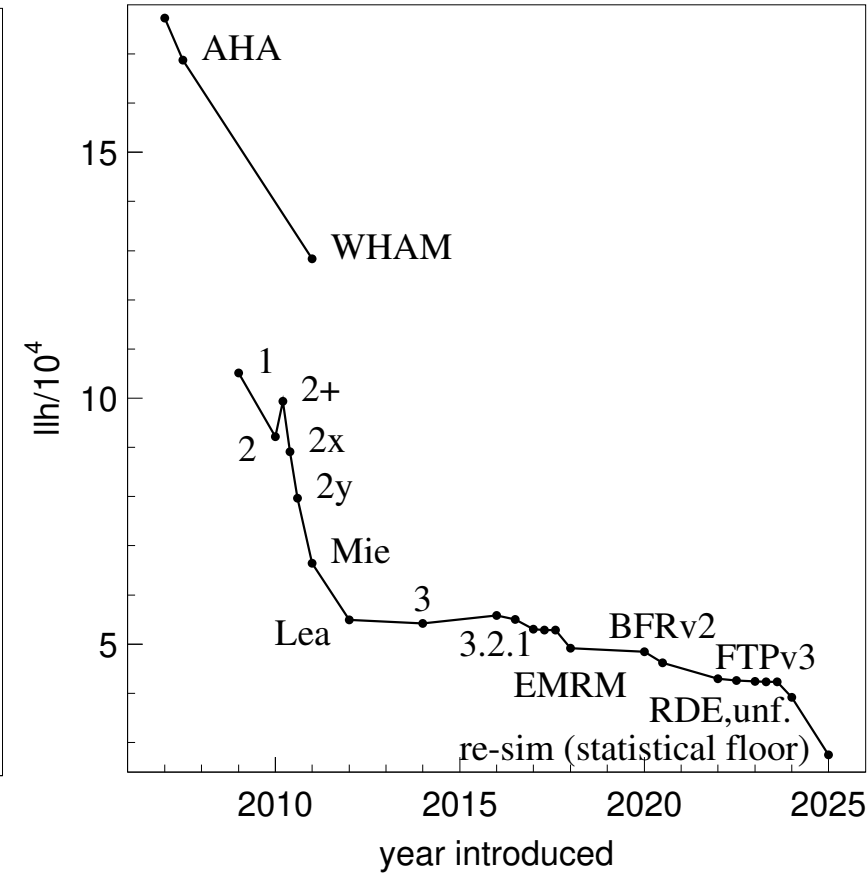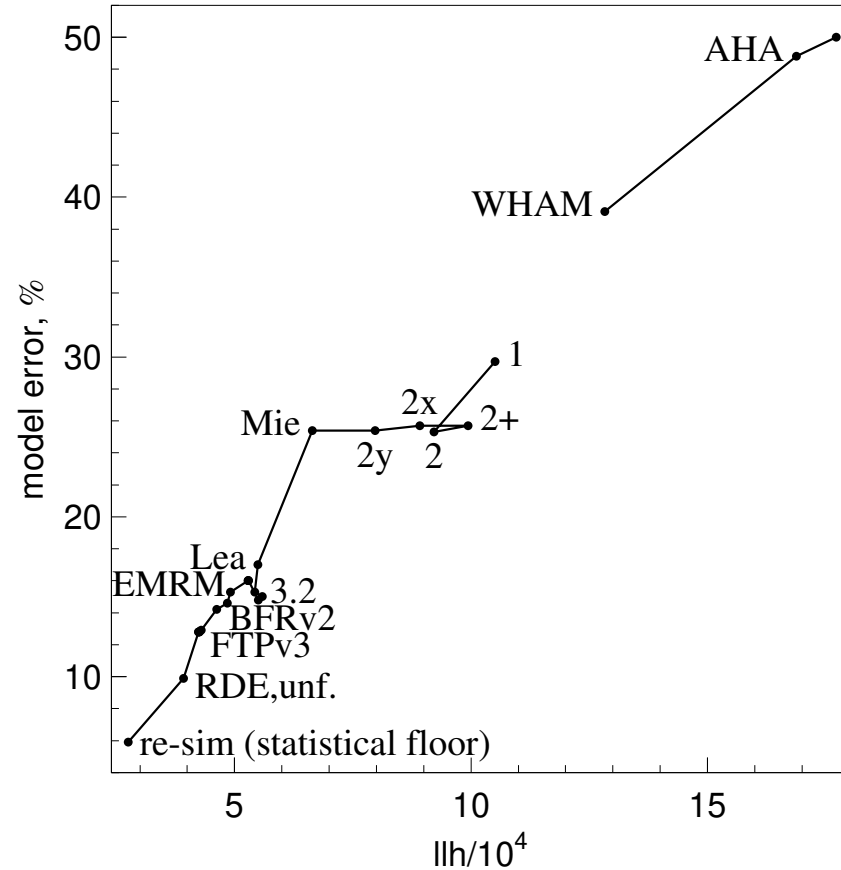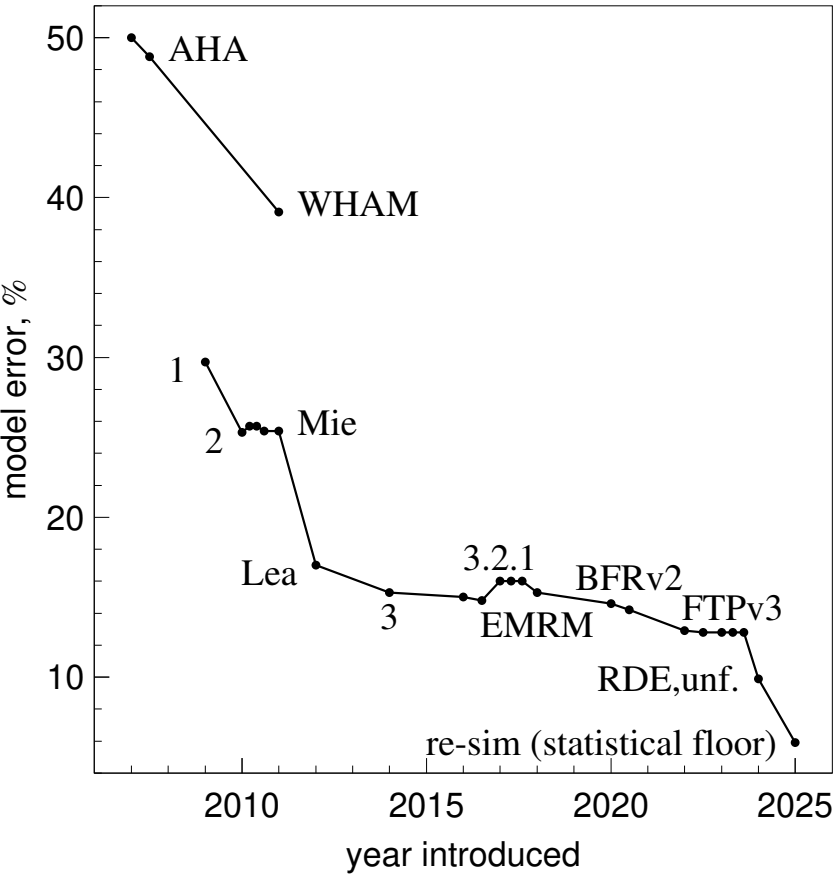Much progress over 30 years

In this presentation I listed 12 AMANDA-era models and 20 SPICE-era models

Improvements can be gauged with llh, model error, and average waveform plot

We have a full description of statistical uncertainties of ice layer properties and tilt corrections
- with a covariance matrix of size 10388 by 10388

However, interpretation of uncertainties is complicated since we have not yet reached the statistical floor

Are we still missing a major piece of the ice model puzzle?

Timeline
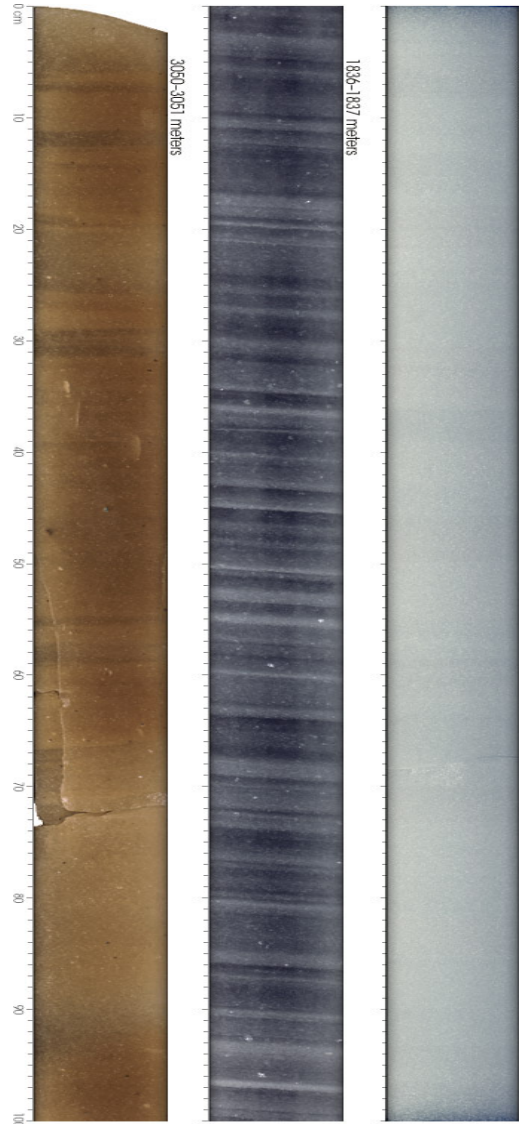
AMANDA ice models:			model error
bulk, f125, mam, mamint, stdkurt, sudkurt, kgm, …			
millennium (published 2006) → AHA (2007)			55%
IceCube ice models:			
WHAM	(2011)		42%
SPICE 1	(2009)		29%
SPICE 2, 2+, 2x, 2y	(2010)	added ice layer tilt	
SPICE Mie	(2011)	fit to scattering function	29%
SPICE Lea	(2012)	fit to scattering anisotropy	20%
SPICE (Munich)	(2013)	7-string, LED unfolding	17%
SPICE^3 (CUBE)	(2014)	llh fixes, DOM sensitivity fits	11%
SPICE 3.0	(2015)	improved RDE, ang. sens. fits	10%
SPICE 3.1, 3.2	(2016)	85-string, correlated model fit	<10%
SPICE HD, 3.2.2	(2017)	direct HI and DOM sens., cable, DOM tilt	
SPICE EMRM	(2018)	absorption-based anisotropy	*single*
SPICE BFR (v1, v2)	(2020)	birefringence-based anisotropy	*LEDs*
SPICE FTP (v0, v1)	(2022)	precise fit to tilt across detector volume	
SPICE FTP (v2, v3)	(2023)	w/precise covariance matrix calculation	

Model error (precision in charge prediction): <10%
Extrapolation uncertainty: 13% (sca) / 15% (abs)
Linearity: < 2% in range 0.1 … 500 p.e.

llh and model error

The quantity that we use during the fit is "llh", which is constructed as a saturated Poisson likelihood for data and simulation with their expectation values compared with the "model error term":
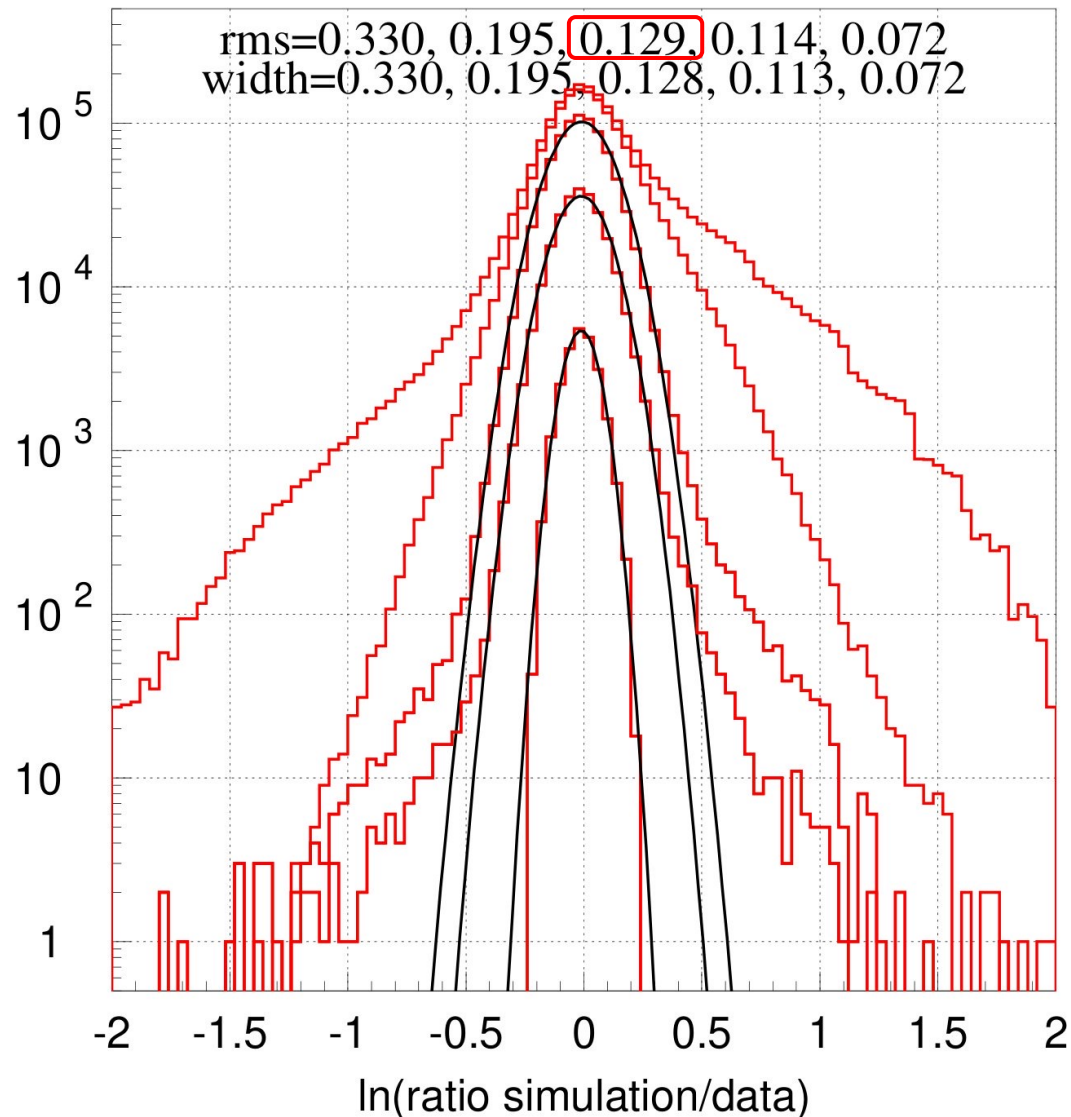
$$\frac{P(\text{same process})}{P(\text{independent processes})} = \left(\frac{\mu_s}{s/n_s}\right)^s \cdot \left(\frac{\mu_d}{d/n_d}\right)^d \cdot \exp\frac{\ln^2(\mu_d/\mu_s)}{-2\sigma^2}$$

For each flasher LED configuration, this quantity is summed over Bayesian-blocked time bins in receiving DOMs and normalized by their number. Then this normalized quantity is summed for all flasher configurations (of which we have 60614 – 12 LEDs times 5160 DOMs minus broken and cDOMs and minus some failed LEDs).

We have made multiple improvements to llh over the years, with each new ice model much better than the previous one. Naturally, a question arises: how far are we from the best possible llh? Say, if the physics of flasher LED events is modeled perfectly, in the absence of any (known or unknown) systematic uncertainties, what is the expected value of the llh? We can refer to such a value as a "statistical floor" of llh.

Model error

rms=0.330, 0.195, 0.129, 0.114, 0.072
width=0.330, 0.195, 0.128, 0.113, 0.072

ln(ratio simulation/data)

The size of σ in the model error term in the llh construction is estimated from plots as shown here. A logarithm of charge ratio in simulation over data is histogrammed for all receiving DOMs for all flasher configurations. The charge we use in this construction is integrated over the time window used by this analysis (i.e., full charge per receiving DOM).

The plot shows 5 histograms (with their rms and width of fitted gaussian listed in the caption) for different threshold value of accepted charge: (1) no cut, (2) 1 p.e., (3) 10 p.e., (4) 100 p.e., and (5) 400 p.e.

The rms/width at each threshold level depends on statistics of data and simulation (i.e., how many events in data and simulation for each configuration). Typically, data has more than 100 events, while simulation (shown here) has only 10. We usually take the middle value (10 p.e. cut – 12.9% here). This number will reduce to 11.8% for 100 simulated events. We had previously estimated (for SPICE 3.2) that after subtracting statistical contribution the model error is 9.8%.
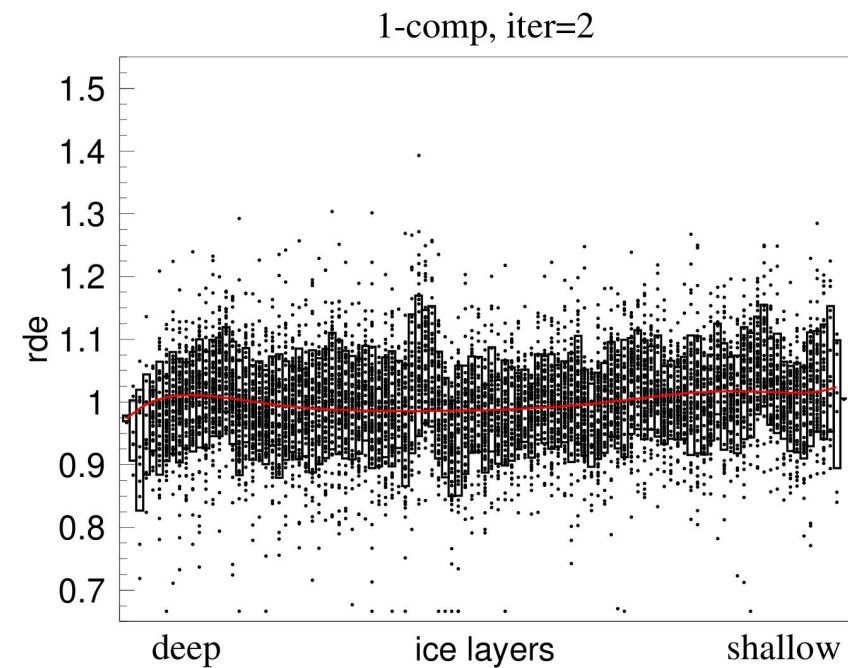
Summary of geometry corrections
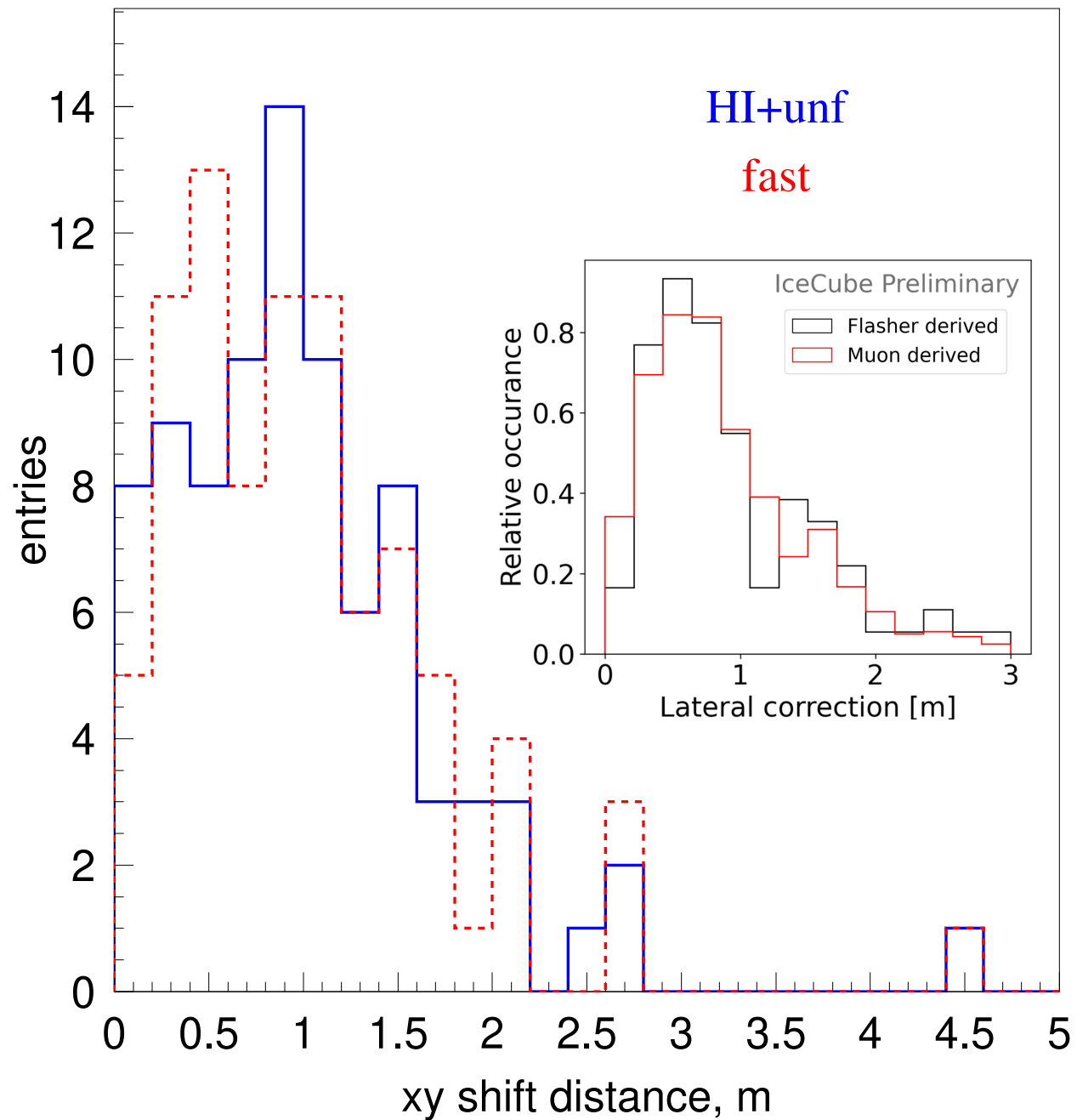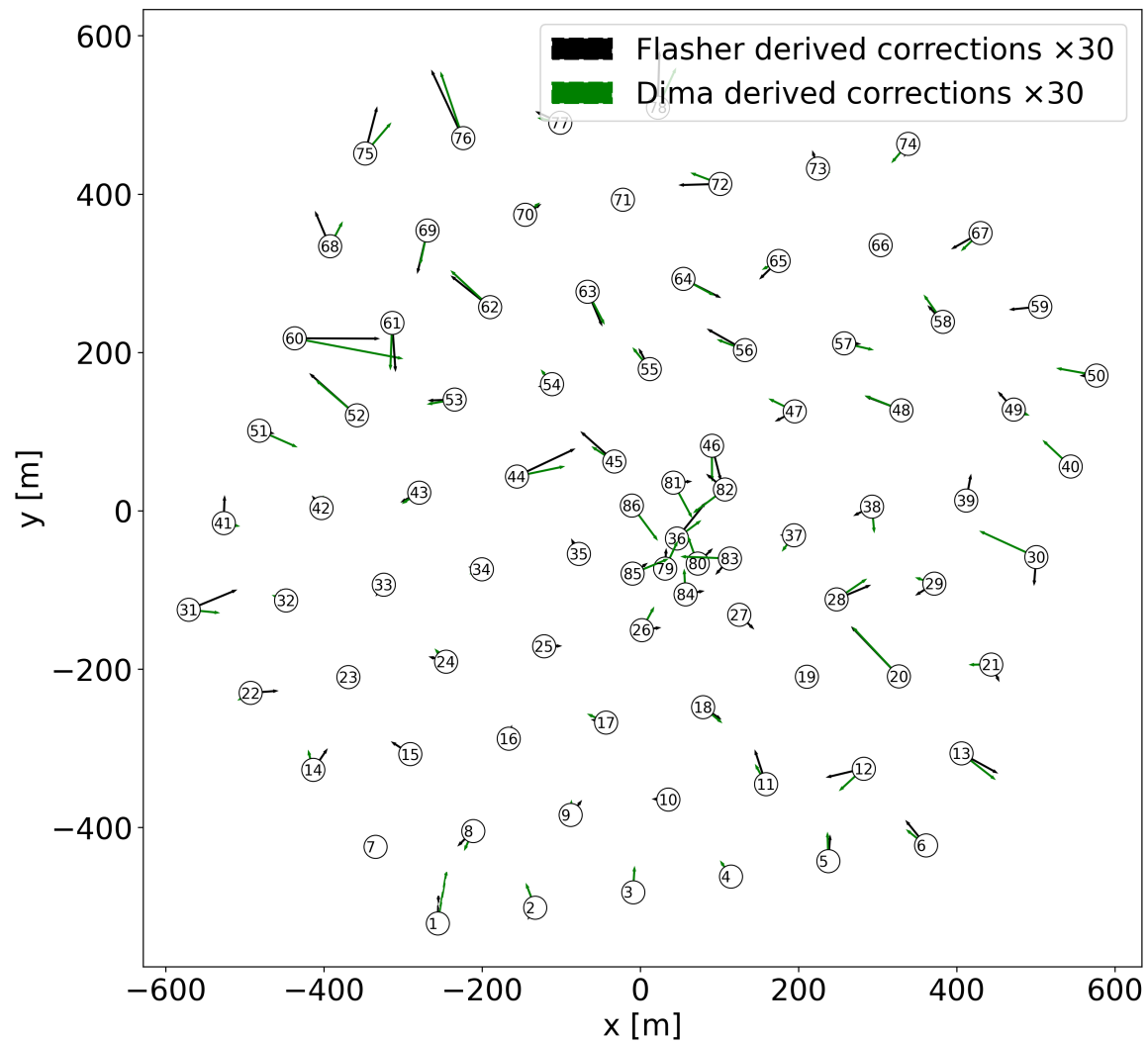
Relative in-ice DOM efficiencies (RDE)
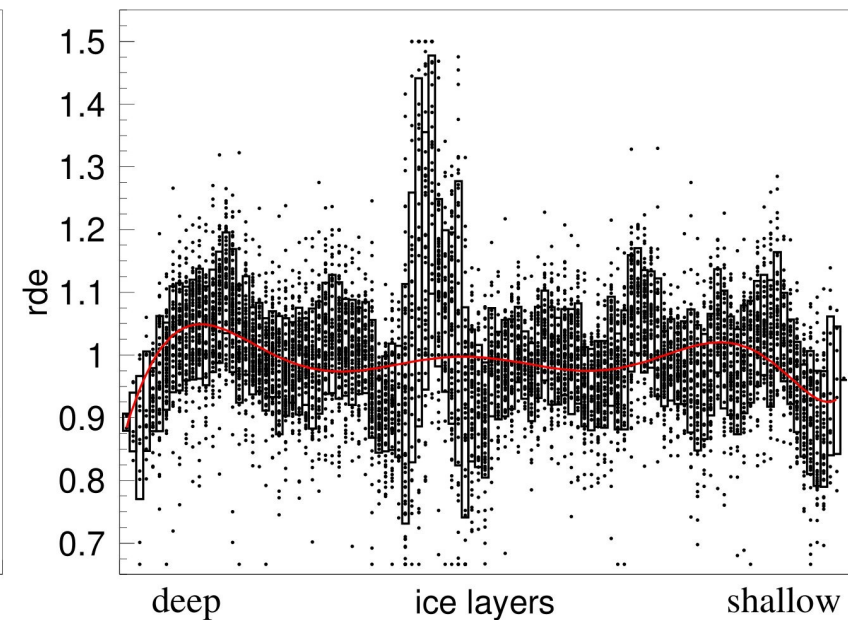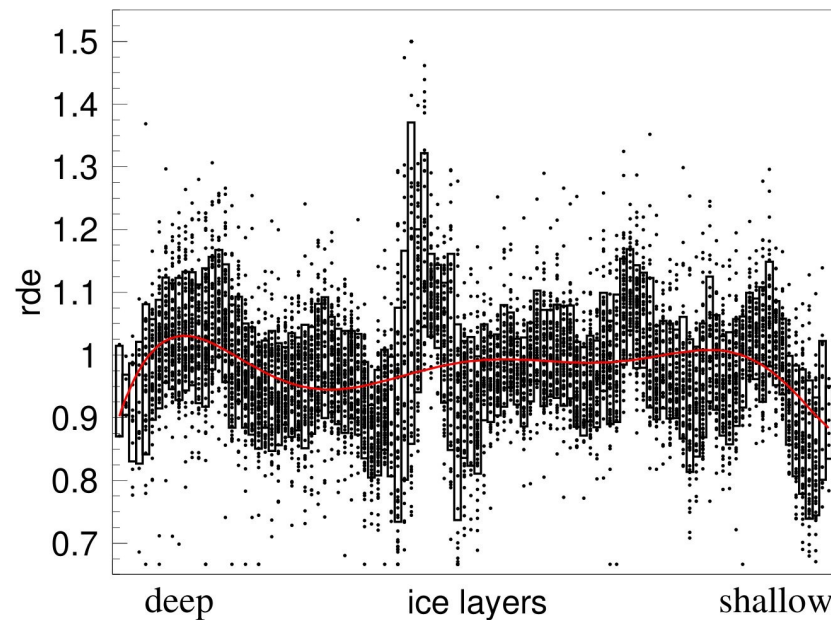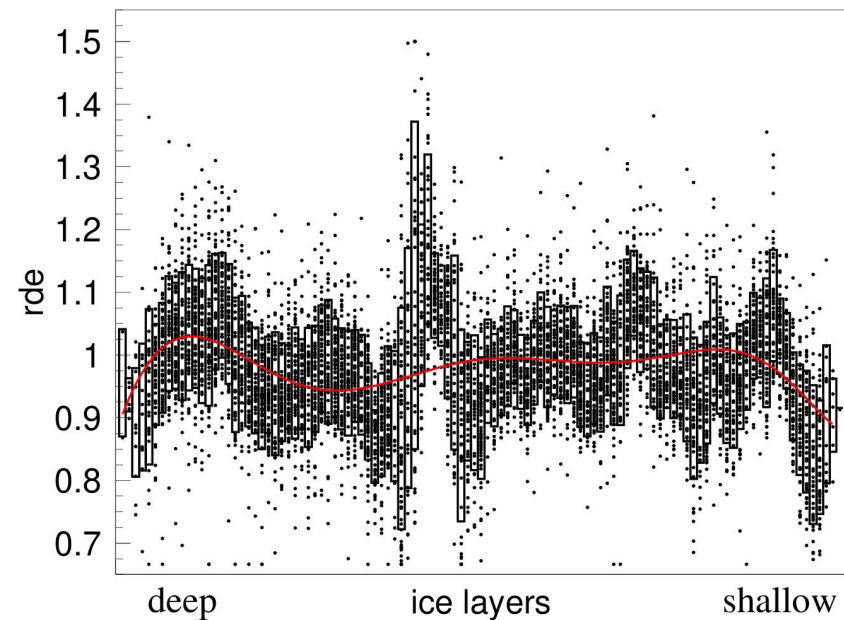
New calculation with SPICE FTPv3

To moderate your expectations:
calculation with former ice models
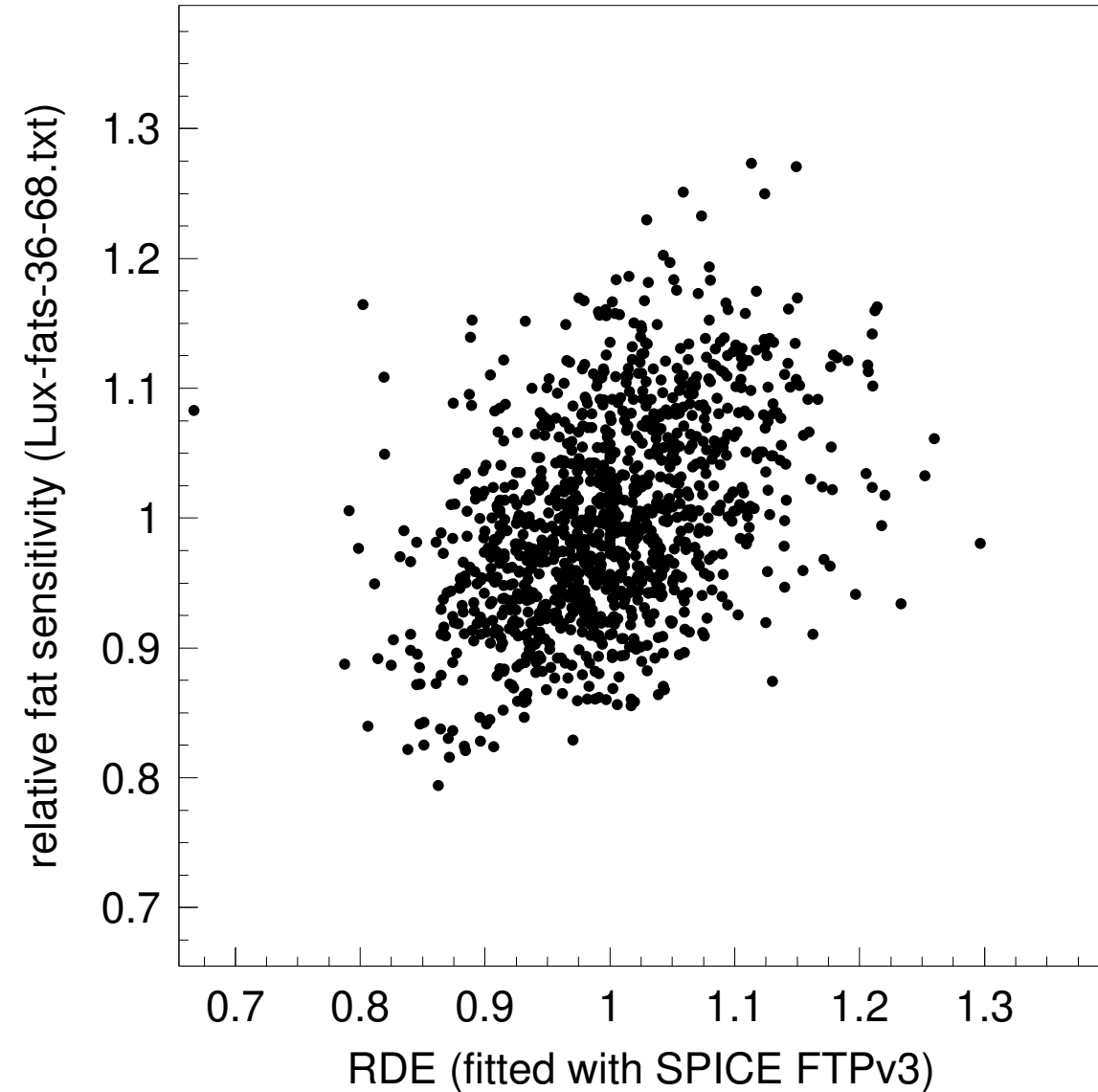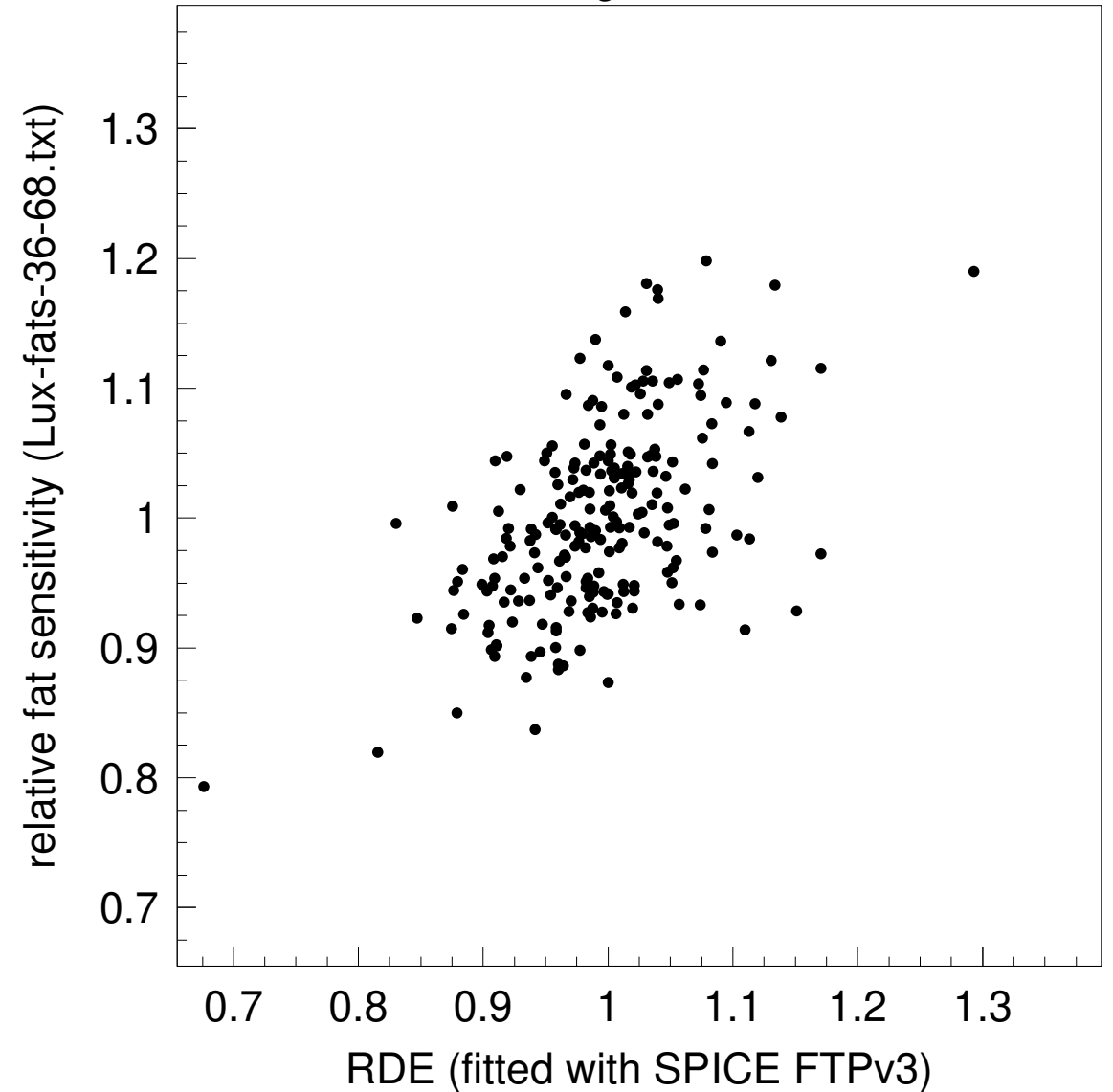strong correlation with the location in ice
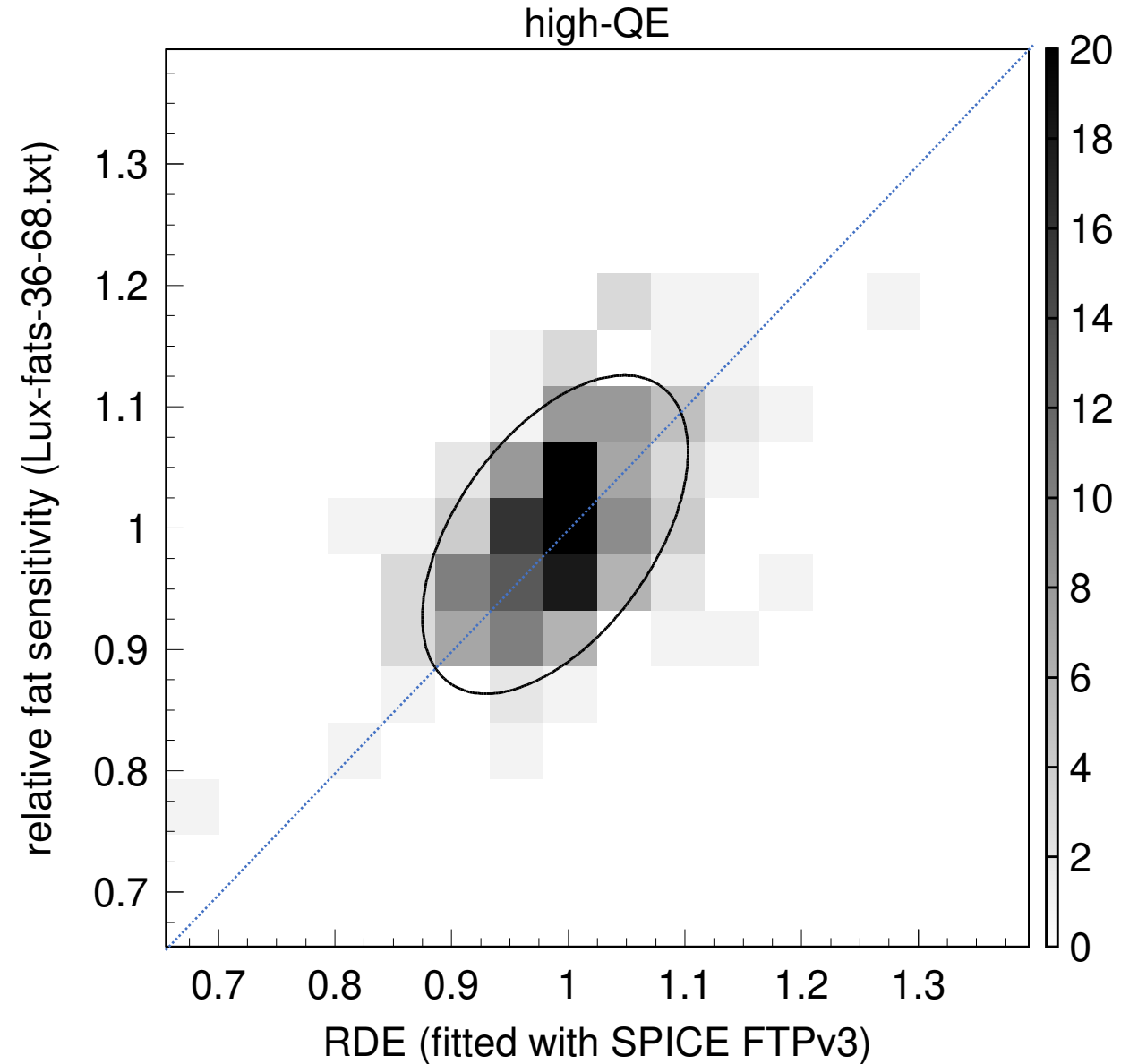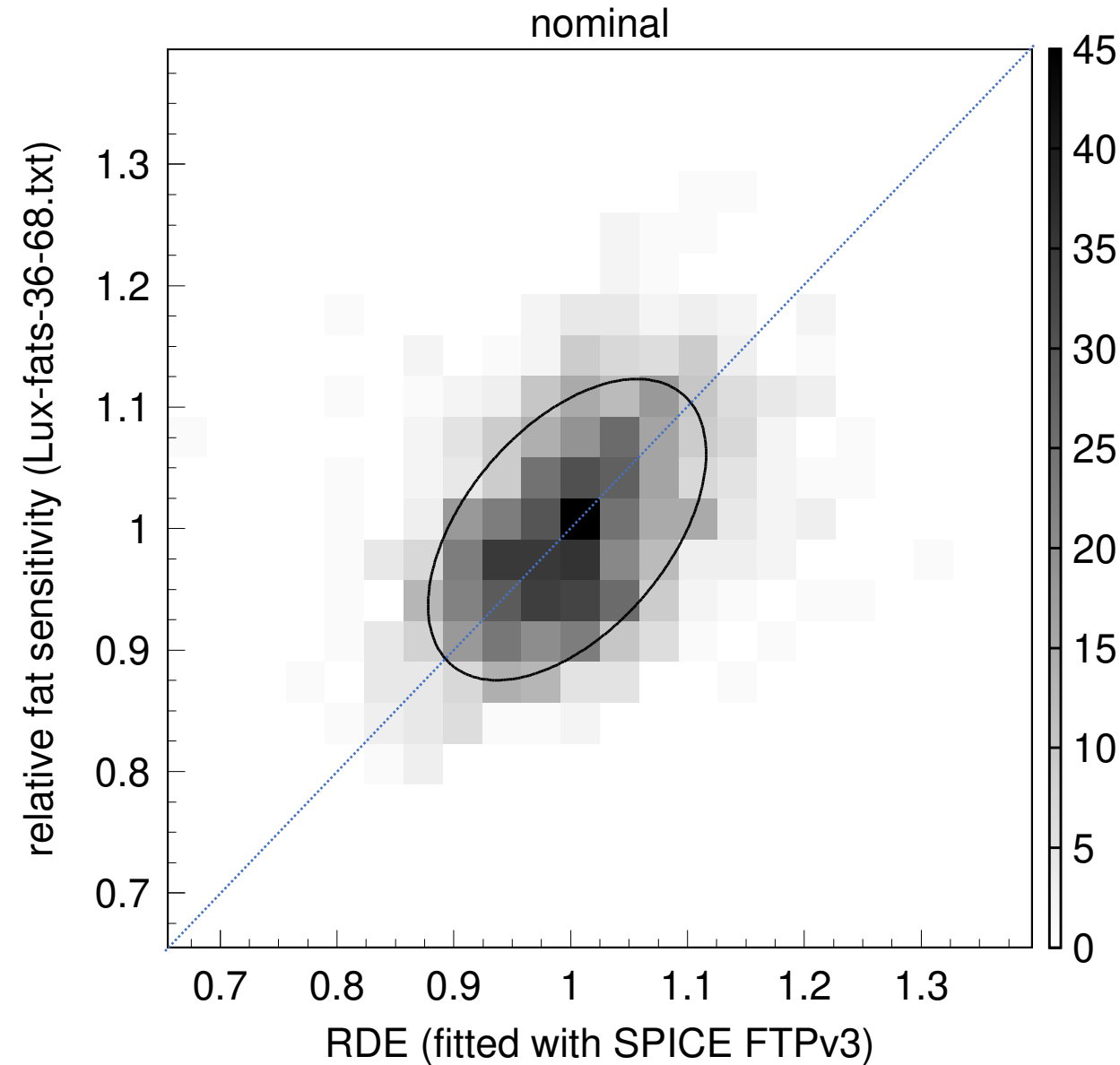
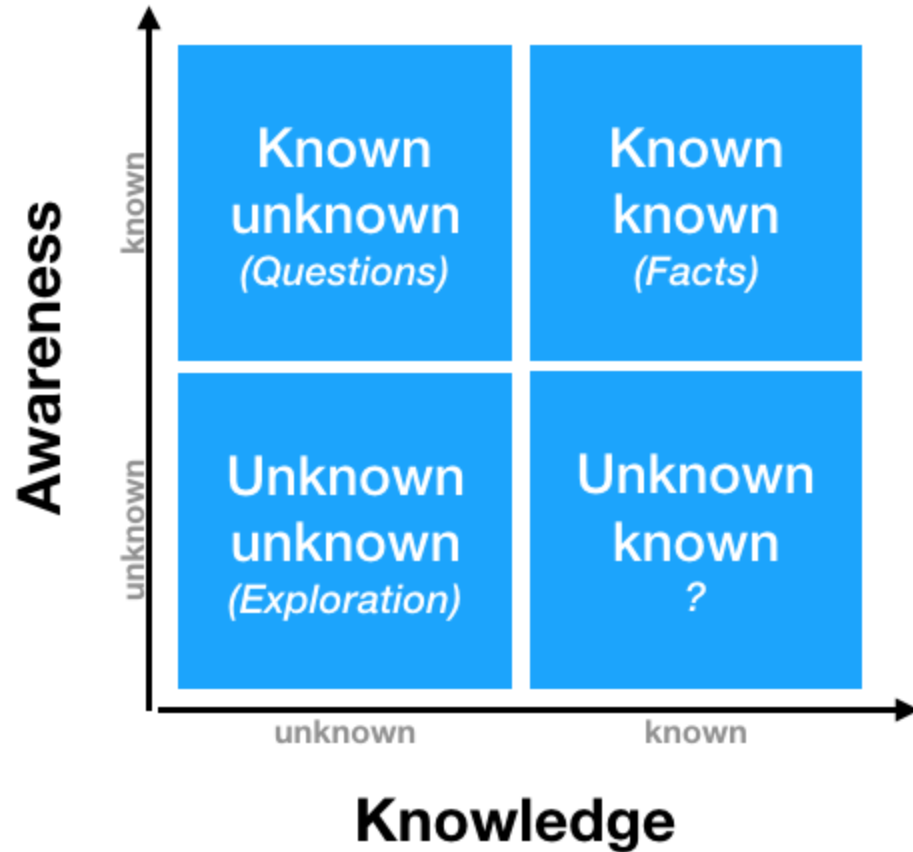# Relative in-ice DOM efficiencies: correlation to FAT

Relative in-ice DOM efficiencies: correlation to FAT

Life after SPICE FTPv3

revisiting the known unknowns

These are known effects; most were previously estimated some with earlier ice models. Here the following is evaluated with the recent SPICE FTPv3 ice model:

- statistical floor
- flasher data issues and cleaning
- LED beam decomposition models
- RDEs (relative in-ice DOM efficiencies)
- hole ice (direct bubble column simulation)
- geometry verification

Ice crystal grain size vs. depth

- Due to the assumptions on unconstrained parameters (elongation, absorption anisotropy…) the size has an overall scaling uncertainty

- The fixed parameters (such as fabric) may also bias the result

- Still we see that grain size increases with depth and in particular below the dust layer

- Grain size seems to be anticorrelated to scattering → crystals are smaller where scattering is stronger, i.e., where there is more dust
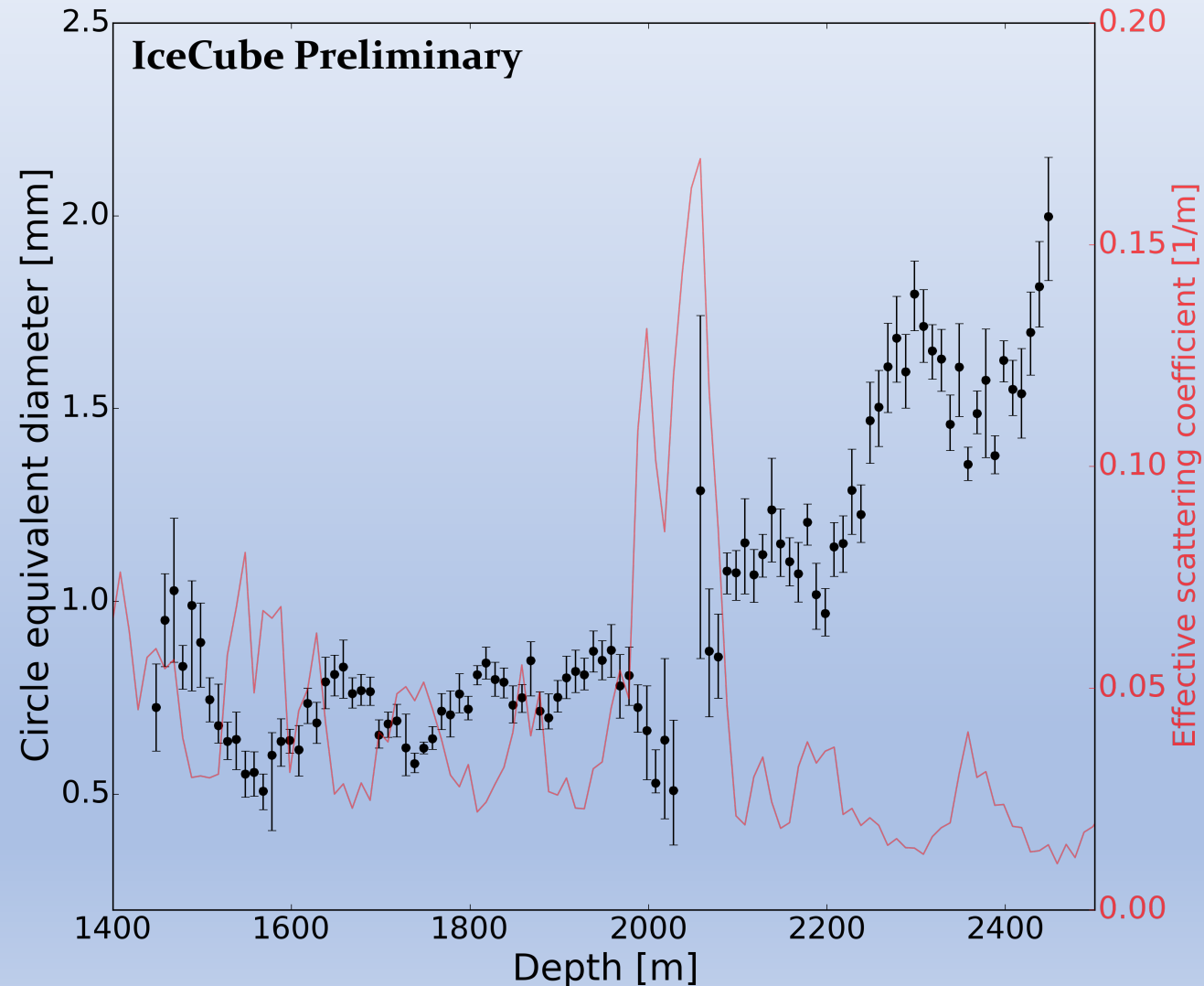
Ice anisotropy with Pencil Beam

- IceCube upgrade to be deployed in 2025/26
- Will contain new calibration devices including several pencil beam devices
- Laser-like beam can sweep over a range of directions, allowing to distinguish models of anisotropy and measure the scattering function directly.